ABSTRACT

Title of dissertation: IMPACTS OF AEROSOL ON CONVECTIVE STORMS AND PRECIPITATION

Yuwei Zhang, Doctor of Philosophy, 2019

Dissertation directed by: Prof. Zhanqing Li
Department of Atmospheric and Oceanic Science/Earth System Science Interdisciplinary Center

Dr. Jiwen Fan
Atmospheric Sciences and Global Change Division
Pacific Northwest National Laboratory

Aerosol-cloud interactions (ACI) remain the largest uncertainty in projections of future changes in climate in response to the buildup of greenhouse gases, even though they have been extensively investigated. Convective clouds have complicated dynamics and microphysics, and aerosol effects on them are the least understood of any cloud type. This study aims to further our understanding of aerosol effects on convective clouds by tackling a few outstanding problems by means of observational data analysis and model simulations under a wide-range of environmental conditions. There are three primary objectives: (1) to investigate the impact of ultra-fine aerosol particles from the Manaus metropolis on convective clouds under the pristine environment of Amazon; (2) to explore and quantify the urbanization effect on convective storms over the Houston area where the anthropogenic effects of both land surface and aerosols are exceptionally strong; (3) to examine and compare the relative significances of fire-induced surface heating and aerosol effects on exceptionally deep convective clouds, or pyroCb.

Ultrafine aerosol particles smaller than 50 nanometers ($UAP_{<50}$) are abundant in the troposphere but have been conventionally considered too small to be activated as cloud condensation nuclei (CCN) to affect cloud formation. Observational evidence and numerical simulations of deep convective clouds (DCCs) over the Amazon show that DCCs forming in a low-aerosol environment can develop very large water vapor supersaturation. This is because fast droplet coalescence reduces integrated droplet surface area and subsequent condensation. $UAP_{<50}$ from pollution plumes that are ingested into such clouds can be activated to form additional cloud droplets on which water condenses and forms additional cloud water and latent heating, thus intensifying convective strength. This "warm-phase invigoration" is demonstrated to have much stronger effects than the "cold-phase invigoration" previously proposed and does not affect the timing of precipitation because warm rain needs to form first to remove droplets and form high in-cloud supersaturation.

Urbanization has local impacts on storms through changing urban land-cover and anthropogenic aerosols. The Chemistry version of Weather Research and Forecast model (WRF-Chem) coupled with spectral-bin microphysics (SBM) are first employed to examine how urban land and anthropogenic aerosols impact DCCs on 19-20 June 2013 over Houston. We find that urbanization in Houston drastically enhances convective intensity and precipitation, primarily due to the urban aerosol effects. Urban land effect does not change precipitation much but initiates mixed-phase clouds 20 min earlier due to urban heating. Urban aerosols accelerate the development of convective cells into ice phase clouds, resulting from larger latent heat release. With the Morrison bulk scheme, the model does not show significant aerosol impacts on convective intensity and precipitation, due to

limitations in representation of aerosol-cloud interaction processes, particularly aerosol drop condensation.

Wildfires can influence severe convective storms through releasing sensible heat and aerosols into the atmosphere. We developed a computationally efficient model capability based on WRF-Chem that can account for the impact of sensible heat fluxes from wildfires on thermodynamics. The model is used to investigate how the Texas Mallard Fire on 11-12 May 2018 led to the development of pyrocumulonimbus (pyroCb) clouds that are well simulated by accounting for both the effects of heat and aerosols emitted from the wildfire. Both heat and aerosol effects increase low-level temperatures and mid-level buoyancy and enhance convective intensity. Intensified convection along with more supercooled liquid condensate at high altitudes due to stronger vertical transport, results in larger hailstones and enhanced lightning. The effects of heat flux on the extreme convection are more significant than those of aerosol emissions. This is on the contrary to the effect of urbanization in Houston for which the effect of land surface change is smaller than that of aerosols, presumably because heat from fire is much more intensive than that from the urban heat island effect.

IMPACTS OF AEROSOL ON CONVECTIVE STORMS AND PRECIPITATION

by

Yuwei Zhang

Dissertation submitted to the Faculty of the Graduate School of the
University of Maryland, College Park in partial fulfillment
of the requirements for the degree of
Doctor of Philosophy
2019

Advisory Committee:

Professor Zhanqing Li, Chair
Doctor Jiwen Fan (PNNL), co-advisor
Professor Kenneth Pickering
Professor Rachel Pinker
Professor Shunlin Liang, Dean's Representative

DEDICATION

To my beloved parents.

STATEMENT OF PUBLICATION AND CONTRIBUTION

Chapter 3 is based on a paper (Fan et al. 2018) in which I am the third author. My contributions are designing numerical experiments with Dr. Fan, conducting all numerical experiments, doing all the analysis of observation data and model simulations, and contributing to the main idea and manuscript.

Fan J., D. Rosenfeld, **Y. Zhang**, S. Giangrande, Z. Li, L. Machado, and S.T. Martin, et al. (2018), Substantial Convection and Precipitation Enhancements by Ultrafine Aerosol Particles. *Science* 359, 6374:411-418. doi:10.1126/science.aan8461.

Chapter 6 is based on a paper (Zhang et al. 2019a).

Zhang Y., J. Fan, T. Logan, Z. Li, and C. Homeyer (2019a), Wildfire impact on environmental thermodynamics and severe convective storm, *Geophysical Research Letters*. doi: 10.1029/2019GL084534.

Chapter 4 is based on a paper (Zhang et al. 2019b).

Zhang Y., J. Fan, and Z. Li (2019b), Impacts of Cloud Microphysics Parameterizations on Simulated Aerosol-Cloud interactions. (In preparation)

Chapter 5 is based on a paper (Zhang et al. 2019c).

Zhang Y., J. Fan, and Z. Li (2019c), Impacts of Land Surface and Aerosol Changes from Houston Urbanization on Convective Storms. (In preparation)

ACKNOWLEDGMENTS

I would first like to thank my advisor, Prof. Zhanqing Li, for all his help, guidance and support of my PhD study and research, for his patience and constructive criticism. Without his guidance and persistent help this dissertation would not have been possible.

I especially express my deep appreciation to Dr. Jiwen Fan. I spent two and half years at Pacific Northwest National Laboratory in visiting and doing PhD intern and I had great pleasure of working with her. She taught me a lot in doing research from the aspect of modeling techniques, analysis methods, organizing stills and scientific thinking. Thanks for her valuable guidance and consistent encouragement.

I would like to extend thanks to Adrian. M. Loftus for all his help, advice and encouragement, and for providing a partial support of my Ph. D study. I also thank Maureen Cribb and other group members at the University of Maryland for their help.

Finally, I would like to express my deepest gratitude to my family and friends for supporting me spiritually throughout my life.

TABLE OF CONTENTS

LIST OF TABLES

LIST OF FIGURES

LIST OF ABBREVIATIONS AND SYMBOLS

ACI	Aerosol-cloud interaction
ACPC	Aerosol-Cloud-Precipitation-Climate
ARI	Aerosol-radiative interaction
ARM	Atmospheric Radiation Measurement (US Department of Energy)
ATTO	Amazonian Tall Tower Observatory
BG	Present-day background
BEP	Building Environment Parameterization
CAPE	Convective available potential energy
CBMZ	Carbon Bond Mechanism Version Z
CCN	Cloud condensation nuclei
$CCN_{>50}$	CCN with a diameter larger than 50 nm
CG	Cloud-to-Ground
CIN	Convective inhibition
CPTEC	Center for Weather Forecasting and Climate Research
DCC	Deep convective cloud
EMC	Environmental Modeling Center
ESRL	Earth System Research Laboratory
FIMS	Fast Integrated Mobility Spectrometer
FINN	Fire INventory from NCAR
GEWEX	Global Energy and Water Cycle Experiment
GLM	Geostationary Lightning Mapper
GOCART	Global Ozone Chemistry Aerosol Radiation and Transport

HAILCAST Hail forecasting model

IC Intra-Cloud

IGAC International Global Atmospheric Chemistry

IGBP International Geosphere–Biosphere Programme

iLEAPS Integrated Land Ecosystem–Atmosphere Processes Study

INPE National Institute of Space Research

IPCC Intergovernmental Panel on Climate Change

LPI Lightning potential index

MEGAN Model of Emissions of Gases and Aerosols from Nature

MERRA-2 Modern-Era Retrospective analysis for Research and Applications, V2

MESH Maximum expected size of hail

MISR Multi-angle Imaging Spectro Radiometer

MINX MISR INteractive eXplorer

MODIS Moderate Resolution Imaging Spectroradiometer

MOSAIC Model for Simulating Aerosol Interactions and Chemistry

N_a Aerosol particle number concentration

NCA National Climate Assessment

NCAR National Center for Atmospheric Research

NCEP National Centers for Environmental Prediction

NCEP/FNL National Center for Environmental Prediction final analysis data

NEXRAD Next-Generation Weather Radar

NLDAS North American Land Data Assimilation System

NLDN National Lightning Detection Network

NOAA	National Oceanic and Atmospheric Administration
NWP	Numerical weather prediction
PBL	Planetary boundary layer
PDF	Probability density function
PI	Pre-industrial
PM	Particulate matter
PyroCb	Pyrocumulonimbus
RAP	Rapid Refresh
RGCM	Regional and global climate model
RRTMG	Rapid radiative transfer model for general circulation model
RH	Relative humidity
RWP	Radar Wind Profiler
S_w	Supersaturation with respect to water
SBCIN	Surface-based convective inhibition
SBM	Spectral-bin microphysics
SD	Size distribution
SMPS	Scanning-Mobility Particle Sizer
SPC	Storm Prediction Center
TCEQ	Texas Commission for Environmental Quality
WRF	Weather Research and Forecasting model
WRF-Chem	Weather Research and Forecasting model coupled with Chemistry
$UAP_{<50}$	Ultrafine aerosol particles with a diameter smaller than 50 nm
UHI	Urban heat island

VD	Vertical distribution
VIIRS	Visible Infrared Imaging Radiometer Suite
WCRP	World Climate Research Programme

Chapter 1. Introduction

1.1 Background

The liquid and solid particles in the atmosphere are classified into aerosol, cloud and precipitating hydrometeors according to their size, chemical composition, water content and fall velocity. Despite their small mass or volume fraction in the atmosphere, through the effects of aerosol-radiative interactions (ARI), aerosol-cloud interactions (ACI) or both, they strongly influence the transfer of radiant energy and the spatial distribution of latent heating through the atmosphere, thereby influencing the weather and climate (e.g., Twomey, 1977; Albrecht, 1989; Rosenfeld, 1998; Anderson et al., 2005; Rosenfeld et al., 2008; Boucher et al., 2013). Feedbacks between aerosols, clouds, precipitation, and the climate system are recognized by the Intergovernmental Panel on Climate Change (IPCC) as one of the key sources of uncertainty in our knowledge of Earth's energy budget and anthropogenic climate forcing (e.g., Arakawa, 1975, 2004; Haywood and Boucher, 2000; Lohmann and Feichter, 2005; Andreae et al., 2005).

Cumulus clouds are pervasive on earth and play important roles in the transfer of energy through the atmosphere. Under certain conditions, shallow cumuli may grow to deep convective clouds (DCCs), which are significant sources of precipitation and play a key role in the hydrological and energy cycle as well as regional and global circulation (Arakawa, 2004). DCCs and precipitation are determined by water vapor, vertical motion of air and cloud microphysics. Aerosols affect these three factors through ARI and ACI.

Aerosols can substantially reduce the amount of solar radiation reaching the ground (Ramanathan et al., 2002; Li et al., 2007), and thus reduce sensible and latent heat fluxes

that drive the diurnal evolutions of temperature (Ding et al. 2013), and the development of the boundary layer (Li et al., 2017a). This in turn causes an enhancement of relative humidity (RH), which favors the hygroscopic growth of aerosols and enhances the scattering of solar radiation. Besides cooling the surface, for strongly absorbing aerosol particles like black carbon (Peng et al., 2016), they also heat some part of atmosphere depending on the locations (horizontally and vertically), which changes atmospheric stability and even circulation (Wang et al., 2013), leading to complicated responses of clouds, radiation, and precipitation to aerosol loading (Yang et al., 2013a, b; Fan et al., 2015, 2016; Yang et al., 2016, Li et al., 2017b).

Aerosols can also serve as cloud condensation nuclei (CCN) and ice nuclei (IN) upon which cloud droplets and ice crystals form. How aerosols affect cloud properties and precipitation through ACI strongly varies among cloud types that are mainly controlled by atmospheric dynamics and thermodynamics. For warm clouds, the ‘‘Twomey’’ effect (i.e., reducing droplet size and increasing reflectance of clouds due to increased droplet number for a constant liquid water path) proposed about four decades ago (Twomey, 1977) is relatively well understood. Aerosols can also indirectly impact cloud lifetimes, coverage, and cloud albedo thereby altering the Earth's radiation balance (Albrecht, 1989; Wood, 2012) and water cycle. For non-precipitating clouds with cloud droplet effective radius smaller than ~14μm, cloud droplets are usually small and increasing aerosols makes even smaller cloud droplets, which evaporate much faster when mixing with the ambient dry air, leading to stronger evaporative cooling and mixing at the cloud boundaries (Randall, 1980 a,b), smaller cloud water content and lower cloud albedo in polluted conditions (Chen et al. 2012).

For DCCs with more complicated dynamics, thermodynamics, and microphysics, aerosol impacts are extremely complex and not as understood as those for shallow clouds. DCCs produce copious precipitation and drive the global-scale circulation (Houze, 2014). Precipitation, latent heat, and cloud radiative forcing associated with DCCs are strongly modulated by cloud microphysical processes (Barnes et al., 2016). The basic theory proposed for aerosol-DCC interactions is that increasing aerosol concentrations can suppress warm rain due to a reduction in droplet size, which allows more cloud water to be lifted to a higher altitude wherein the freezing of this larger amount of cloud water releases additional latent heat, thereby invigorating convective updrafts (referred to as "cold-phase invigoration," Rosenfeld et al. 2008). This can be very significant under the conditions of warm-cloud bases (>15 °C) and weak wind shear. Where the warm-cloud zone is deeper, the suppression of warm rain by aerosols can be more significant (Li et al., 2011; Rosenfeld et al., 2014; Fan et al., 2012). Where convection is nearly vertical due to weak wind shear, the increase of latent heating can dominate over the increase of evaporative cooling (Fan et al., 2012, 2013; Khain et al., 2008; Tao et al., 2007; Lebo et al., 2012). Enhancement in DCC intensity favors enhanced storm electrification, larger precipitation rates, as well as taller clouds and larger anvils.

Many factors can affect whether aerosols invigorate or suppress convective intensity through aerosol indirect effects, such as environmental wind shear (Fan et al., 2009; Lebo et al., 2012), relative humidity (Fan et al., 2007; Khain et al., 2008), and Convective Available Potential Energy (Storer et al., 2010; Lebo et al., 2012; Morrison, 2012). In the cases where strong wind shear exists and/or cloud bases are cold, aerosols could strongly suppress convection and precipitation due to strong evaporative cooling of

the small cloud droplets and/or less efficient ice growing processes (Khain et al., 2008; Morrison, 2012; Fan et al., 2012). Aerosol effects on DCCs are also strongly dependent on the regimes of convective systems. For the systems that are mainly triggered by gust fronts, aerosols may change the intensity and size of gust fronts, which then change the cloud-system organization and impact precipitation and cloud macrophysical properties (Lee, 2012; Lee et al., 2014; Morrison, 2012). Supercell systems that are strongly driven by dynamic pressure perturbations are less sensitive to aerosols (Storer et al., 2010; Morrison, 2012). However, in some situations, adding aerosols leads to larger hydrometeors, less evaporative cooling, and weaker gust fronts, which do not undercut the updrafts and allows for the maintenance of super cells and severe convective storms (Rosenfeld and Bell 2011).

1.2 Objectives

ACI remains the largest uncertainty in projections of future changes in climate in response to the buildup of greenhouse gases, even though it has been extensively investigated. Convective clouds have complicated dynamics and microphysics, and aerosol effects on them are the least understood of any cloud type. The overall goal of my dissertation work is to gain a better understanding of how aerosol affects convective clouds under the context of urbanization and wildfires, both of which have been increasing and changed land, sensible heat and aerosols. Specific science questions that we are trying to answer are: (1) how do aerosols particularly the numerous ultrafine aerosol particles from mega-cities in the warm and humid regions such as Amazon and Houston affect convective intensity and precipitation? (2) how do aerosols and land surface change as a result of urbanization jointly and separately affect convective development and precipitation in

Houston region? (3) What are the influences of wildfires on environmental thermodynamics and the subsequent severe storm properties and how can one computationally parameterize the effect in model?

1.3 Outline

Chapter 1 provides an overview of previous studies on aerosol's impact on convective clouds and precipitation and presents the scientific questions. Chapter 2 lists the sources of datasets used and basic description of the model utilized in this dissertation work. Chapter 3 explores the effect of aerosol properties (e.g., concentration, size, size and vertical distribution) on DCCs and precipitation and raises a new invigoration mechanism contributed by UAP. Chapter 4 investigates the impacts of cloud microphysics parameterizations on simulated aerosol-DCC interactions and examines the potential problems with Morrison two-moment bulk scheme in representing aerosol impacts on DCCs. Chapter 5 examines how urban land and anthropogenic aerosols over Houston impact the evolution of DCCs, convective intensity and precipitation. Chapter 6 describes how wildfires impact environmental thermodynamics and severe convective storms by utilizing a new model that can computational efficiently account for the impact of sensible heat fluxes from wildfires on thermodynamics. Chapter 7 presents a summary of Chapter 3-6 and suggestions for future studies.

Chapter 2. Data and Models

2.1 Observation Data

In Chapter 3, we utilize the dataset from the GoAmazon 2014/2015 field campaign to do the observational analysis and model evaluation. The GoAmazon experiment was carried out near the Manaus metropolis aiming to gain a better understanding of the impacts of pollution emissions from Manaus on the hydrological cycle and climate in the tropical rainforest through the wet and dry seasons from January 2014 through December 2015 (Martin et al., 2017). All ground-based and airborne observational datasets covering aerosol, cloud and meteorological properties can be obtained from the U.S. Department of Energy's Atmospheric Radiation Measurement (ARM) program data archive at http://www.archive.arm.gov/discovery/#v/results/s/fiop::amf2014goamazon. Specifically, the measurements from the Atmospheric Radiation Measurement 1290-MHz Ultra High Frequency Radar Wind Profilers (RWP), having a vertical resolution of 120 m and temporal resolution ~6 s, are used for providing the most accurate datasets on vertical air motions, reflectivity and precipitation rates for Amazon DCCs. The accuracy of the RWP retrievals is expected to be within 1 to 2 m s^{-1} within convective updrafts that do not indicate large hail. There was no retrieval from the RWP between 3.5- and 5.5-km altitudes due to retrieval contamination from melting particles. Aerosol measurements are from the Scanning-Mobility Particle Sizer (SMPS) with 5-min intervals. The standard SMPS instrument measures the aerosol number size distribution in the particle diameter range from 10 to 500 nm. The uncertainty for the data at T3, which is 70 km downstream of Manaus, is largely dominated by the variability in the sampling flow rate, which is around

+/-10%. Radiosonde sounding data is applied for calculation of the environmental convective available potential energy (CAPE) and convective inhibition (CIN).

In Chapter 4 and 5, we use the following observation data over Houston area for model evaluation. Particulate matter (PM) 2.5 data are provided by Texas Commission for Environmental Quality (TCEQ) at https://www.tceq.texas.gov/agency/data/pm25.html. The Visible Infrared Imaging Radiometer Suite (VIIRS) retrieved cloud base height and CCN at cloud base are estimated based on the method of Rosenfeld et al., (2016). The surface pressure and 10-m winds are from the North American Land Data Assimilation System (NLDAS) with 0.125-deg resolution at https://climatedataguide.ucar.edu/climate-data/nldas-north-american-land-data-assimilation-system. The radar reflectivity is obtained from Next-Generation Weather Radar (NEXRAD) network at https://www.ncdc.noaa.gov/data-access/radar-data/nexrad-products. The National Centers for Environmental Prediction /Environmental Modeling Center (NCEP/EMC) Stage IV Data is used as the observation of precipitation with hourly output at 4-km resolution (Lin and Mitchell, 2005). The NCEP Stage IV precipitation data are from https://www.emc.ncep.noaa.gov/mmb/ylin/pcpanl/stage4/. The meteorological and chemical lateral boundary and initial conditions were created from the Modern-Era Retrospective analysis for Research and Applications, Version 2 (MERRA-2, Gelaro et al., 2017).

In Chapter 6, we employ the observation data discussed below to do model simulation and evaluation. The Anderson 13 fuel category data and high-resolution topography data available at http://www.landfire.gov are used in the fire-spread model (SFIRE) that was coupled with WRF (Mandel et al., 2011 and Mandel et al., 2014) for

estimating fire behavior and spread. The smoke plume height data digitized from the Multi-angle Imaging Spectro Radiometer (MISR) based on the MISR INteractive eXplorer (MINX) software are utilized to evaluate the predicted plume height (Nelson et al., 2014). The MISR data are obtained from https://misr.jpl.nasa.gov/getData/accessData/. To analyze and evaluate the thermodynamics before the convection, sounding data from National Weather Service forecast office at Amarillo, TX (KAMA) are used. The observed radar reflectivity and the radar-retrieved maximum expected size of hail (MESH) data are from Gridded NEXRAD WSR-88D Radar data (GridRad; Homeyer and Bowman, 2017) created at 5-min temporal intervals for this study. The MESH data used in this study are developed from a newly-improved algorithm (Murillo and Homeyer, 2019). The NEXRAD and MESH data were produced by co-author Dr. Cameron Homeyer and available at http://gridrad.org/. The NCEP Stage IV precipitation data are used as the observation of precipitation with hourly output at 4-km resolution. The lightning observation data are from National Lightning Detection Network (NLDN; Cummins and Murphy, 2009). The NLDN lightning data were obtained through Dr. Ronald Holle at Vaisala, Inc (https://my.vaisala.net/en/services/dataservicesandsolutions/lightningdata/Pages/NLDN.aspx). The Storm Prediction Center (SPC) report data are available from https://www.spc.noaa.gov/climo/online/.

All the data and sources are summarized in Table 2.1.

Table 2.1 Observation data and source

Data	Source
GoAmazon field campaign data	http://www.archive.arm.gov/discovery/#v/results/s/fiop::amf2014goamazon
PM 2.5 at TCEQ	https://www.tceq.texas.gov/agency/data/pm25.html
NLDAS	https://climatedataguide.ucar.edu/climate-data/nldas-north-american-land-data-assimilation-system
NEXRAD	https://www.ncdc.noaa.gov/data-access/radar-data/nexrad-products; http://gridrad.org/
Stage IV precipitation	https://www.emc.ncep.noaa.gov/mmb/ylin/pcpanl/stage4/
MISR	https://misr.jpl.nasa.gov/getData/accessData/
Anderson 13 fuel category data	http://www.landfire.gov
NLDN	https://my.vaisala.net/en/services/dataservicesandsolutions/lightningdata/Pages/NLDN.aspx
SPC	https://www.spc.noaa.gov/climo/online/

2.2 Model Description

The WRF model is a numerical weather prediction (NWP) system designed to serve both atmospheric research and operational forecasting needs. The Advanced Research WRF (ARW; Skamarock et al., 2008) is used that was developed by the National Center for Atmospheric Research (NCAR) Mesoscale and Microscale Meteorology Division in support of atmospheric research community.

WRF-Chem (Grell et al., 2005) can account for the effects of different types of aerosols (e.g., sulfate, nitrate, chloride, carbonate, ammonium, sodium, calcium, black carbon, primary organic mass, and other inorganic mass). The transport of meteorological and chemical variables is treated using the same vertical and horizontal coordinates with no interpolation in space and time (Zhang, 2008). The direct effect of aerosol on shortwave radiation is simulated based on the Mie theory following the approach of Fast et al., (2006). The indirect effect of aerosols on cloud formation is also accounted for through the effects

of clouds on shortwave radiation, treatments of aerosol activation/re-suspension, and prognostic cloud droplet number concentrations based on activated aerosols, as described by Chapman et al., (2009). Carbon Bond Mechanism Version Z (CBMZ; Zaveri and Peters, 1999) gas-phase chemistry and the Model for Simulating Aerosol Interactions and Chemistry (MOSAIC; Zaveri et al., 2008) aerosol reaction scheme are included. Global Ozone Chemistry Aerosol Radiation and Transport (GOCART) dust and sea salt emission schemes are used.

The coupling of spectral-bin microphysics (SBM) with MOSAIC in WRF-Chem v3.6.1(Gao et al., 2016) is applied in Chapter 4 and 5. The aerosol activation calculation uses the water vapor supersaturation calculated in the SBM along with the MOSAIC aerosol chemical composition and size. The cloud-borne aerosol resuspension calculation uses a droplet loss rate due to evaporation that is now calculated in the SBM for the coupling. In a similar way, the cloud-borne aerosol wet-removal calculation uses a droplet loss rate due to conversion of cloud drop to rain and ice particles that are also now calculated in the SBM for the coupling (Gao et al., 2016).

Chapter 3. Ultrafine Aerosol's Impacts on Deep Convective Clouds and Precipitation

3.1 Introduction

Over the unperturbed Amazon rainforest region, the pristine background is very clean with very low concentrations of aerosols on the order of hundreds per cubic centimeter (Pöschl et al., 2010; Andreae, 2007). Responses of cloud properties to aerosols are non-linear and most sensitive to the addition of particles when the background is very clean (i.e., the "aerosol-limited regime;" Pöschl et al., 2010; Lohmann and Feichter, 2005; Koren et al., 2014). Therefore, the aerosol effect on convective clouds over the Amazon region is expected to be large, and previous studies have demonstrated evident smoke aerosol influence on convective clouds during dry seasons in the Amazon (June-September) (Andreae et al., 2004; Koren et al., 2008; Lin et al., 2006). In addition to the low total aerosol concentration, the ultrafine aerosol particles with a diameter smaller than 50 nm ($UAP_{<50}$) are typically nearly absent over the Amazon rainforest, as new particle formation has rarely been observed in the boundary layer (Zhou et al., 2002; Kulmala et al., 2011). $UAP_{<50}$ are often transported downward from the free troposphere into the boundary layer and subsequently grow to particles that are traditionally considered as $CCN_{>50}$ (Wang et al., 2016). However, the Manaus metropolis, a city of about two million people, produces a pollution plume that generally follows the north-easterly trade winds and is an important source of elevated $UAP_{<50}$ concentrations (Pikridas et al., 2015).

In this Chapter, we take advantage of the unique observational data from GoAmazon 2014/5 (e.g., the direct cloud updraft velocity measurements for DCCs occurring in a

similar convective environment but different aerosol environment) to investigate the observed aerosol effects, as well as to perform and analyze high-resolution simulations of a sample case, using the detailed spectral-bin microphysics scheme to scrutinize the mechanism. We aim to examine how do aerosols particularly the numerous ultrafine aerosol particles from mega-cities in the Amazon warm and humid regions affect convective intensity and precipitation.

3.2 Observed relationships of convection and precipitation with aerosols

To analyze the relationship between updraft velocity, radar reflectivity, and surface precipitation with aerosol particle number concentration (N_a), only the locally occurring systems for the wet season of 2014 from 01 March to 31 May based on criteria in Tang et al., (2016) are selected to constrain the selected convective cases occurring within similar dynamics and thermodynamics environments. The selection criteria are (1) convection occurred between 1100-1900 local time and (2) no convection occurred during the 3 hours preceding the locally occurring systems. The second criterion excludes cases with previous convective clouds, which are likely from the propagating systems. Another criterion to ensure deep convective clouds: the maximum echo height determined by reflectivity greater than 0 dBZ measured by RWP for each event is higher than 10 km. There are 20 cases meeting the above criteria during the analysis period. However, aerosol measurements from SMPS for three of the events are reported as having bad data, which left 17 qualifying locally occurring cases: the 11, 17, 22, 23 and 26 events in March; the 1, 12, 18, 20, 21, 23 and 25 events in April; and the 16, 19, 20, 30, and 31 events in May (Table 3.1). The low-level air for these cases is generally northeasterly, favoring the

transport of the Manaus pollution plume to the T3 site (Figure 3.9). The N_a at the T3 site varies substantially from case to case (Table 3.1).

Table 3.1 Aerosol number concentrations for all 17 selected local occurring systems from 2014 wet season with D>15 nm and D>50 nm in the order of low to high concentrations as plotted in Figure 3.1

Date (MM/DD)	$D > 15$ nm (cm^{-3})	Date (MM/DD)	$D > 50$ nm (cm^{-3})
03/23	495	03/22	287
03/22	553	03/23	302
04/21	609	04/21	353
05/31	711	05/16	383
05/30	853	05/30	449
04/12	1455	04/01	537
05/16	1525	05/31	649
05/19	1662	05/20	716
04/23	1721	04/23	793
04/18	1930	04/12	877
04/01	1998	04/18	952
03/11	2346	03/11	1079
05/20	2679	05/19	1214
03/26	3162	03/26	1348
04/20	3462	03/17	1664
03/17	3619	03/21	1872
03/21	3848	04/20	1927

Figure 3.1 shows the correlation of mean vertical velocity estimated for the top 10 percentile of updrafts in each convective event with the respective aerosol particle number concentration averaged over a 30-min period before the start of convection at the T3 site (~70 km southwest of Manaus, downwind). The convective updraft velocity (w) is found to increase with an increase of N_a for aerosols with a diameter (D) larger than 15 nm, however, the increasing trend in updraft intensity as N_a increases does not hold well when considering only those aerosols having D>50 nm. The result suggests that $UAP_{<50}$ are the primary drivers for intensified convection, not the $CCN_{>50}$.

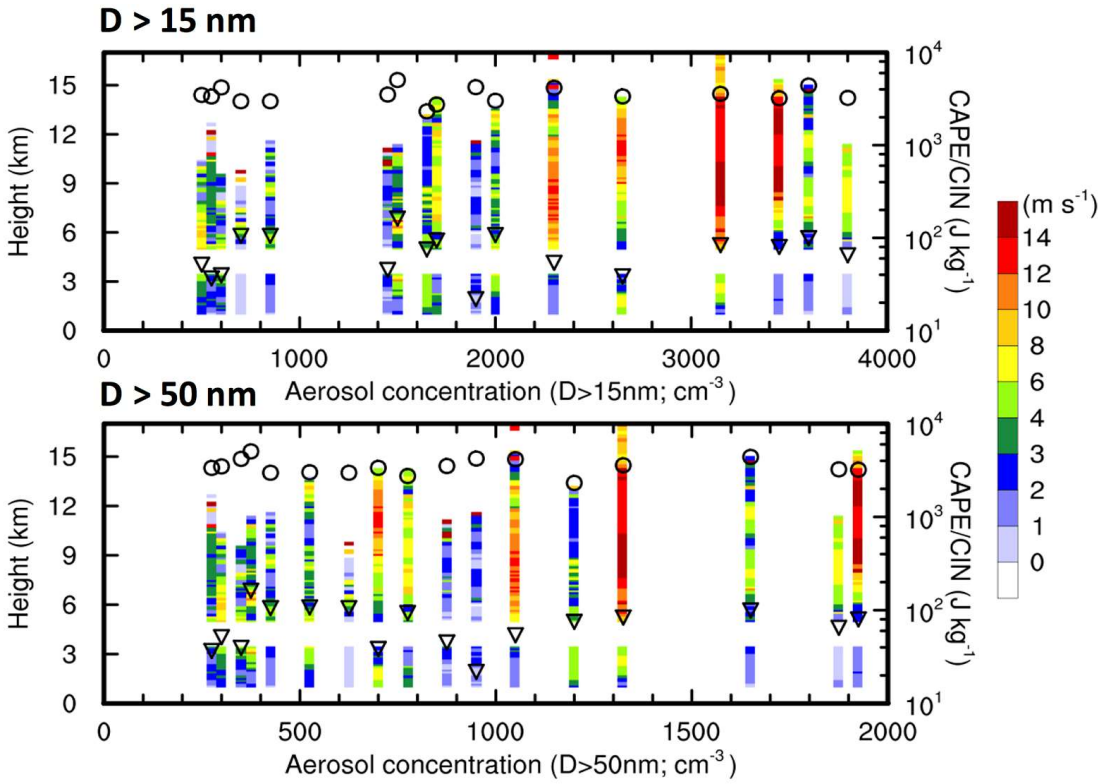

Figure 3.1 Vertical profiles of updraft velocity averaged over the 90th-100th percentile of updrafts and CAPE/CIN in each selected local convective case as a function of N_a with D>15 nm and D>50 nm. The circles and triangles denote the CAPE and CIN values of each case, respectively.

To further clearly show the increasing trend of convection with N_a, the updraft velocity was segregated according to four aerosol groups (ranging from lower to higher N_a). A monotonic and dramatic increase of w for D>15 nm is displayed in Figure 3.2. The number of cases for each group is marked on Figure3.2. The value of w increases from 4 m s^{-1} for the lowest N_a group to 10 m s^{-1} for the highest N_a group. The probability density function (PDF) of w and rain rate from the four aerosol groups indicate that occurrences of stronger updraft velocities are more frequent with the increase of $UAP_{<50}$ (Figure 3.3). For each aerosol group, the frequency for w in each bin is calculated using an interval of 1 m s^{-1} with

the number of points divided by the total convective points of the group (i.e., sum of the convective points from the cases of the group).

The correlation of the maximum velocity averaged over the top 10 percentile of updrafts in each case with aerosol concentrations for D>15 nm and D>50 nm also shown in Figure 3.4. R^2 is doubled for aerosols with D>15 nm compared with those with D>50 nm, indicating that the correlation is higher for D>15 nm. However, the correlation for both D>15 nm and D>50 nm is not good because the data are too scattered, and the single value of vertical velocity is not a good way to present convective intensity.

Besides the convection intensity represented from updraft speed, the radar reflectivity measurements provide an estimate of the microphysical properties related to storm precipitation properties available from the RWP. The corresponding radar reflectivity (Figure 3.5) also increased evidently with the increase of N_a counting $UAP_{<50}$ throughout the vertical profile, associated with hydrometeor size and precipitation rate increases. This is also demonstrated in maximum surface rain rate (Figure 3.6).

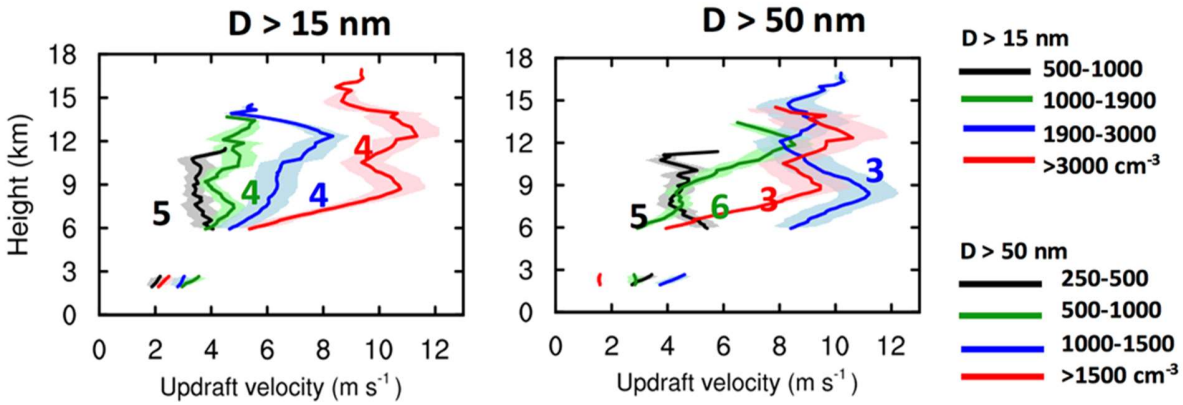

Figure 3.2 Vertical profiles of the updraft velocity averaged over the top 10 percentile of updrafts for each case for the four aerosol groups and standard error (shaded) from the lower to higher N_a for D>15 nm and D>50 nm.

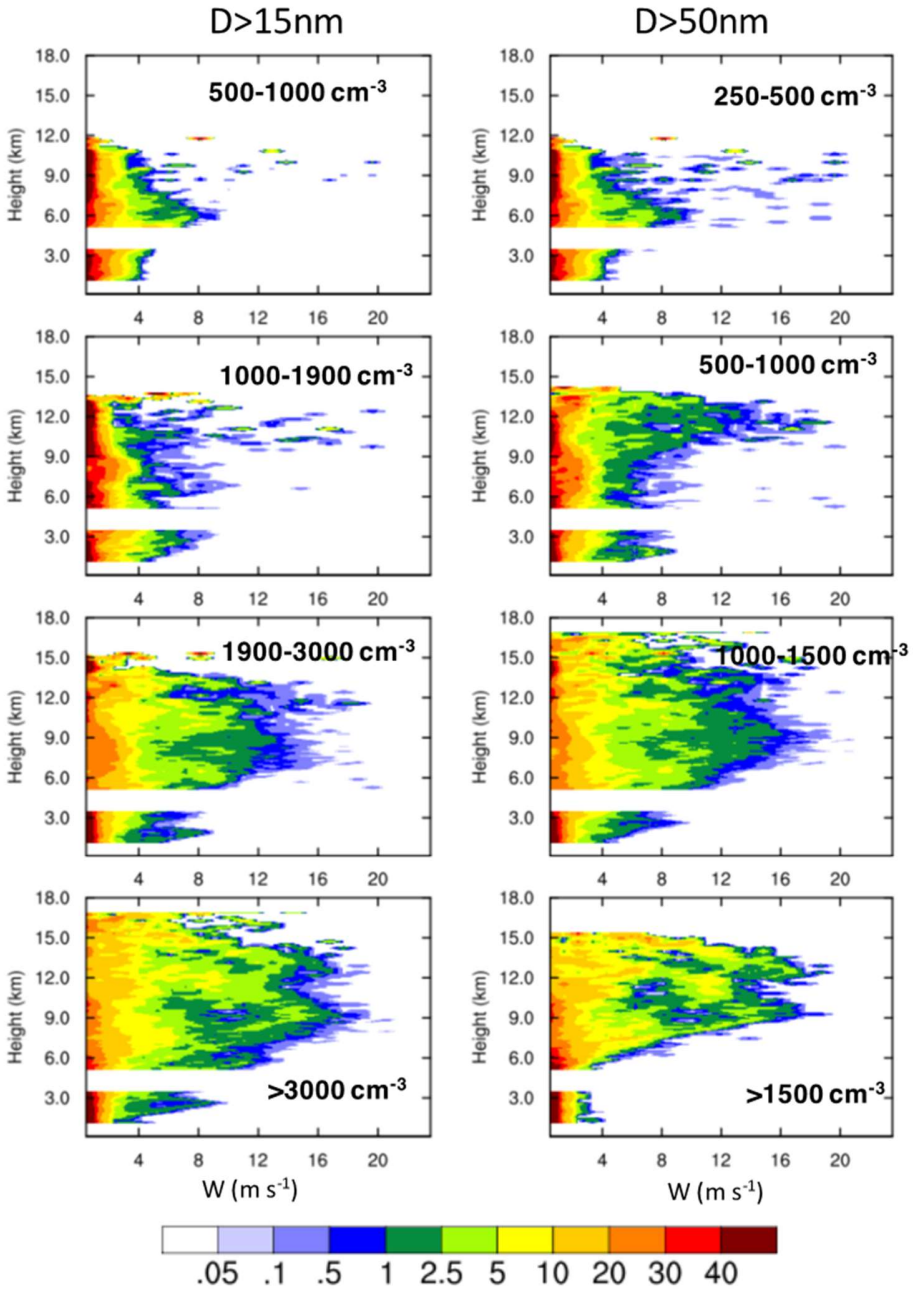

Figure 3.3 Vertical profile of PDF (unit: %) of the updraft speeds (*w*; m s^{-1}) in convective area for D>15 nm (left) and D>50 nm (right) for the four aerosol groups. For each aerosol group, the frequency for w in each bin is calculated using an interval of 1 m s^{-1} with the number of points divided by the total convective points of the group (i.e., sum of the convective points from the cases of the group).

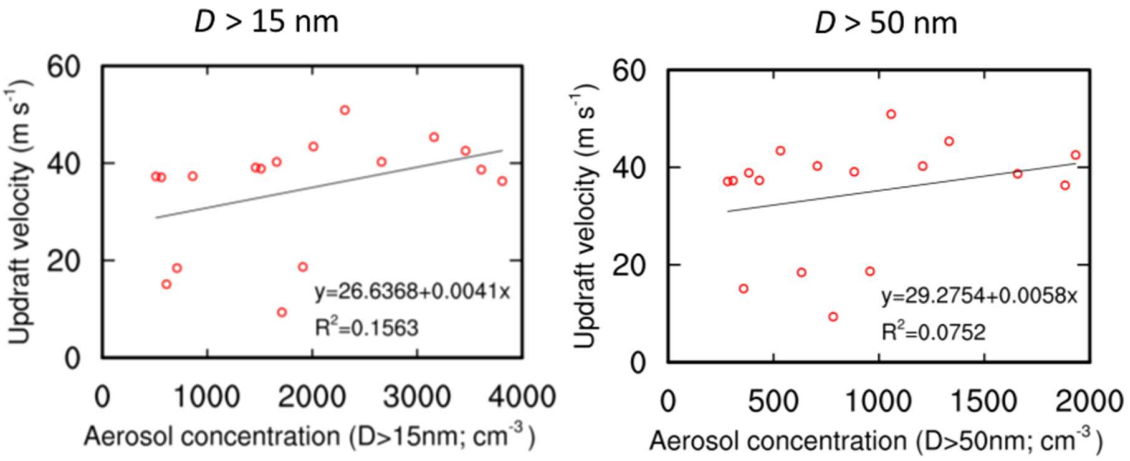

Figure 3.4 The correlation of the maximum velocity averaged over the top 10 percentile of updrafts in each case with aerosol concentrations for D>15 nm and D>50 nm.

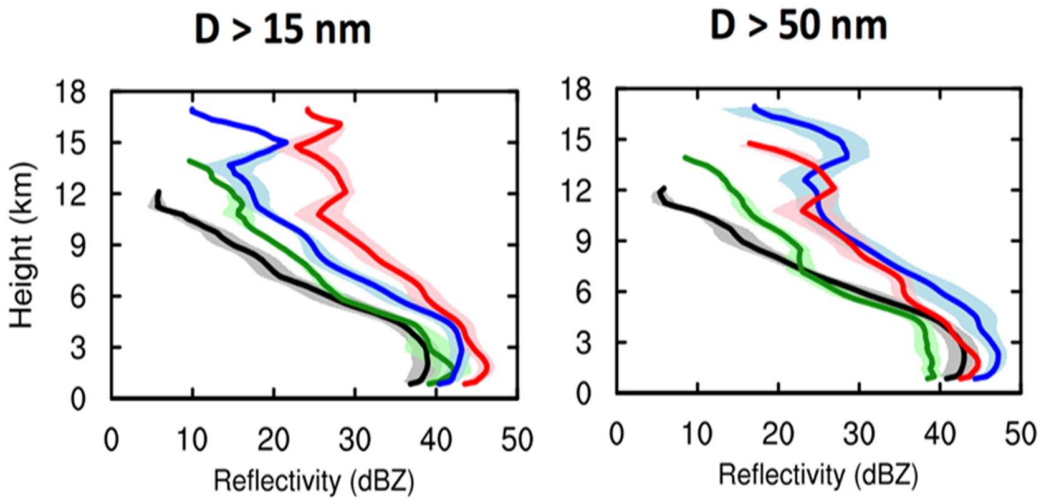

Figure 3.5 Vertical profiles of reflectivity averaged over the top 10 percentile of updrafts for each case for the four aerosol groups and standard error (shaded) from the lower to higher N_a for D>15 nm and D>50 nm.

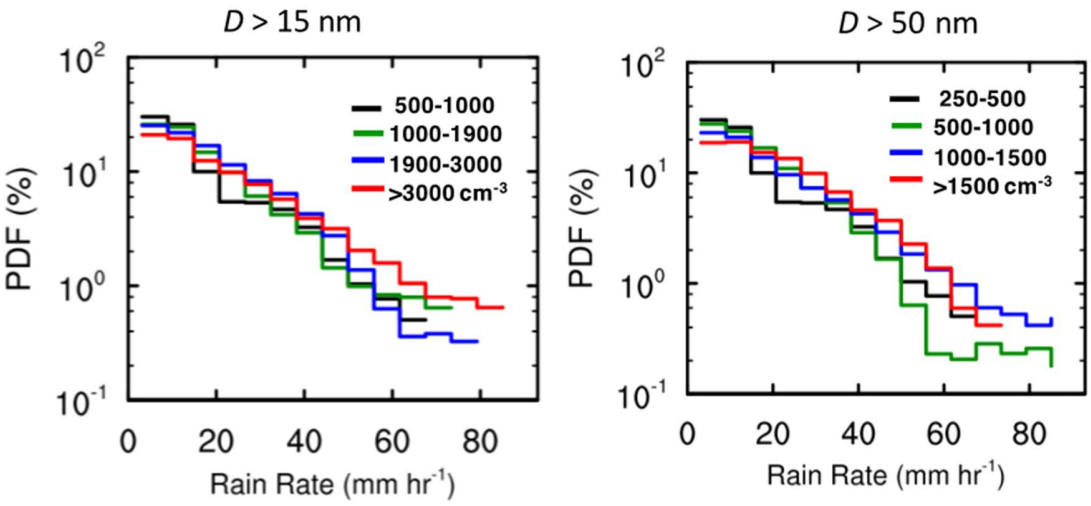

Figure 3.6 The PDFs of the surface rain rates stratified according to the four aerosol groupings for D>15 nm and D>50 nm.

To corroborate $UAP_{<50}$ as the main factor contributing to the observed DCC enhancements, additional analyses are conducted to help isolate aerosol effects from thermodynamic controls. Locally driven Amazon deep convective events within the wet season should initiate and evolve under similar diurnal controls on their dynamical and thermodynamical environments (Tang et al. 2016). The traditional radiosonde thermodynamic forcing parameters such as environmental CAPE and CIN before convection are firstly examined. CAPE and CIN values for each convective case are calculated from the nearest available radiosonde launch before the convective event. Because soundings are launched at a minimum of four times per day (up to six times per day in March that is during the Intensive Operation Period 1), the CAPE and CIN calculated in this way should be representative for the respective convective event. The CAPE is very similar for these events (black circles in Figure 3.1) and is not strongly correlated with updraft intensity. Under similar CAPE conditions, CIN magnitudes should help convey the

propensity for DCCs to initiate and relate its relative intensity. CIN varies quite a bit (triangles in Figure 3.1) but again shows no correlation with the enhanced convective intensity as $UAP_{<50}$ increase. Deep cloud development may also be contributed from boundary layer dynamics and middle-level moisture. To help exclude other factors that might contribute to the relationship between updraft velocity and aerosols in addition to CAPE and CIN, changes in profiles of temperature, relative humidity, zonal (U) and meridional (V) component winds (also from nearest sounding for each case) from the lower to higher aerosol grouping are examined as shown in Figure 3.7. Furthermore, large-scale convergence before convection calculated from the National Center for Environmental Prediction final analysis data (NCEP/FNL) at 0.5-degree resolution is also examined in Figure 3.8. From those plots, none of these factors seem to explain an increasing relationship of updraft intensity with the increase of $UAP_{<50}$. In fact, the lowest N_a group exhibits higher RH at 2- to 5-km altitudes compared with higher N_a groups, which should have favored stronger convection and offset some aerosol effects. This means that the trend for enhanced updraft intensity with the increase of $UAP_{<50}$ should have potentially been more prominent if RH for the lowest N_a group is similar to the higher N_a groups.

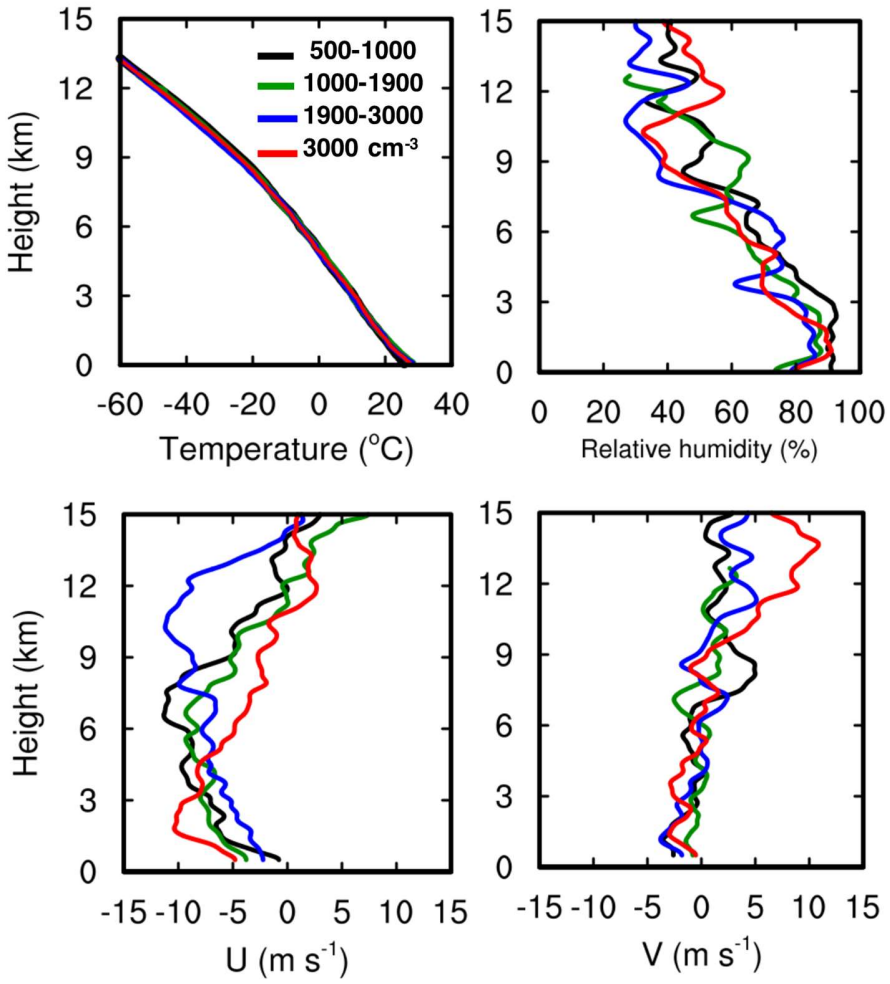

Figure 3.7 Vertical profiles of temperature, RH, zonal U- and meridional V-winds stratified according to the four aerosol groups for D>15 nm.

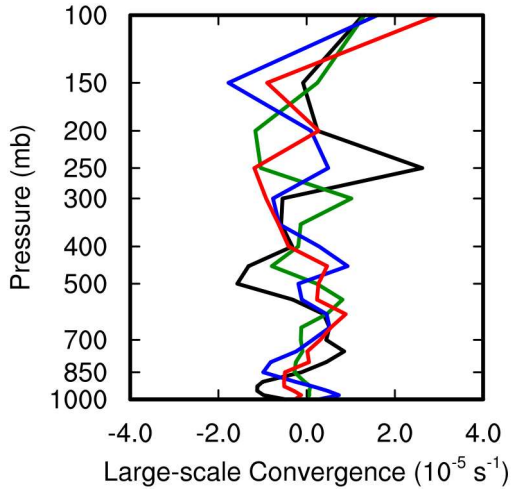

Figure 3.8 Vertical profiles of large-scale convergence stratified according to the four aerosol groups for D>15 nm.

Although RWP observations are not guaranteed to capture the representative updraft cores for every single event, these analyses do not show any covariation of aerosols with dynamics and thermodynamics for these locally occurring systems**.** This provides clear evidence that the enhanced convective intensity seen with the increase of $UAP_{<50}$ is not solely controlled by factors other than the $UAP_{<50}$.

3.3 Modeled experiments and evaluation

To understand the physical processes and mechanisms responsible for the observed intensification of updrafts by $UAP_{<50}$, we conducted model simulations at a cloud-resolving scale of 0.5 km for a typical wet season convective event, as on 17 March 2014 (one of the 17 cases in above observation analysis). The local convective cells were observed at 1600-1900 UTC around the T3 site where the U.S. Department of Energy ARM Mobile Facility was located (Figure 3.9) during GoAmazon2014/5, by the X-band radar located at the T3 site and the S-band radar (SIPAM) located at the Manaus metropolis (near the T1 site), 67.8 km northeast of the T3 site. The radar reflectivity reached its largest values at 1800-1830 UTC (Figure 3.9). The low-level wind was northeasterly (Figure 3.10), favoring the transport of the Manaus pollution plume to the T3 site. The cloud bases were warm (about 20 °C) with weak wind shear in the lower troposphere. The estimated CAPE value was very high (around 4500 J kg^{-1}) approximately 2 h before the initiation of convection.

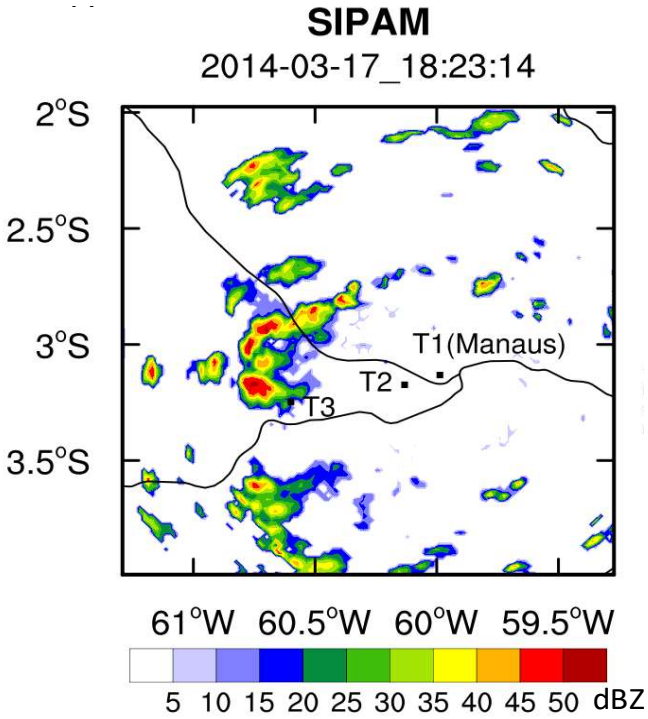

Figure 3.9 The composite radar reflectivity (i.e., the column maximum) from the SIPAM radar at 1824 UTC 17 March 2014.

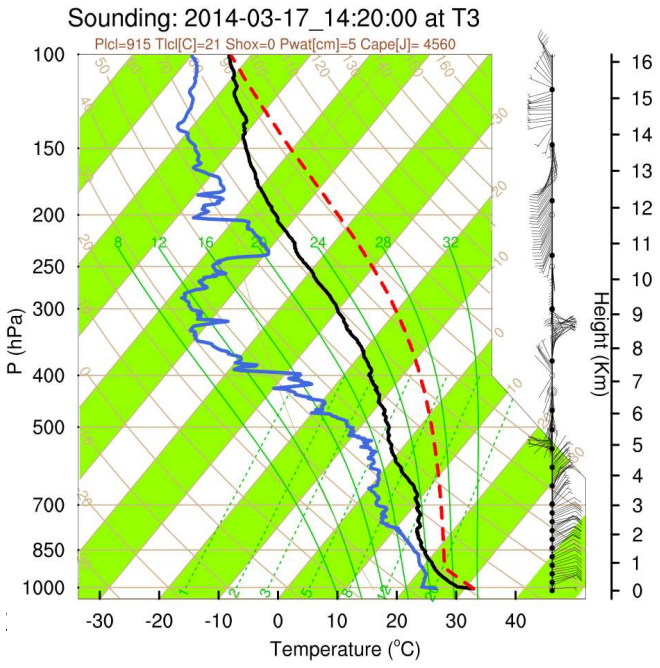

Figure 3.10 Skew-T plot for the sounding data at 1420 UTC at the T3 site.

We use WRF v3.6.1 with SBM (Khain et al., 2004) to simulate this locally occurring system on 17 March 2014. Two nested domains with horizontal grids of 1 and 0.5 km are used (Figure 3.11) with 51 vertical levels up to 50 hPa. The numbers of horizontal grid points for Domain 1 and Domain 2 are 1000×1000 and 450×450, respectively. The Domain 1 simulation, designed for better simulating the synoptic and meso-scale processes, is driven by NCEP/FNL at 1-degree horizontal resolution and 6-h temporal intervals and run with the Morrison two-moment microphysics scheme. With the purpose of avoiding using grey-zone resolutions (4-50 km in cumulus parameterization), 30 grid points for each side of the lateral boundaries in Domain 1 are employed to buffer the "jump" from the 1-degree NCEP/FNL data to 1-km horizontal grid spacing. The land surface data used for the simulations were the best available products for South America. The soil moisture is from an operational product from Center for Weather Forecasting and Climate Research/National Institute of Space Research (CPTEC/INPE) in Brazil, which is a daily product at 0.25 degree. The surface albedo, vegetation, and green fraction used in this study are documented in Beck et al., (2013). Domain 2 with the SBM is driven by the initial and lateral boundary meteorological conditions derived from Domain 1 outputs with the lateral boundary conditions updated every 3 h using the "ndown" approach. The SBM employed is the fast version, which solves a system of kinetic equations for the size distribution functions of water drops, ice crystals/snow, graupel, as well as CCN. The diffusional growth processes (i.e., condensation/evaporation and deposition/sublimation) in SBM are calculated with theoretical equations based on the predicted supersaturation and particle size. In order to better compare the simulation and radar observation, a polarimetric simulator from Alex Khain and Alex Ryzhkov is newly incorporated into this version of

SBM. The Yonsei University planetary boundary layer scheme, Unified Noah land surface scheme, and the rapid radiative transfer model for general circulation model (RRTMG) longwave and shortwave radiation schemes are also used. Cumulus parameterization was not needed for the simulations in both domains. The modeled dynamic time step was 5 s for 1-km resolution and 3 s for 0.5-km resolution, and simulations were initiated at 1200 UTC on 16 March, and run for 36 h.

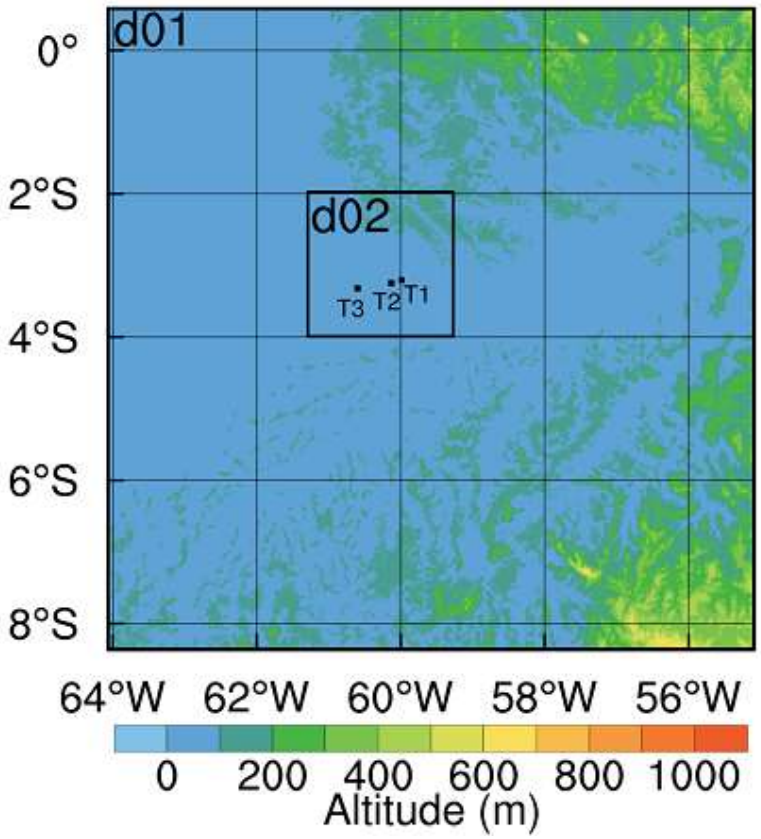

Figure 3.11 The simulation Domain 1 (d01) and Domain 2 (d02) with background of surface height (m).

Table 3.2 Model simulations for T3 case. Abbreviations: BG, present-day background aerosol condition in the Manaus region; PI, preindustrial aerosol condition; P3, factor of 3 increase in *N*a for plume; C, clean condition (i.e., no plume); L in PL3, large aerosol particles (i.e., $D > 50$ nm). Peaked refers to a measured size distribution that has a peak

value over a size range; upper-level peak refers to a measured vertical distribution with aerosols peaked at upper levels (Andreae et al. 2018). N/A means that no plume is applied (i.e., aerosols are horizontally uniform over the domain at the model initial time).

Simulation	Acronym	SD	VD	Hygroscopicity (κ)	N_a of domain (cm^{-3})		N_a of Manaus pollution plume (cm^{-3})	
					$CCN_{>50}$	$UAP_{<50}$	$CCN_{>50}$	$UAP_{<50}$
Manaus regional background with pollution plume	P3_BG	Power law + peaked	Exponential decrease	0.12	130	820	390	2460
Manaus regional background	C_BG	Power law + peaked	Exponential decrease	0.12	130	820	N/A	N/A
Pre-industrial condition without $UAP_{<50}$	C_PI	peaked	Exponential decrease	0.12	130	0	N/A	N/A
Sensitivity test for P3_BG without $UAP_{<50}$	PL3_PI	peaked	Exponential decrease	0.12	130	0	390	0
Sensitivity test for VD based on C_BG	C_BG_VD	Power law + peaked	Upper-level peak	0.12	130	820	N/A	N/A
Sensitivity test for VD based on C_PI	C_PI_VD	peaked	Upper-level peak	0.12	130	0	N/A	N/A
Sensitivity test for SD based on P3_BG	P3_BG_SD	Peaked	Exponential decrease	0.12	450	3350	1350	10050
Sensitivity test for SD based on C_BG	C_BG_SD	Peaked	Exponential decrease	0.12	450	3350	N/A	N/A
Sensitivity test for SD based on C_PI	C_PI_SD	Peaked	Exponential decrease	0.12	450	0	N/A	N/A
Pre-industrial condition with $UAP_{<50}$	C_PI2	Peaked	Exponential decrease	0.12	130	60	N/A	N/A
Sensitivity test for C_PI with mean ATTO	C_PI_ATTO	Peaked	Exponential decrease	0.12	200	0	N/A	N/A
Sensitivity test for C_BG with $CCN_{>50}$ from mean ATTO	C_BG_ATTO	Peaked	Exponential decrease	0.12	200	820	N/A	N/A

Table 3.2 summarizes the major simulations for Domain 2. C_BG is the simulation with a present-day background N_a in the Manaus region of 950 cm^{-3} (130 for $CCN_{>50}$ and 820 for $UAP_{<50}$) near the surface. The plume affected case is P3_BG, which is based on C_BG, but N_a at the Manaus metropolis (black box in Figure 3.12) is increased by three times (based on aircraft observation) and set as a constant plume source during the model simulation to mimic the observed Manaus pollution plume. Aerosol size distribution (SD) is shown in Figure 3.14B. For $UAP_{<50}$, the power-law relationship followed the observed shape in the Manaus city (Line 1 in Figure 3.14A). The total $UAP_{<50}$ concentration of 2460

cm^{-3} in the P3_BG was set to obtain cloud droplet concentrations of about 300 cm^{-3}, which is within the range of 200-600 cm^{-3} for the plume-affected warm clouds observed for this case by aircraft. For $CCN_{>50}$, the SD shape was adopted from measurements under near-pristine conditions at the remote rainforest site of the Amazonian Tall Tower Observatory (ATTO) in the central Amazon Basin (Figure 6a in Pöhlker et al. 2018) and scaled to 130 cm^{-3} of $CCN_{>50}$ (35^{th} percentile of measurement data under near-pristine conditions) as illustrated in Figure 3.14D (dashed line). The hygroscopicity (κ) value used for activation is 0.12, based on the measured κ for urban pollution during the 2014 wet season that is generally between 0.1-0.15 for aerosols smaller than 100 nm (Thalman et al. 2017). The aerosols are horizontally homogeneous over the domain. In this simulation, the aerosol plume was transported from the Manaus metropolis to the T3 site by the northeasterly wind at low levels, and Figure 3.12 shows how the aerosol plume looks at 1200 UTC on 17 March (after 1-d simulation). The three-times-higher aerosol concentrations in the plume were based on the CCN measurements at the 0.23% supersaturation on the aircraft for this case, which shows about 2-4 times increase from the background to the plume conditions. Over the Amazon rainforest without disturbance by human activities (note this is different from the present background condition mentioned above), the aerosol concentration is close to a clean pre-industrial (PI) condition, and $UAP_{<50}$ are very low in concentration due to the lack of particle nucleation events in the isoprene-dominated environment. To mimic the PI aerosol condition and isolate the contribution of $UAP_{<50}$ that are produced by Manaus pollution plume to the increased convective intensity and precipitation from C_BG to P3_BG, another pair of simulations are carried out, C_PI and PL3_PI based on C_BG and P3_BG, respectively, except that $UAP_{<50}$ (i.e., particles with a diameter less than 50 nm)

was removed in both background and plume conditions (Figure 3.13B and Table 3.2). Therefore, the initial N_a became 130 and 390 cm^{-3} for C_PI and PL3_PI, respectively.

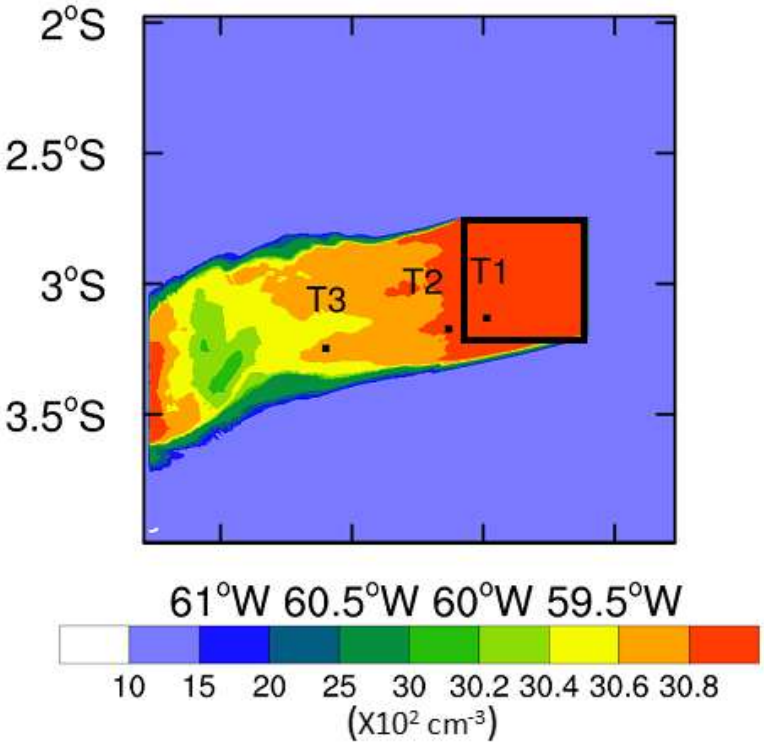

Figure 3.12 Aerosol concentrations after 1-d simulation.

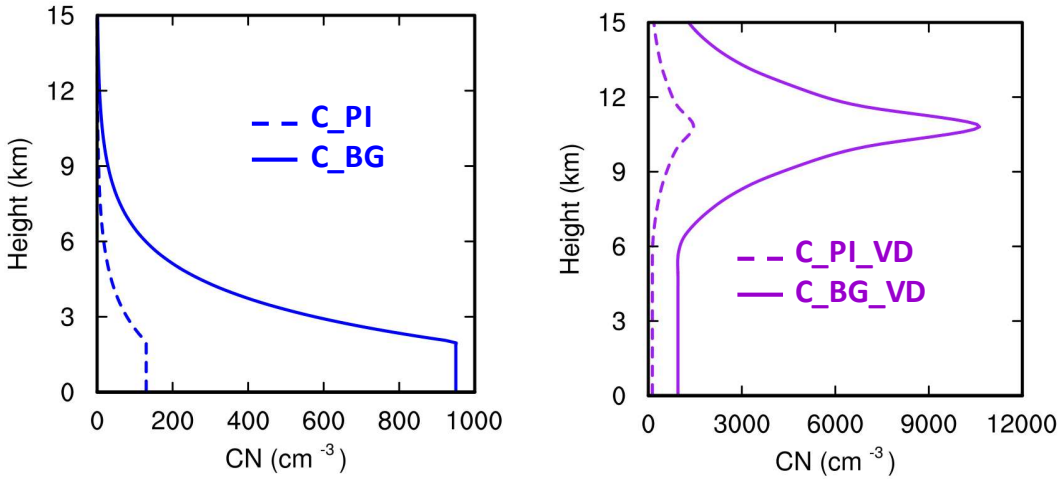

Figure 3.13 Aerosol vertical distribution for (A) C_PI and C_BG, and (B) the tested VD in C_PI_VD and C_BG_VD.

The aerosol concentration was assumed to be uniform within 2 km above the ground and exponentially decrease above 2 km in the four main simulations in Table 3.2 (the first 4 simulations). A new observational study showed that aerosol concentration peaks at the upper troposphere over the Amazon region (Andreae et al., 2018). To look at whether the high concentration of aerosols at upper levels could impact our results, sensitivity tests are conducted by using a similar VD as in Figure 7b of Andreae et al., 2018. That is, aerosol concentration is kept as a constant below 6 km (Figure 3.13B), and an exponential increase from 6 to 11 km. An exponential decrease is assumed above 11km. Two tests (C_BG_VD and C_PI_VD) were performed corresponding to the original simulations of C_BG and C_PI (Table 3.2), respectively, except using the new vertical distribution. The aerosol concentration below 6 km altitude in C_BG_VD and C_PI_VD is set to be the same as that of C_BG and C_PI below 2 km (Figure 3.13A), respectively. The highest concentration at upper levels is about 11 times larger than that below 6 km, consistent with Figure 7b of Andreae et al. 2018.

Aerosol SD could vary significantly. To examine if our conclusions are affected by a different SD, we performed sensitivity tests by employing a SD measured at about 20 km downwind of the Manaus city (Line 2 in Fig. 3.14A). Lines 3 and 4 are further downwind with Line 4 around the T3 area, where $UAP_{<50}$ are much lower. Also, aerosols measured at these locations likely went through cloud processing because of cloud and precipitation occurring nearby. Thus, Line 2 is chosen to represent the plume condition in the sensitivity tests. Three tests were conducted following the same setup as the previous simulations except for a different SD (Table 3.2): the plume case P3_BG_SD, the present-day background case C_BG_SD, and the PI case C_PI_SD (Figure 3.14C). The total aerosol

concentration of Line 2 is about 1.14e4 cm^{-3}, which is very high due to contribution of $UAP_{<50}$.

Because all $UAP_{<50}$ are removed in the PI condition to examine the contribution of $UAP_{<50}$, to show that our conclusion and the proposed mechanism are not impacted by a small amount of $UAP_{<50}$ in the PI condition, we conducted an additional sensitivity test C_PI2 (Table 3.2), in which 60 cm^{-3} of $UAP_{<50}$ were added to the SD of C_PI (Fig. 3.14D). The SD for C_PI2 was based on measurements at the remote site ATTO in the central Amazon Basin (a present-day pristine condition, Fig. 6a of Pöhlker et al. 2018) and scaled to a total N_a of 190 cm^{-3} with $UAP_{<50}$ of about 60 cm^{-3}. This value of N_a is an approximated PI condition, which is at the low end of the range of observations under the present-day pristine conditions (35^{th} percentile with regard to $CCN_{>50}$) while the SD shape is similar to the average rainforest aerosol SD for both present-day pristine conditions (Fig. 6a of Pöhlker et al. 2018) and the entire wet season (Fig. 6 Pöhlker et al. 2016). The hygroscopicity used is 0.12, the same as other simulations.

We also conducted the sensitivity tests C_PI_ATTO and C_BG_ATTO (Table 3.2) for testing the addition of $UAP_{<50}$ condition to the present-day pristine $CCN_{>50}$ condition. The size distributions for these simulations were based on C_PI and C_BG, respectively, with the mean number of $CCN_{>50}$ (200 cm^{-3}) averaged over all measurements under present-day pristine conditions at the ATTO site (goldenrod line in Fig. 3.14D) (Pöhlker et al. 2018).

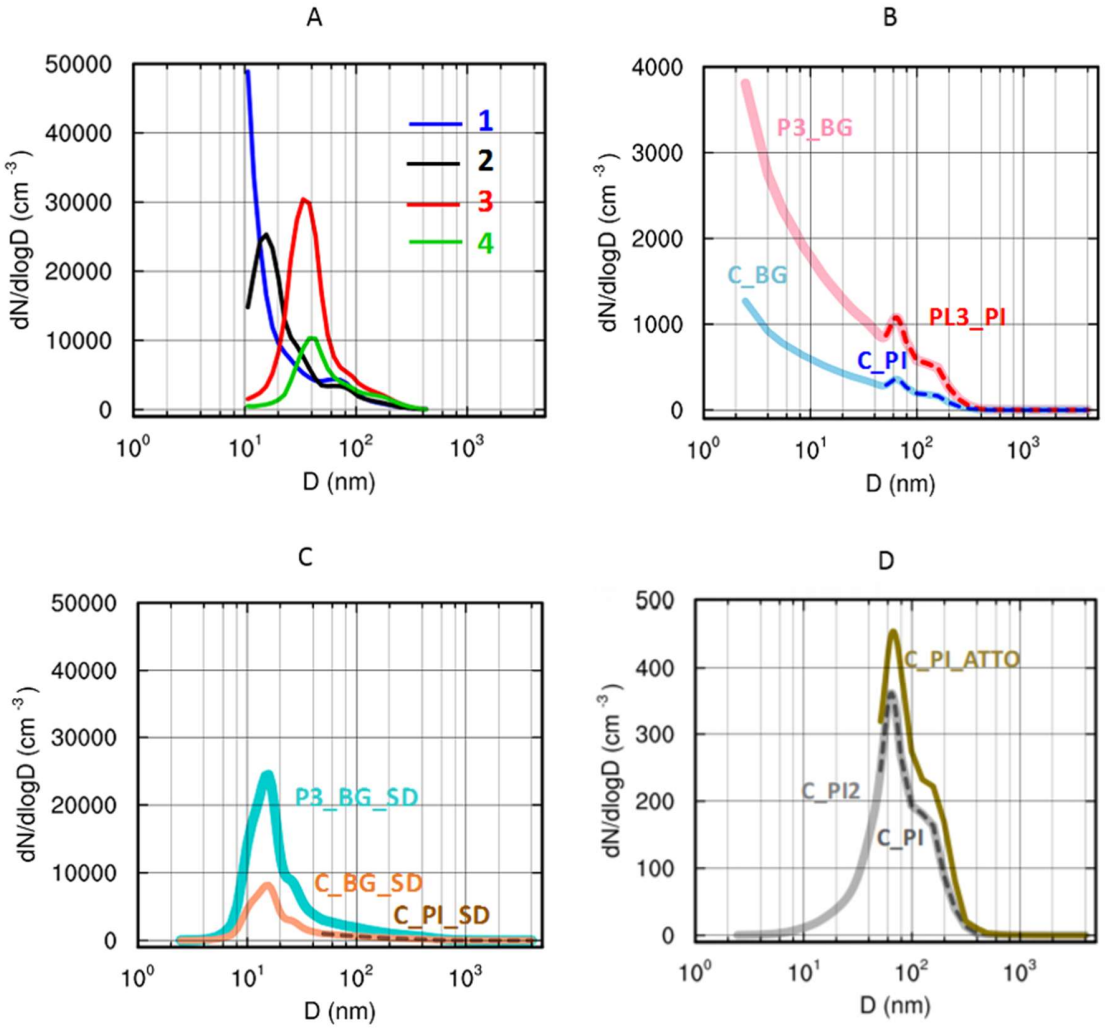

Figure 3.14 Aerosol size distribution from Fast Integrated Mobility Spectrometer (FIMS) measurements on aircraft (A) and model simulations C_PI, PL3_PI, C_BG and P3_BG (B), and C_PI_SD, C_BG_SD, and P3_BG_SD (C), and C_PI2 (D). In Figure 3.14A, line 1 is for the location of inside Manaus. Line 2, 3, and 4 are for the locations of 20 km, 40 km, and 70 km downwind Manaus, respectively. Line 4 is near T3.

The baseline simulation P3_BG was evaluated with available observations in meteorology, clouds, and precipitation. Figure 3.15 shows that the simulated profiles of temperature, water vapor, and wind fields agreed well with sounding observations at the T3 site at 14:20 UTC. For cloud properties, the aircraft only sampled select shallow warm clouds at flight levels around 1-km altitude between the Manaus metropolis and the T3 site;

thus, the sampling was not representative of the deep convective clouds that are analyzed around the T3 site. Due to limited sample size (less than 10 min in-cloud measurements) and large variability of the measured cloud droplet concentration (1-800 cm^{-3}) sampled by aircraft over a long distance, it was difficult to compare the data with the simulations. In general, the cloud droplet concentrations around cloud center at the 1-km altitude for the plume-affected region were 200-600 cm^{-3}, and the corresponding modeled values in P3_BG were generally within that range. Again, these values were for the shallow clouds, not the deep convective clouds around the T3 site.

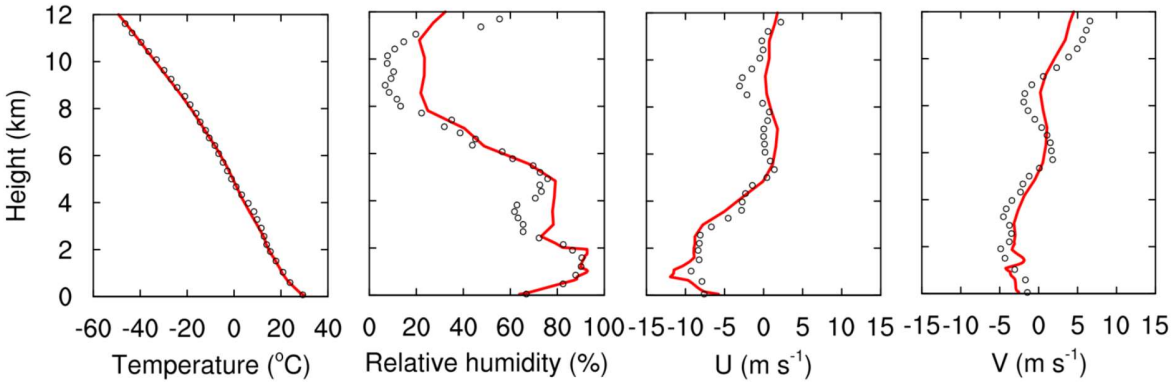

Figure 3.15 Comparison of the temperature, RH, U- and V-winds from the sounding data at 14:20 UTC at the T3 site (circle) with those from the same time and location in P3_BG (red).

Fortunately, the S-band and X-band radar measurements can be used as reference for the deep convective cloud properties around the T3 site, although the radars had some missing data during the strong precipitation period between 1736-1824 UTC. Note, the RWP did observe the passage of a moderate convective cell at the T3 site during this period, but it is difficult to compare column measurements with 3-D cloud simulations due to limited sampling over such a short time period (the temporal and spatial shifts of

convection in the simulation further increased the difficulties to compare). The comparison of the retrieved rain rate at around 1824 UTC from SIPAM and X-band radar (estimated at the 2.5-km altitude) with that in P3_BG is shown in Figure 3.16 (PL3_PI is plotted to show the impact of $UAP_{<50}$). The red box is where the observed deep convective event resides and is the analysis area for the plume-affected deep convective cloud systems. The modeled rain rates are also from the 2.5-km altitude and an approximately 20-min time shift is considered based on the time series of rain rate plot in Figure 3.17. The domain shown here is smaller than the modeled domain. The SIPAM retrieved rain rates are generally larger than those estimated by the X-band radar, but both estimates show the rain core around the T3 site (already passed the T3 site by this time). The rain rate intensity from the rain core around the T3 site was well captured by P3_BG, but significantly weaker in all other simulations (i.e., PL3_PI, C_PI, and C_BG). Note that comparison of P3_BG with PL3_PI shows the addition of $UAP_{<50}$ to the plume and background area greatly enhances rain rate not only in the plume-affected area (i.e., around the T3 site) but also in the whole domain. The time series of the rain rate comparison as seen in Figure 3.17 shows that the simulation with the Manaus pollution plume (P3_BG) was able to reproduce the intensity and the timing of the peak rain rate from the rain core around the T3 site. The comparison is based on the convective system around the T3 site (red box in Figure 3.16). The 10-dBZ echo top height from the simulated radar reflectivity for P3_BG agreed well the SIPAM observations during the deep convection cloud period (i.e., after 1700 UTC; Figure 3.18), suggesting qualitatively that observed precipitation-sized particles being lofted to high altitudes by intense convective updrafts were reasonably captured by the simulation. The 10-dBZ echo top height might not be accurate for shallow clouds so the comparison is

shown for 1800-2000 UTC. All these evaluations indicate that the baseline simulation reasonably reproduced the convective intensity and precipitation of the locally occurring system around the T3 site. These observational metrics provide confidence in the model performance.

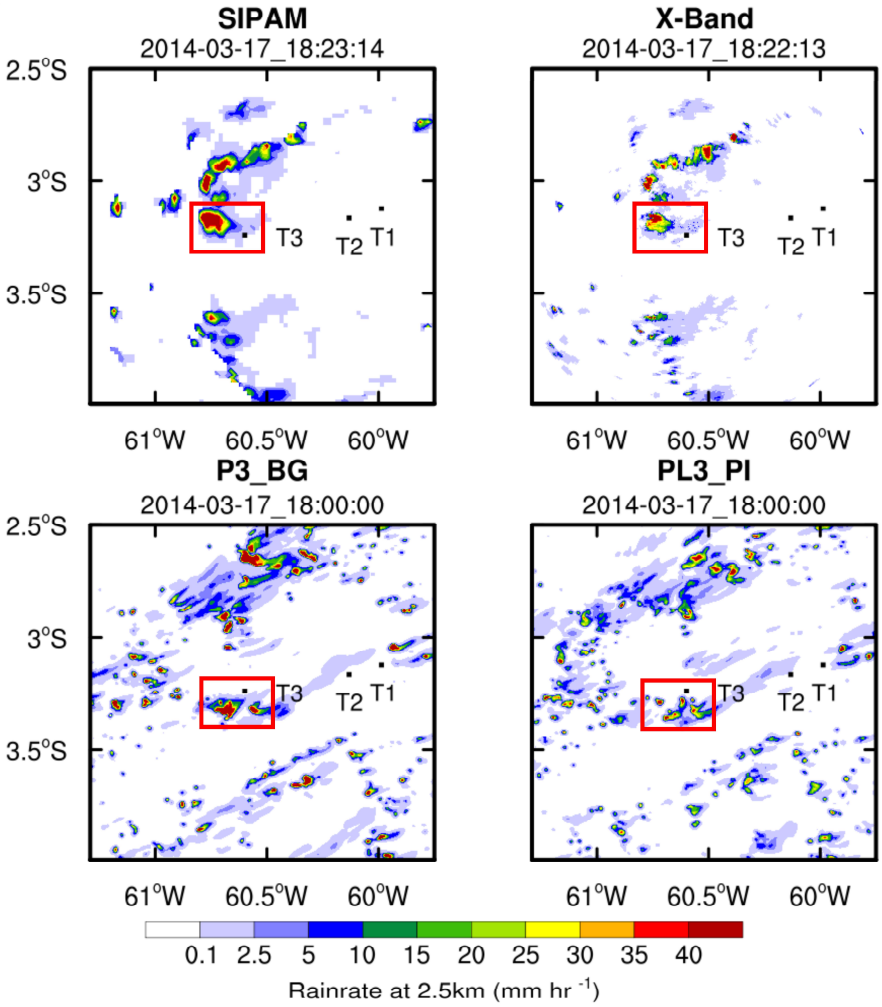

Figure 3.16 Rain rate at 2.5-km altitude from SIPAM, X-band radar, P3_BG, and PL3_PI.

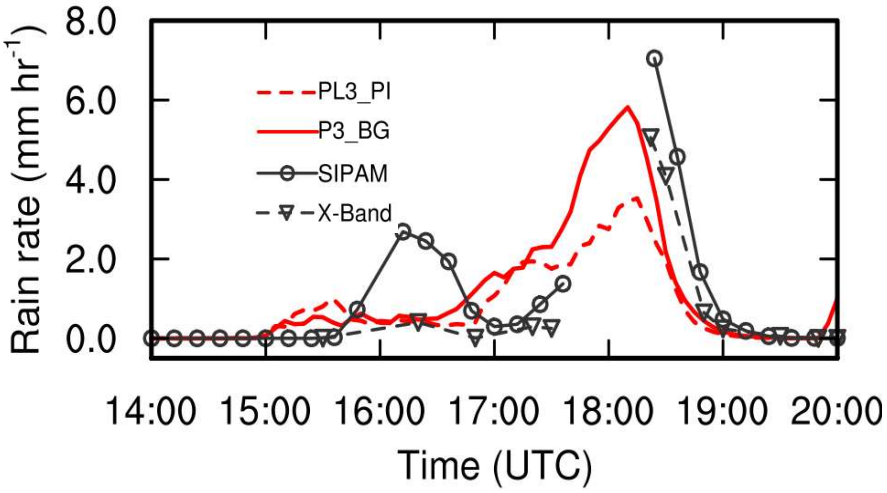

Figure 3.17 Time series of rain rate at 2.5-km altitude from SIPAM, X-band radar, P3_BG. and PL3_PI from SIPAM and P3_BG and PL3_PI.

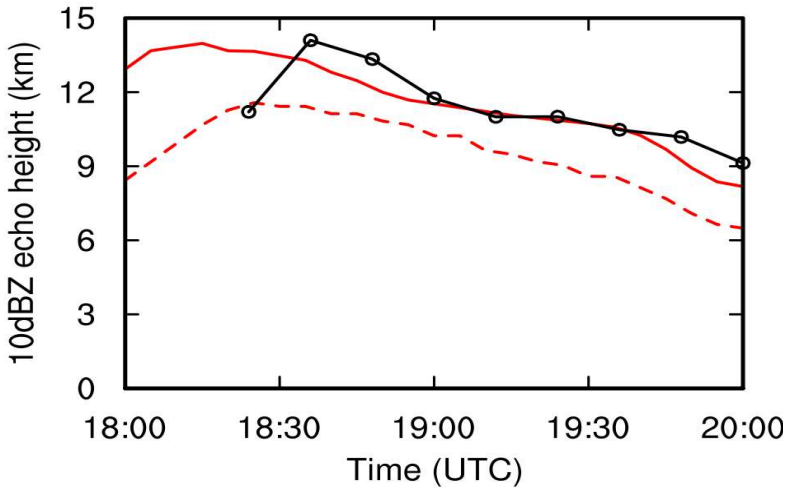

Figure 3.18 Time series of 10-dBZ echo top height from SIPAM and P3_BG and PL3_PI.

3.4 Modeled mechanisms

With the sensitivity tests based on these baseline simulations, adding $UAP_{<50}$ to the PI environment (i.e., lacking $UAP_{<50}$) invigorates convective intensity dramatically (C_PI vs. C_BG and PL3_PI vs. P3_BG in Figure 3.19A). Hereafter, the analysis is mainly focused on the deep convective clouds around the T3 site in red box shown in Figure 3.16 because

they are affected by the Manaus pollution plume in P3_BG and evaluated by observations. The PDFs of updraft velocity clearly convey the same point (Figure 3.20). Therefore, the model replicates the results that were observed: $UAP_{<50}$, which are abundant in the Manaus pollution plume, lead to enhanced convection around the T3 area. The convective intensity is over 50% weaker in the PI environment (C_PI) when compared to the perturbed environment by the urban plume (P3_BG). As a result, the peak rain rate is nearly 2.5 times greater (Figure 3.22). Even under the present-day Manaus regional background condition that already contains a significant amount of $UAP_{<50}$ (820 cm^{-3}), further increasing $UAP_{<50}$ due to the Manaus pollution plume by three times still drastically enhances convective intensity (by about 40%) in the downwind area (P3_BG vs. C_BG). The corresponding increase in the peak precipitation rate is nearly by 100%, much more significant than that of convective intensity.

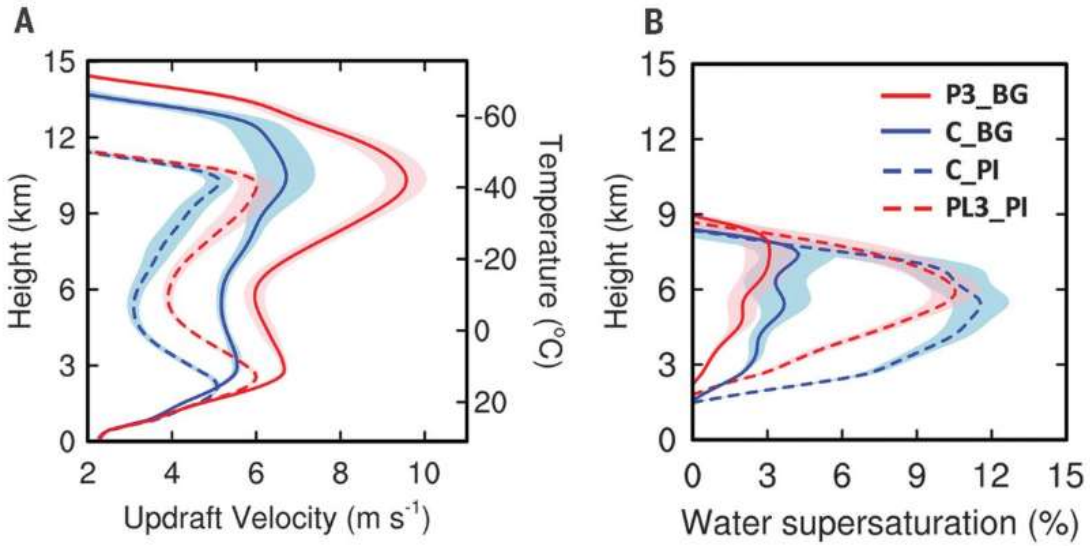

Figure 3.19 Vertical profiles of updraft velocity w (A) and water supersaturation (B) averaged over the top 10 percentiles (i.e., 90th-100th) and standard error (shaded) for the updrafts with w>2 m s^{-1} during 1400-1900 UTC from the convective clouds around the T3 site.

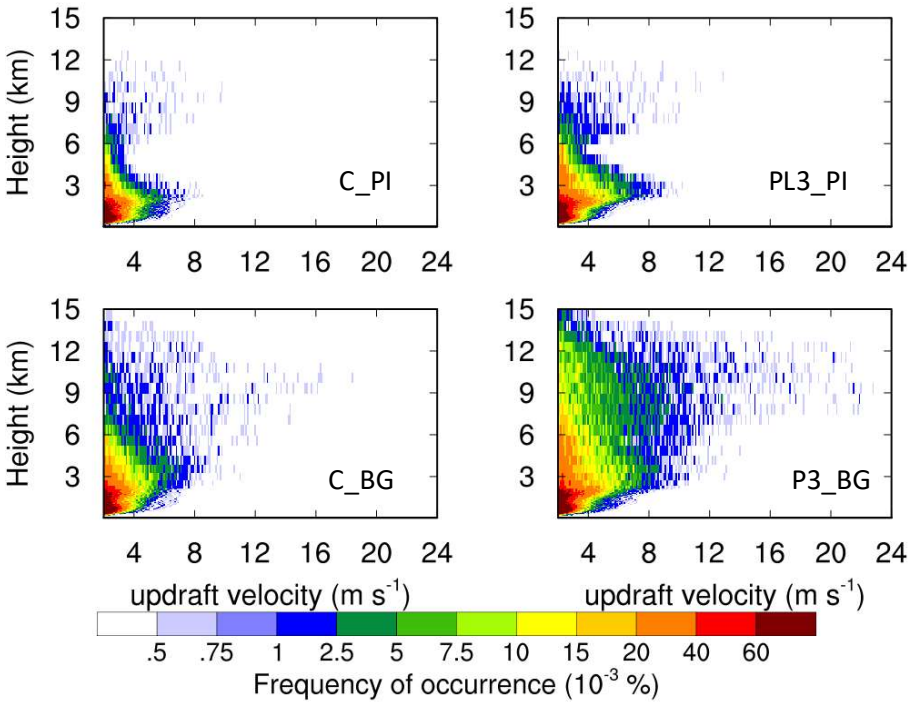

Figure 3.20 Vertical profile of PDF of updraft speeds for w>2 m s-1 from C_PI, PL3_PI, C_BG, and P3_BG during 1400-1900 UTC from the convective clouds around the T3 site. The frequency calculation for each level is based on w ranging from 2 to 24 m s^{-1} with 0.1 m s^{-1} intervals.

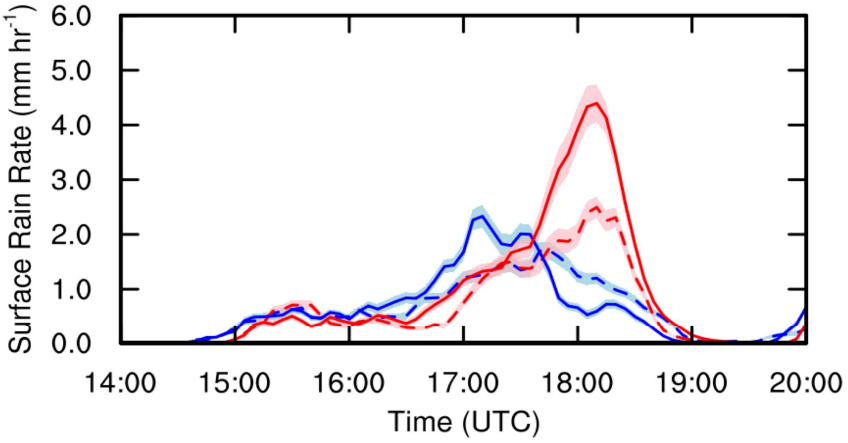

Figure 3.21 Time series of mean surface rain rate averaged over the red box area (Figure 3.16) from simulations of C_PI (blue dashed), PL3_PI (blue solid), C_BG (red dashed), and P3_BG (red solid).

This result highlights the ubiquity of convective invigoration by aerosols in Amazonia (i.e., in both PI and present-day Manaus regional background environments) and the non-linear response of precipitation rates to convective intensity. The ubiquity of convective invigoration by the Manaus pollution plume is also corroborated by more frequent strong updrafts over the entire domain from C_PI to C_BG (Figure 3.22). Another notable feature is that the timing of the peak rain rate is delayed when increasing $CCN_{>50}$ particles, consistent with previous studies. However, adding $UAP_{<50}$ to the same CCN condition does not change the timing, while greatly enhancing the rain rate resulting from enhanced convective intensity. The reason for no change in the timing of rain by $UAP_{<50}$ will be discussed later.

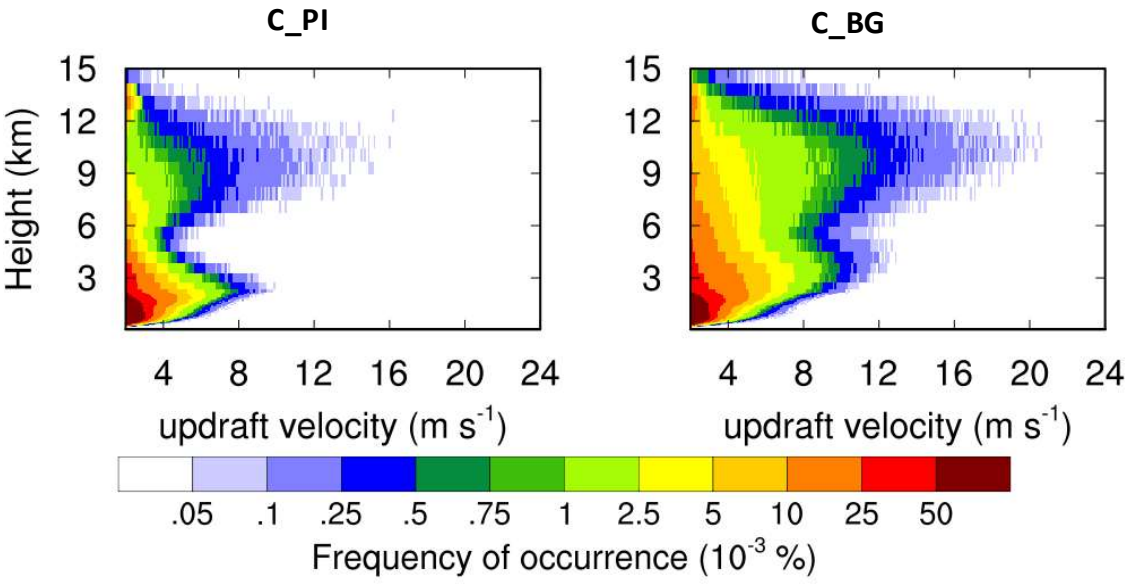

Figure 3.22 Vertical profile of PDF of updraft speeds for w>2 m s-1 from C_PI, PL3_PI, C_BG, and P3_BG over the entire domain.

Further analysis shows that the mechanism responsible for such strongly enhanced convective intensity by $UAP_{<50}$ is different from the "cold-phase invigoration" previously proposed. We used comparisons between C_PI and C_BG to demonstrate our proposed mechanism (similar conclusions were drawn from comparisons between PL3_PI and P3_BG). The warm- and deep-cloud periods were examined. The vertical velocity increase under the deep cloud period correlates with the increase in total buoyancy (no correlation with cold pool intensity is seen), although the condensate loading effect partially offsets the thermal buoyancy (Figure 3.23 and Figure 3.24). The thermal buoyancy includes contributions from both temperature and water vapor variations. The thermal buoyancy increase is attributed to the increased net latent heating (Figure 3.25).

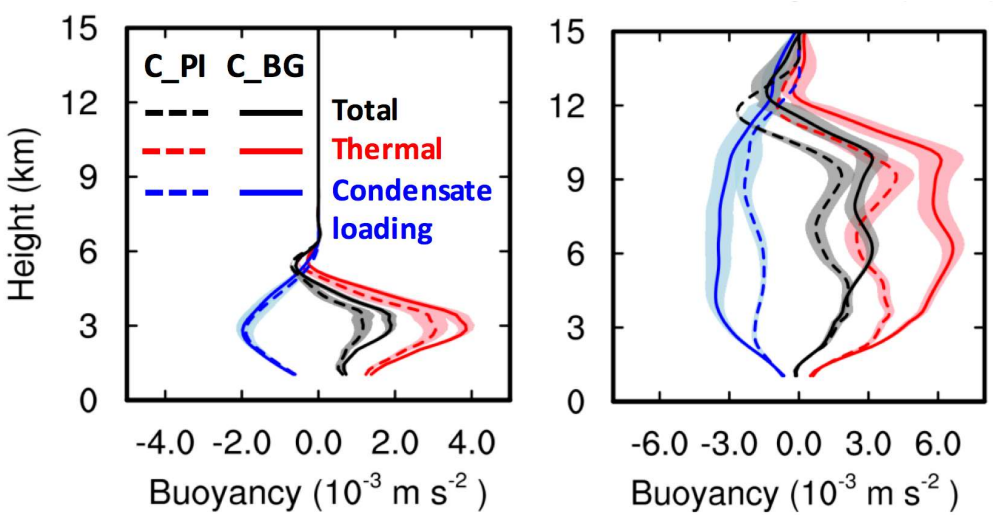

Figure 3.23 Vertical profiles of buoyancy terms and standard error (shaded) for Warm Cloud (left) Deep Cloud (right) from C_PI (dashed) and C_BG (solid). The values for the Warm Cloud are averaged over the top 10 percentile (i.e., 90th-100th) of the updrafts with w>1 m s^{-1} from a 30-min duration after the warm rain starts and rain rate is larger than 0.5 mm h^{-1} for the convective clouds in the red box in Figure 3.16. The values for the Deep Cloud are averaged over the top 10 percentile (i.e., 90th-100th) of the updrafts with w>2 m s^{-1} from a 30-min duration with 15 min before and after the strongest convection.

Therefore, the specific time for the warm and deep cloud periods varies by simulations due to time shift of the convective clouds between the simulations.

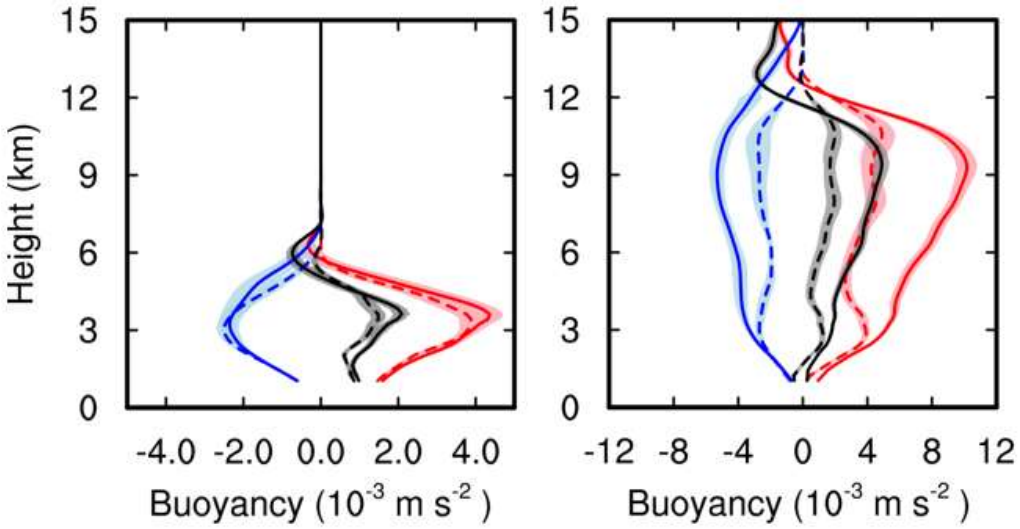

Figure 3.24 Vertical profiles of buoyancy terms and standard error (shaded) for Warm Cloud (left) Deep Cloud (right) from PL3_PI (dashed) and P3_BG (solid).

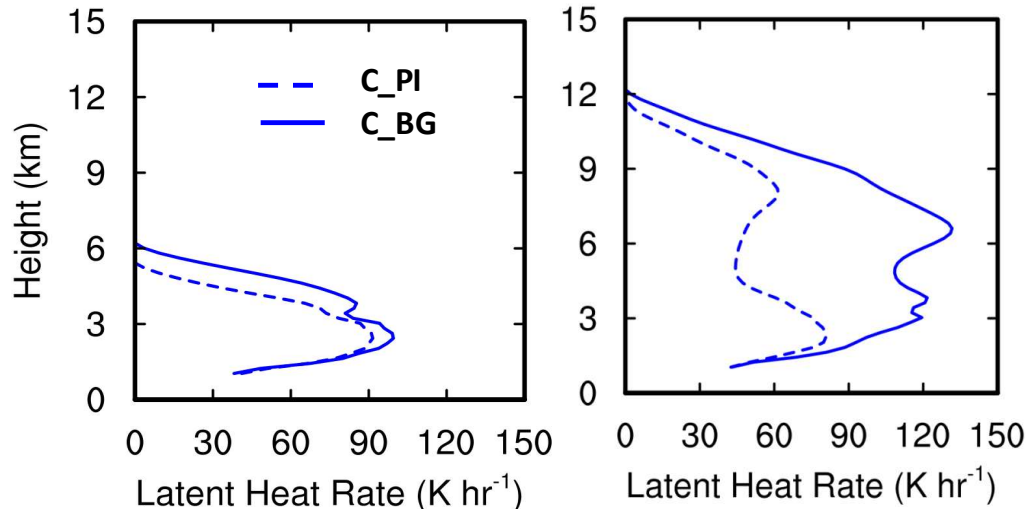

Figure 3.25 Vertical profiles of the net latent heat (heating + cooling) and standard error (shaded) for the warm-cloud period (left) and deep-cloud period (right) in C_PI (dashed) and C_BG (solid).

Next, how latent heating is increased and what microphysical processes are the major contributors are analyzed in detail. In the PI environment (C_PI), for the warm cloud period after warm rain initiates, the mean vapor supersaturation with respect to water (S_w) for the top 10 percentile of updrafts can be nearly 4% (Figure 3.26) because of the efficient warm rain formation due to fast droplet coalescence resulting from large droplet size, which reduces the integrated droplet surface area for condensation (Figure 3.27). The addition of $UAP_{<50}$ (C_BG) brings the S_w down to 1%, because $UAP_{<50}$ form an additional number of droplets above the cloud base, due to smaller critical aerosol size for activation under high S_w (Figure 3.28). These droplets increase the integrated surface area above cloud base by over 40% (Figure 3.27), and therefore promote condensational growth evidently already for the warm cloud period (Figure 3.29). Note, enhanced condensation leads not only to the increased cloud water but also to a rain water increase under the warm cloud period (Figure 3.30). This result is corroborated by aircraft measurements of warm clouds during GoAmazon2014/5, showing larger liquid water content in the plume-affected clouds relative to background clouds; enhanced condensation efficiency is part of the explanation (Cecchini et al., 2016). Under the deep cloud period, the condensation effect is further amplified. The S_w reaches up to 15% in C_PI due to a lack of droplet surface area for condensation and decreases to 7% in C_BG (Figs. 5.31 and Figure 3.32). This allows aerosols as small as 10 nm to be activated into cloud droplets (Figure 3.33). The activation of the $UAP_{<50}$ leads to a 2-4 times increase of the integrated droplet surface area and doubled condensational heating rate (Figure 3.34). The decrease of supersaturation by $UAP_{<50}$ is similarly evident even over the entire convective period 1400–1900 UTC (Figure 3.19B).

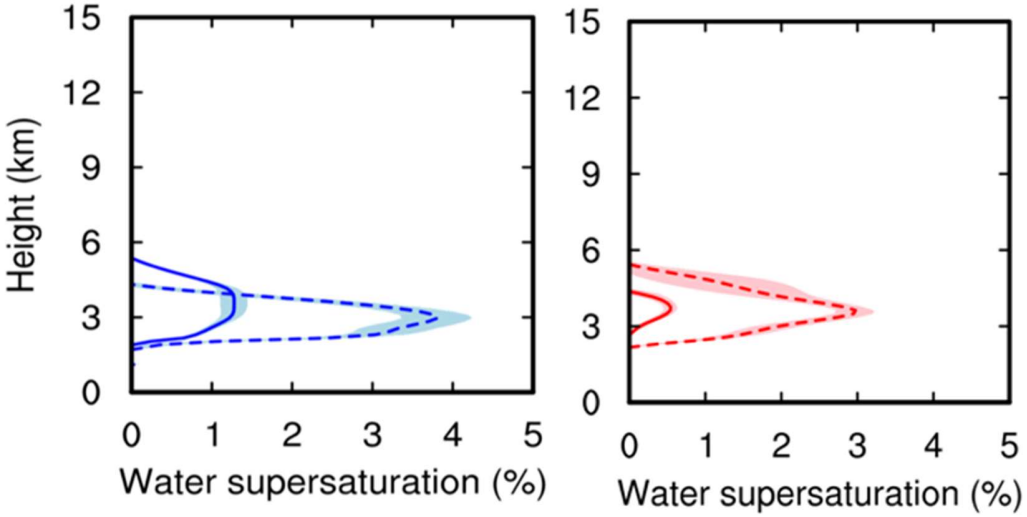

Figure 3.26 Vertical profiles of S_w and standard errors (shaded) for the warm-cloud period in C_PI (blue dashed), C_BG (blue solid), PL3_PI (red dashed), and P3_BG (red solid).

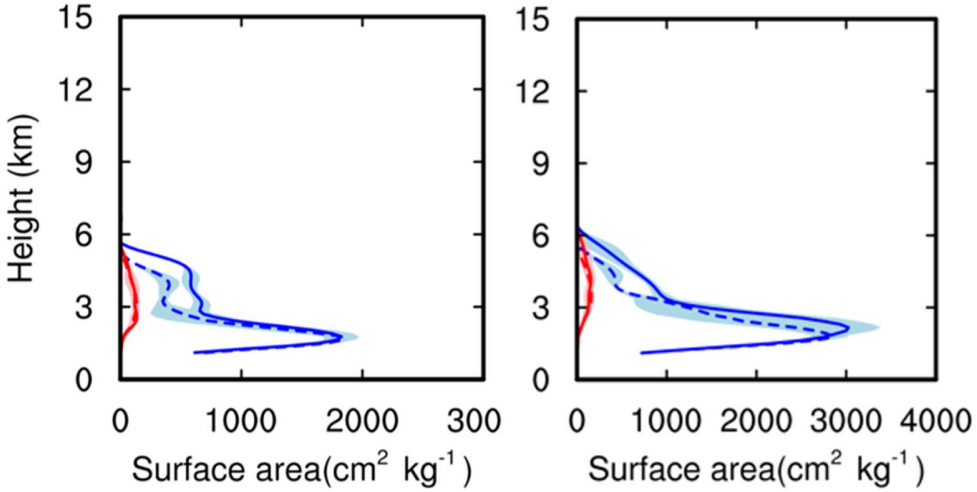

Figure 3.27 Vertical profiles of droplet surface area for cloud droplets (blue), rain drops (red) and standard errors (shaded) for the warm-cloud period in C_PI (left dashed), C_BG (left solid), PL3_PI (right dashed) and P3_BG (right solid).

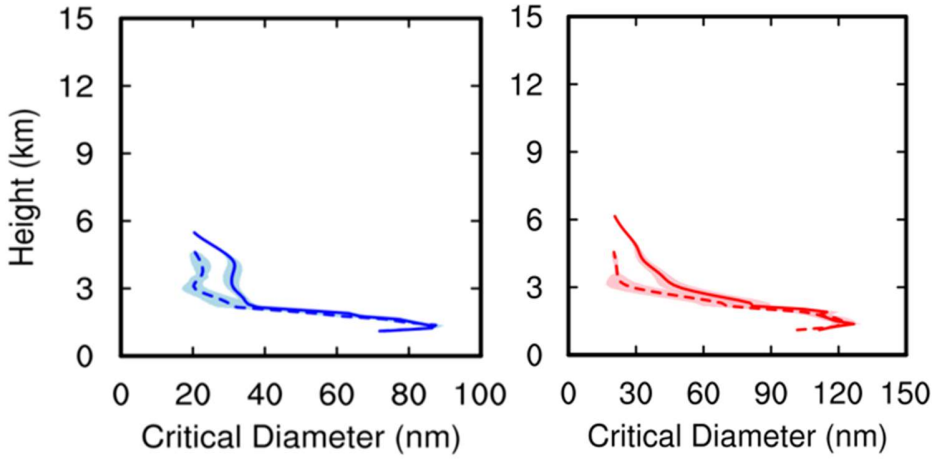

Figure 3.28 Vertical profiles of critical diameter for activation and standard errors (shaded) for the warm-cloud period in C_PI (blue dashed), C_BG (blue solid), PL3_PI (red dashed), and P3_BG (red solid).

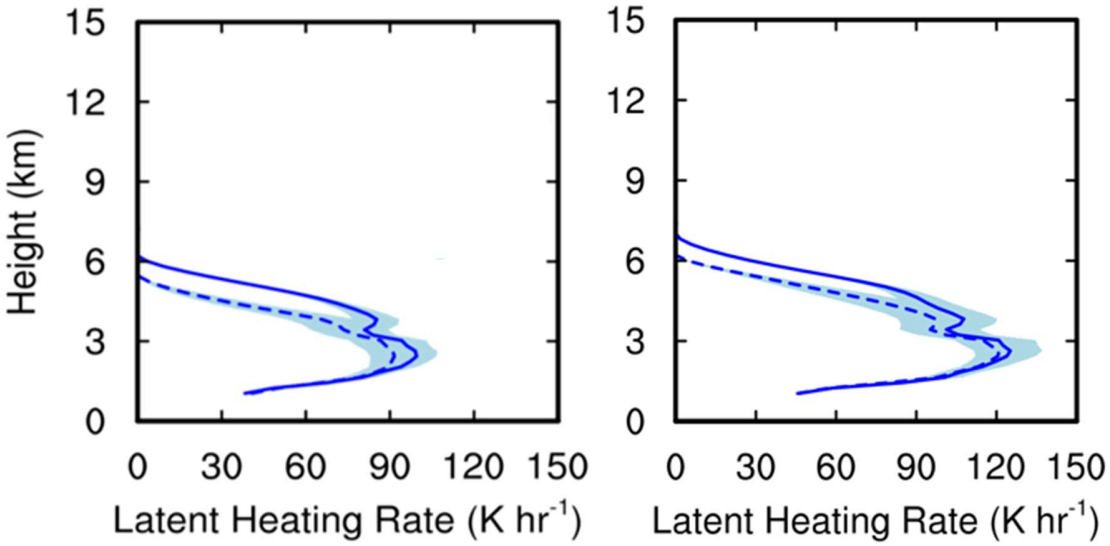

Figure 3.29 Vertical profiles of latent heating from condensation and standard errors (shaded) for the warm-cloud period in C_PI (left dashed), C_BG (left solid), PL3_PI (right dashed) and P3_BG (right solid).

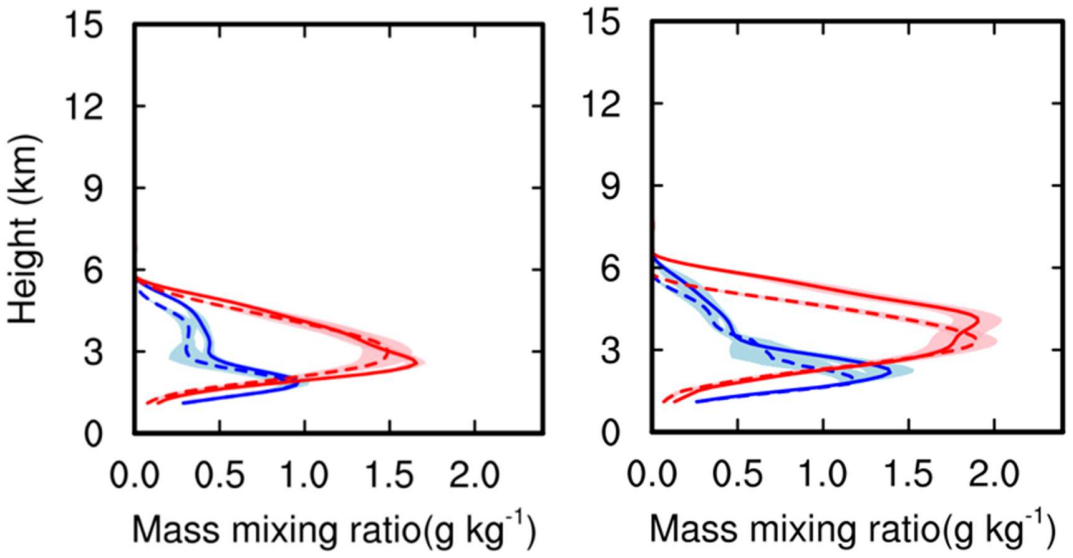

Figure 3.30 Vertical profiles of mass mixing ratios for cloud droplets (blue), rain drops (red), and standard errors (shaded) for the warm-cloud period in C_PI (left dashed), C_BG (left solid), PL3_PI (right dashed) and P3_BG (right solid).

Due to the very small critical size for droplet nucleation at 2.5 to 3-km altitude, another droplet nucleation peak appears above the peak at the cloud base in C_BG due to presence of a significant amount of $UAP_{<50}$ (Figure 3.31). Without $UAP_{<50}$, cloud droplet nucleation occurs predominantly at the cloud base because almost all of the aerosol particles can be activated there (Figure 3.31). The addition of $UAP_{<50}$ makes droplet nucleation occur in a large rate above the cloud base and up to the 8-km altitude due to the transport of $UAP_{<50}$ from low levels. The enhanced droplet nucleation over the profile from C_PI to C_BG leads to an increase of a few times in condensational heating occurring throughout the lower and middle troposphere. The magnitude of condensational heating in C_BG is nearly two times larger than depositional heating, indicating the predominance of the condensation process in latent heat. The increase in depositional heating is also much less than that of condensational heating and only located at 10- to 12-km altitude, noting that

condensational heating is located at low and middle levels and has a deep layer of increase. The latent heating rate from riming and drop freezing is increased considerably from C_PI to C_BG as well. The increases in drop freezing and riming rates result from additional supercooled droplets transported from low levels. Although the increasing rate in latent heating from droplet freezing is the largest, the actual magnitude is too small when compared to other processes to play an important role. The latent heat from riming is also several times smaller than that from condensation and deposition.

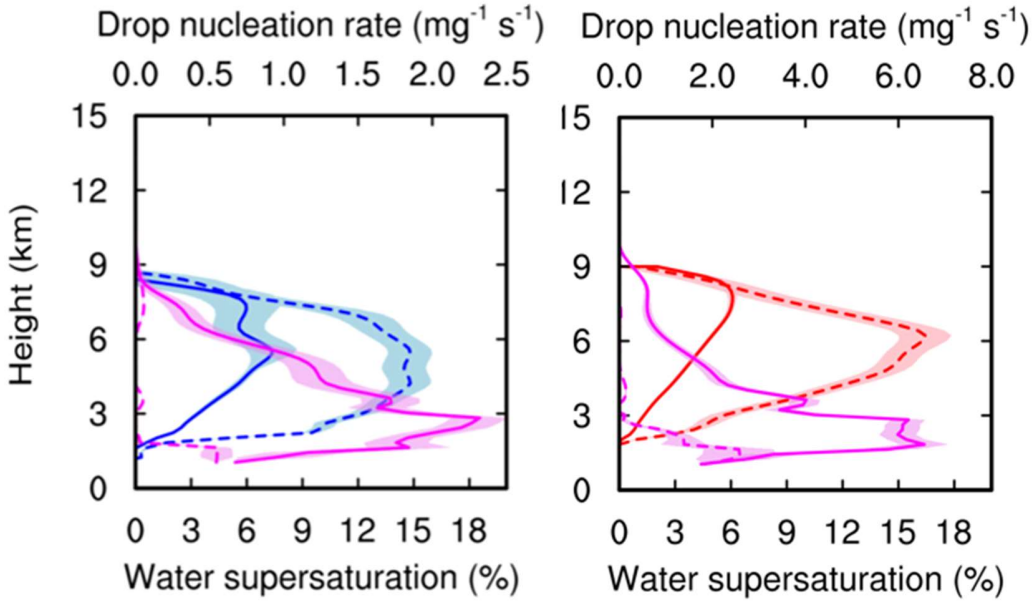

Figure 3.31 Vertical profiles of S_w (blue in left, red in right), droplet nucleation rates (magenta) and standard errors (shaded) for the deep-cloud period in C_PI (left dashed), C_BG (left solid), PL3_PI (right dashed) and P3_BG (right solid).

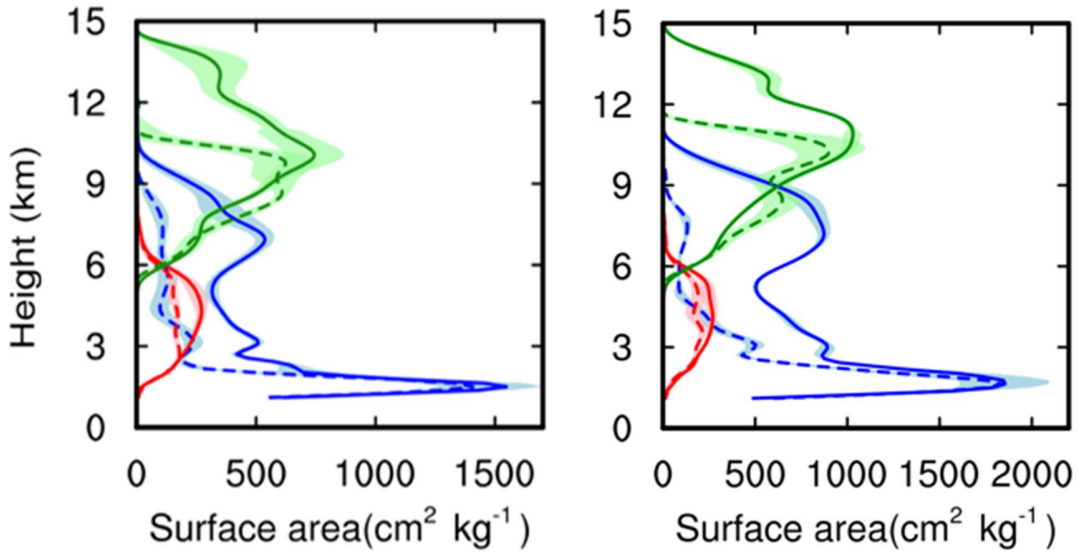

Figure 3.32 Vertical profiles of droplet surface area for cloud droplets (blue), rain drops (red), and ice-phase particles (green) and standard errors (shaded) for the warm-cloud period in C_PI (left dashed), C_BG (left solid), PL3_PI (right dashed) and P3_BG (right solid).

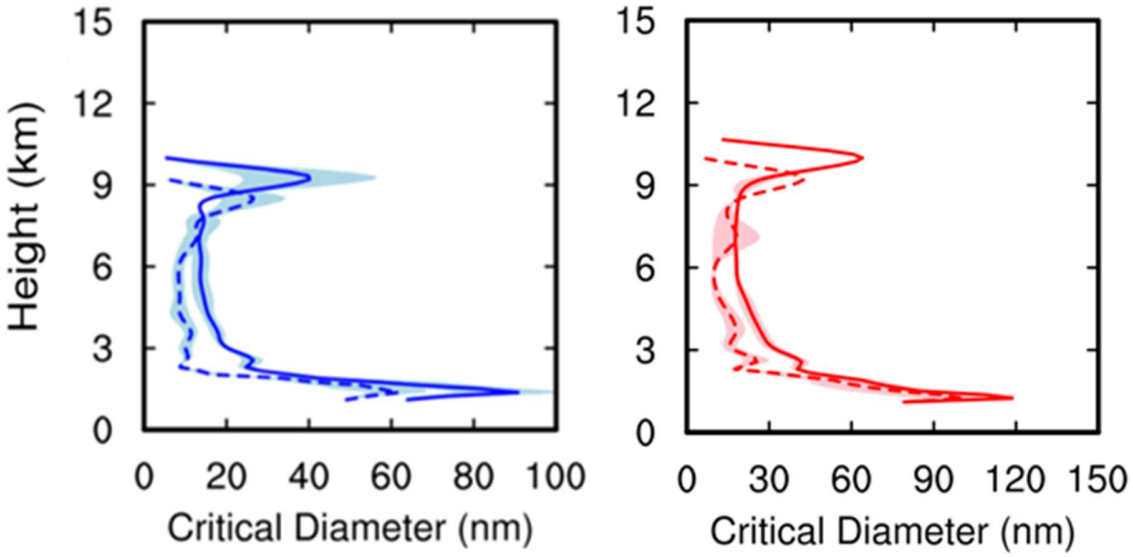

Figure 3.33 Vertical profiles of critical diameter for activation and standard errors (shaded) for the deep-cloud period in C_PI (blue dashed), C_BG (blue solid), PL3_PI (red dashed) and P3_BG (red solid).

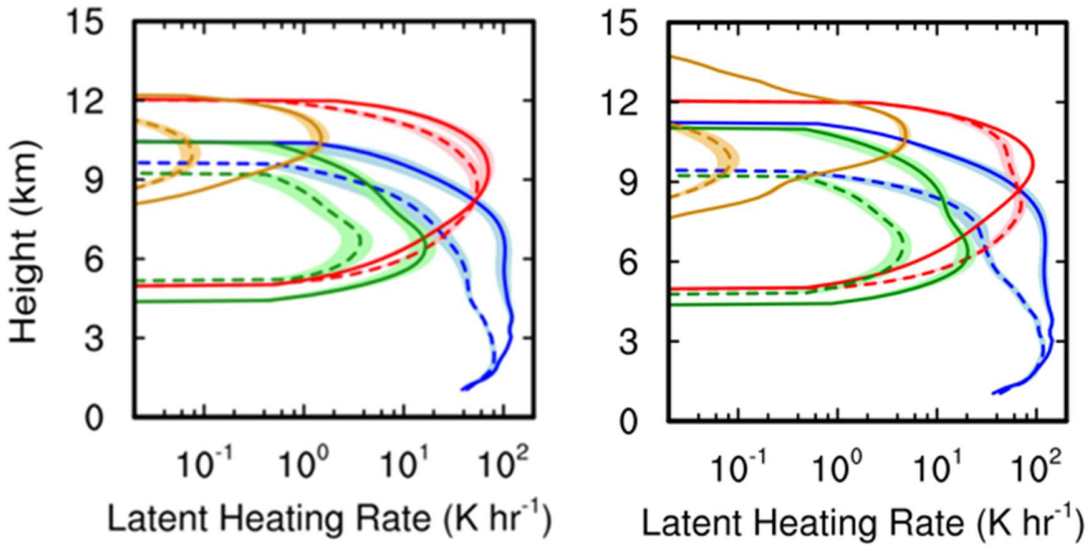

Figure 3.34 Vertical profiles of latent heating from condensation (blue), deposition (red), drop freezing (orange), and riming (green), and standard errors (shaded) for the deep-cloud period in C_PI (left dashed), C_BG (left solid), PL3_PI (right dashed) and P3_BG (right solid).

To understand the relative role of the enhanced condensational heating and latent heating from ice-related processes in intensifying convection, three sensitivity tests based on P3_BG are further conducted. In P3_BG_LH1, the net latent heat of condensation and evaporation in the warm phase (above 0 °C) was multiplied by a factor of 0.85. The factor means a 15% reduction from P3_BG. In P3_BG_LH2, the latent heat at upper levels from the deposition, freezing including riming, and sublimation was reduced by 15% from P3_BG. As shown in Figure 3.34, the condensational heating is the dominant heat source at low and middle levels, while it is the depositional heating at upper levels. to gain understanding of the relative role of the increased latent heat at low, middle, and upper levels in intensification of convection. As shown in Figure 3.34, the depositional heating is dominant and has large values at 8 to 11 km altitudes, so this test was to show the impact of increased latent heating at upper levels (excluding the reduction in riming or drop

freezing did not make much difference in the results). At middle levels, condensational heating is dominant compared with other processes (Figure 3.34). Therefore, in P3_BG_LH3, the net latent heat of condensation and evaporation is reduced by 15% at middle levels (-38 to 0 °C). Note, the cooling terms are reduced at the same time to maintain the balance of the microphysical processes. For example, reducing latent heating from condensation by 15%, implies an unaccounted for increase of evaporative cooling. Figure 3.35 clearly shows that with a 15% reduction of the net latent heating at low levels, the convective intensity over the entire vertical profile was reduced drastically (purple vs. red in Figure 3.39). In contrast, with the same reduction at upper levels (e.g., mainly 8 to 11 km), the updraft velocity was decreased only above 8 km (green), with a magnitude of 50% smaller than that found for the P3_BG_LH1 simulation. With the reduction at middle levels (orange line), the magnitude of the reduced updraft velocity is similar to that of reducing latent heat at upper levels, which is much smaller than the impact of reducing the low-level heating. The probability density function (PDF) of *w* in Figure 3.40 shows similar results. Given the increase of the net latent heating at low levels from C_PI to C_BG averaged over the entire convection period is 27%, doubled than that at upper levels (i.e., 14%), and the low levels were dominated by condensational latent heating, it is concluded that the increase of condensational heating played the predominant role in the substantial enhancement of convection by $UAP_{<50}$, whereas the enhanced latent heating at upper levels played a secondary role. The corresponding changes in precipitation are shown in Figure 3.41. These tests conclude that the enhanced condensation heating is the predominant player in the convection and precipitation intensification, whereas the enhanced latent heating at upper levels played a secondary role. This is different from the "cold-phase

invigoration" (i.e., enhanced ice-related processes), which is caused by added CCN that can be activated at the cloud base via suppressing coalescence and delaying warm rain. $UAP_{<50}$ do not suppress droplet coalescence and delay the rain because $UAP_{<50}$ can only be activated above the cloud base when rain has already formed, and supersaturation is enhanced by a reduced droplet surface area available for condensation.

Because of this greatly enhanced convection associated with $UAP_{<50}$, the mass mixing ratios of all hydrometeors are nearly doubled under the deep cloud period (Figure 3.35). The activation of $UAP_{<50}$ leads to an increase- up to an order of magnitude- in droplet number concentrations (Figure 3.36), as well as a drastic increase in ice-phase particle concentrations resulting from enhanced freezing including riming. All ice-phase particle number concentrations (ice, snow, and graupel) increase by ~two times generally, but the increase of the mass mixing ratio of ice-phase particles is largely driven by graupel with snow mass reduced (Figure 3.37), particularly in mixed-phase regions (6 -10 km) resulting from a larger amount of supercooled liquid droplets in the cases of $UAP_{<50}$. Falling graupel particles to the warm phase increase rain mass under the deep cloud period (Figure 3.35), contributing to increased surface precipitation as in Figure 3.31.

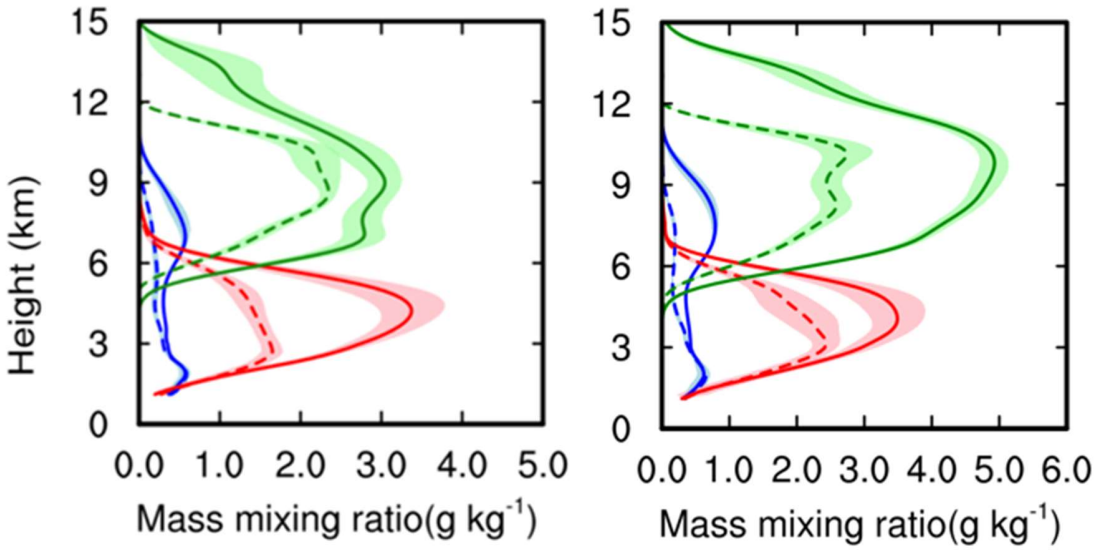

Figure 3.35 Vertical profiles of mass mixing ratios for cloud droplets (blue), rain drops (red), ice-phase particles (green)and standard errors (shaded) for the warm-cloud period in C_PI (left dashed), C_BG (left solid), PL3_PI (right dashed) and P3_BG (right solid).

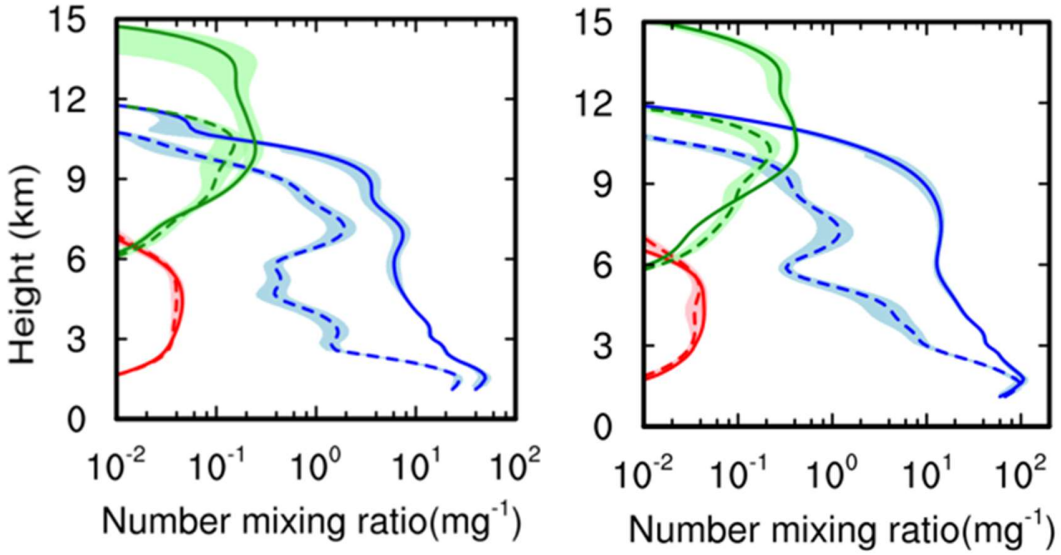

Figure 3.36 Vertical profiles of number mixing ratios for cloud droplets (blue), rain drops (red), ice-phase particles (green)and standard errors (shaded) for the warm-cloud period in C_PI (left dashed), C_BG (left solid), PL3_PI (right dashed) and P3_BG (right solid).

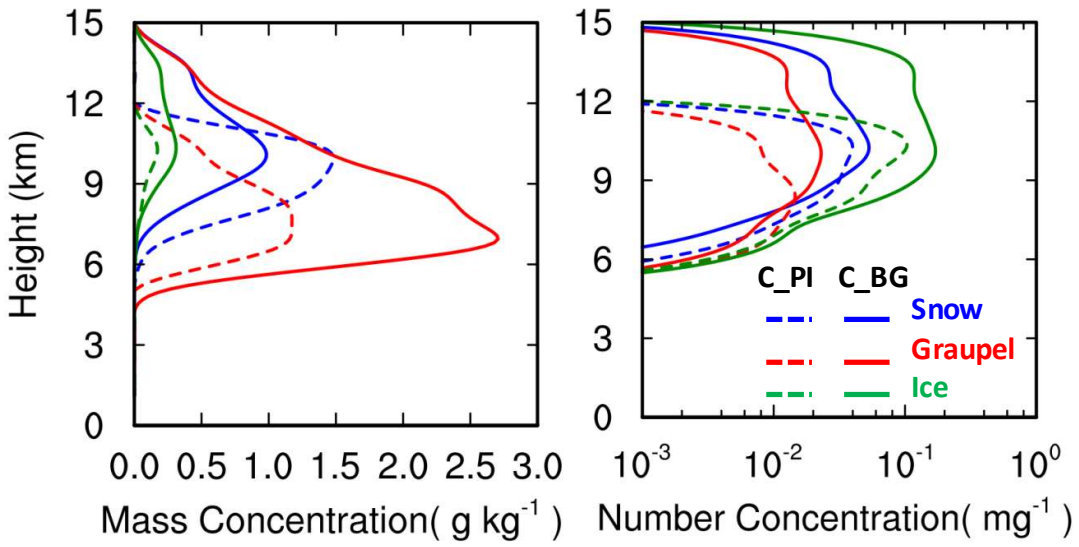

Figure 3.37 Vertical profiles of mass (left) and number (right) concentrations of ice (green), now (blue), and graupel (red) at the deep-cloud period for C_PI (dashed) and C_BG (solid).

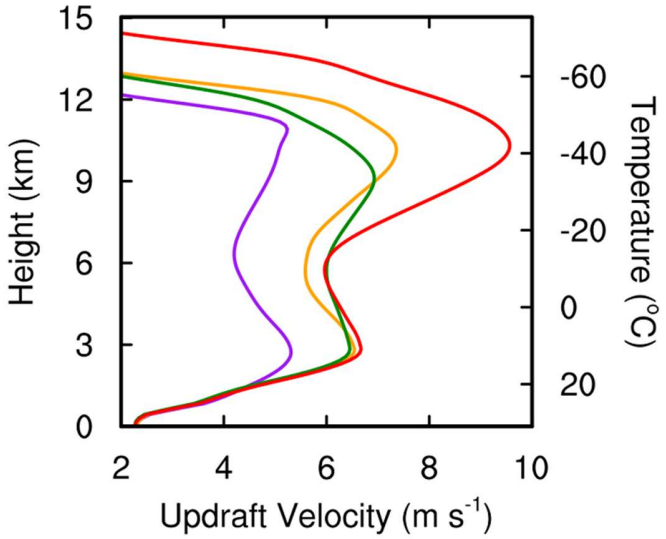

Figure 3.38 Vertical profiles of updraft velocity averaged over the top 10 percentiles (i.e., 90th-100th) for the updrafts with w>2 m s^{-1} during 1400-1900 UTC from the convective clouds around the T3 site for P3_BG (red), P3_BG_LH1 (purple), and P3_BG_LH2 (green), and P3_BG_LH3 (orange).

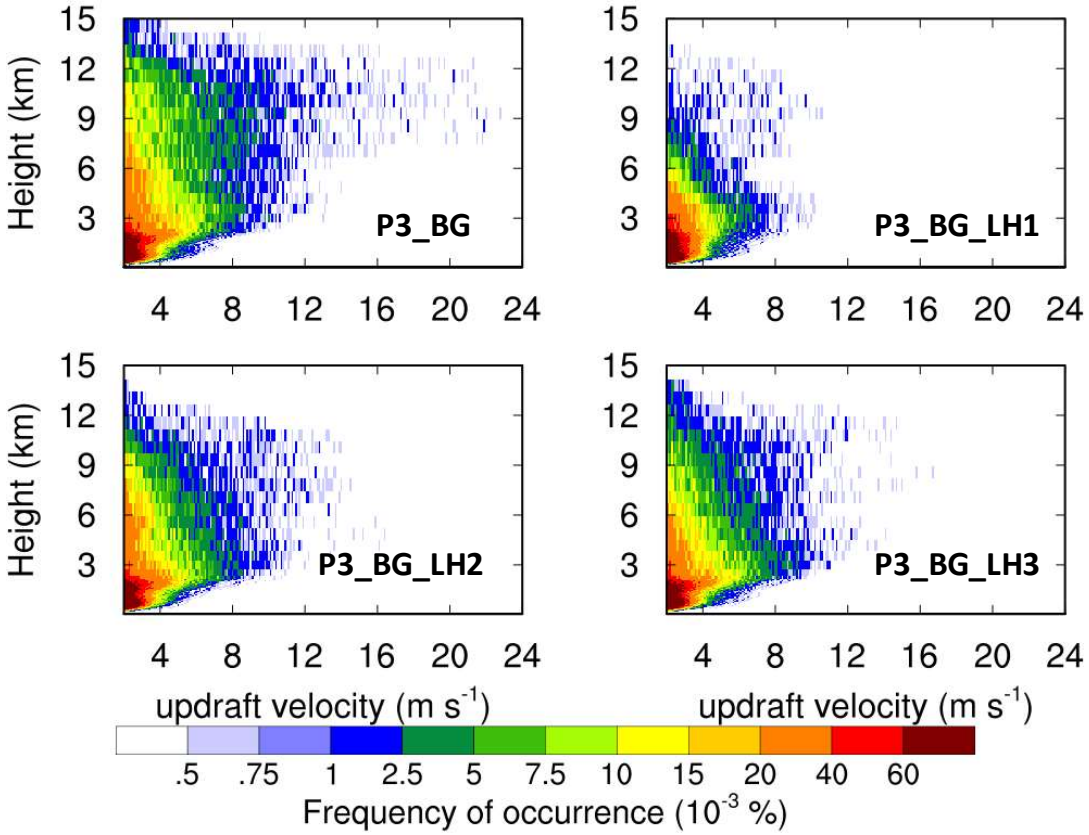

Figure 3.39 Vertical profile of PDF of updraft speeds for w>2 m s-1 from P3_BG, P3_BG_LH1, and P3_BG_LH2, and P3_BG_LH3 during 1400-1900 UTC from the convective clouds around the T3 site.

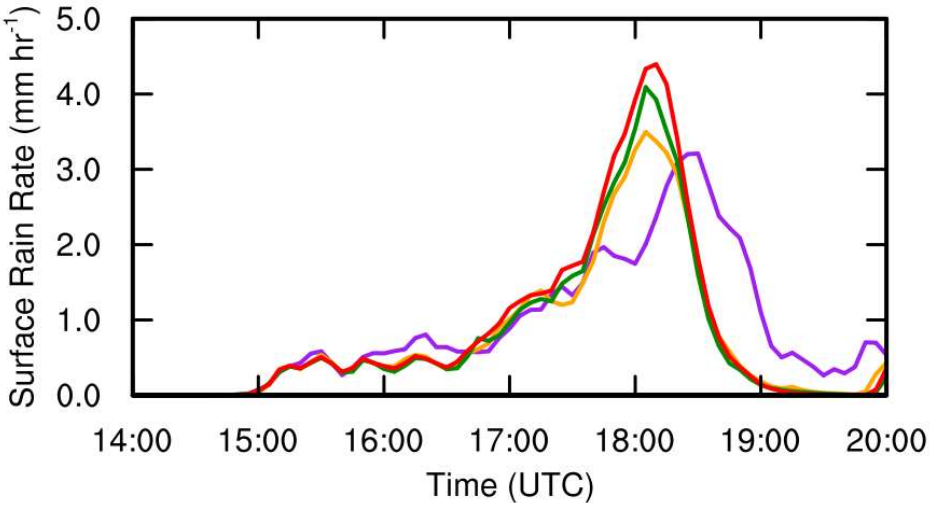

Figure 3.40 Time series of mean surface rain rate averaged over the red box area (Figure 3.16) from simulations of P3_BG (red), P3_BG_LH1 (purple), and P3_BG_LH2 (green), and P3_BG_LH3 (orange).

In summary, the detailed simulations show that the drastic enhancement in convective intensity is primarily attributable to the enhanced condensational heating, with the latent heat released from enhanced ice-related processes at upper levels playing a secondary role. This differs from the previous "cold-cloud invigoration" concept (Rosenfeld et al., 2008), which does not consider aerosol impacts on condensational heating. As illustrated in Figure 3.38, the enhanced condensational heating is driven by activating $UAP_{<50}$ above cloud base due to high S_w resulting from fast droplet coalescence and forming an additional number of cloud droplets. The subsequent condensational growth considerably lowers the water supersaturation, liberating additional latent heating in the lower atmosphere, which enhances convective intensity drastically. The additional condensate from this enhanced condensation add to both the warm rain and supercooled cloud water. Besides the enhanced droplet freezing and riming because of additional supercooled water, the intensified convection also enhances ice deposition. Cumulatively, these stronger ice processes at middle and upper levels further enhance convection but with much less significance relative to enhanced condensation at low-levels. The effects of $UAP_{<50}$ are found to be in contrast with those of $CCN_{>50}$. $UAP_{<50}$ increase warm rain rate and have no effect on the timing of peak rain rate, whereas $CCN_{>50}$ suppress warm rain rate and delay the timing of peak rain rate.

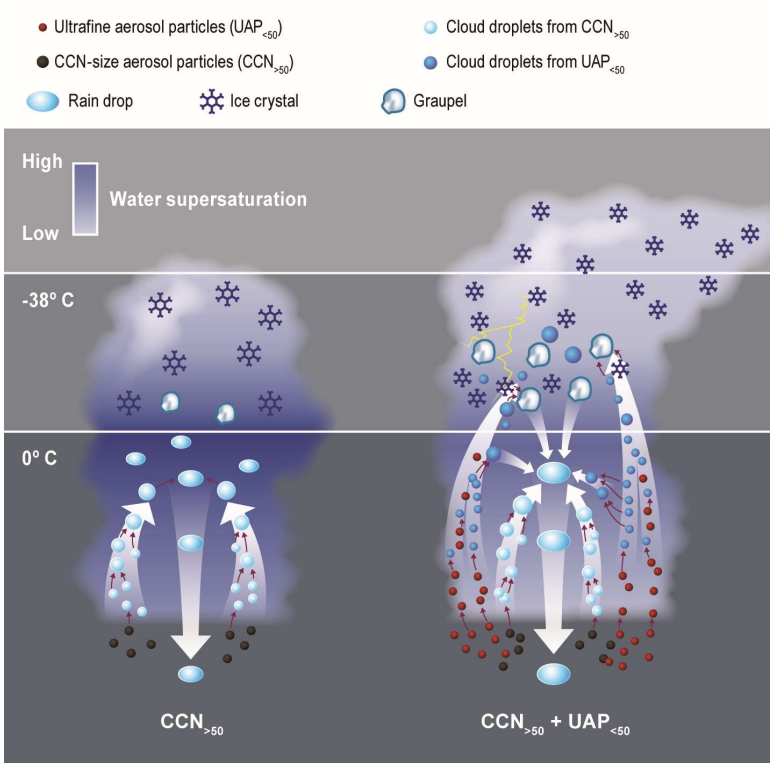

Figure 3.41 Illustration of the effect of ultrafine aerosol particles smaller than 50 nm ($UAP_{<50}$) on tropical convective clouds.

3.5 Conclusions and Discussion

The retrieved updraft velocity from RWP has allowed us to directly examine and help constrain aerosol impacts on updraft intensity, revealing the potentially substantial convective updraft and precipitation enhancements by $UAP_{<50}$ from the Manaus pollution plume. Real-case 3-D simulations are used to reproduce (1) observed convective cloud characteristics and (2) observed convective updraft and precipitation enhancements by $UAP_{<50}$ over the Amazon region. The physical mechanism for such strong intensification of convection stems from the strong capacity of these DCCs in activating $UAP_{<50}$ that usually have a much higher number concentration than $CCN_{>50}$ particles, because fast droplet coalescence in pristine conditions removes integrated droplet surface area for

condensational growth, leaving a highly supersaturated condition. The subsequent condensational growth of an additional number of droplets considerably lowers the water supersaturation, liberating a large amount of additional latent heat at the low and middle levels of DCCs and considerably enhancing updraft strength. This "warm-phase invigoration" has much stronger effects than the "cold-phase invigoration" previously proposed (Rosenfeld et al., 2008). Note, the $UAP_{<50}$ increases the rain water amount mainly through enhanced accretion of the added cloud droplets and the added graupel melting. Added $UAP_{<50}$ does not affect the timing of precipitation because $UAP_{<50}$ can be activated to form additional cloud droplets only after warm rain is in progress. In contrast, $CCN_{>50}$ particles suppress and delay warm rain, and then delay the peak precipitation.

The large magnitude of the condensation effects is likely because of the very warm, moist and clean condition in the Amazon wet season. This leads to a mechanism different from that associated with dry season events over the Amazon (i.e., "cold-phase invigoration," Rosenfeld et al., 2008; Andreae, 2007; Koren et al., 2008; Lin et al., 2006), or other dryer or colder locations (e.g., Li et al. 2011; Zhang et al. 2007). A key factor is the ample cloud droplet coalescence in the tropical rainforest environment that is not impacted by human activities, which rapidly removes droplets. Droplet removal leads to suppressed condensation, leaving a high supersaturation for activating $UAP_{<50}$. This is corroborated by sensitivity tests with droplet collision-coalescence processes shut off for both background (C_BG) and plume-affected (P3_BG) cases, which show small differences in water supersaturation between the two cases, in contrast to the large differences when droplet collision-coalescence processes turned on.

It has been believed that there is a cut-off size for aerosol particles to serve as CCN for a specific region or typical aerosol type (Andreae, 2007), typically larger than 60 nm (Lohmann and Feichter, 2005). Generally, $UAP_{<50}$ are not considered to contribute to CCN due to their small sizes, which require high supersaturation. The study shows that under both present-day Manaus regional background and PI environments over the Amazon region, $UAP_{<50}$ can effectively serve as CCN for droplet nucleation above cloud base after coalescence starts. DCCs in the natural rainforest environment over the Amazon where fine particles are scarce may be especially susceptible to the addition of $UAP_{<50}$, as shown by this work. The dearth of new particle formation in Amazon boundary layer under natural conditions might be because (1) low sulfuric acid concentration and (2) products of gas phase oxidation of isoprene do not facilitate new particle formation as efficiently as those from oxidation of other biogenic volatile organic compounds (e.g., monoterpenes). However, anthropogenic emissions in this region may induce aerosol nucleation and produce a large amount of $UAP_{<50}$ through various mechanisms (Zhang et al. 2012; Shrivastava et al. 2017), e.g., interactions of anthropogenic sulfur and NO_x with biogenic sources such as organic acids from aromatics enhance aerosol nucleation.

A recent study showed that aerosol concentrations over the Amazon peak at the upper troposphere (Andreae et al., 2018), unlike the VD assumed in our model simulations. We conducted sensitivity tests (C_BG_VD and C_PI_VD) by using a VD similar to that in figure 7B of Andreae et al. 2018. Similar convective invigoration by increasing $UAP_{<50}$ through the same mechanism is seen (Figure 3.42). The new VD does not affect the conclusion because the maximum supersaturation peaks at an altitude of 6 km and the latent heating at low levels is the major contributor to convection intensification, so the

addition of $UAP_{<50}$ at upper levels would not greatly affect the convective invigoration below it. However, the new VD causes stronger convective invigoration at upper levels because of higher aerosol concentrations. Another uncertainty results from the aerosol SD assumed in the simulation. We also carried out sensitivity tests (P3_BG_SD, C_BG_SD, and C_PI_SD) by using a SD measured at ~20 km downwind from Manaus (Line 2 in Figure 3.14A). The results were similar to the previous simulations with a different SD (Figure 3.43). Thus, we infer that any aerosol scenario that contains a large ratio of $UAP_{<50}$ to $CCN_{>50}$ in a humid environment would produce the $UAP_{<50}$ effects we report in this study.

Because all $UAP_{<50}$ are removed in our simulations for examining the $UAP_{<50}$ effects, and because small numbers of $UAP_{<50}$ are observed at the remote rainforest site in the central Amazon Basin (e.g., Figure 6a of Pöhlker et al., 2018), we conducted an additional sensitivity test, C_PI2, in which $UAP_{<50}$ (60 cm^{-3}) were added to C_PI (Table 3.2). We found that the differences in updraft velocity and supersaturation between C_PI and C_PI2 are very small (Figure 3.44). Thus, our conclusion and the proposed mechanism are not affected by the small amount of $UAP_{<50}$ in the PI condition. This indicates that we should expect similarly large $UAP_{<50}$ effects for pristine regions with low $UAP_{<50}$ concentration. The intrusion of urban areas such as the Manaus metropolis produces a large amount of $UAP_{<50}$, which may drastically change convective and precipitation conditions over the Amazon Basin by producing stronger convective clouds and precipitation. We also conducted the sensitivity tests C_PI_ATTO and C_BG_ATTO (Table 1) for testing the addition of $UAP_{<50}$ condition to the present-day pristine $CCN_{>50}$ condition. We see the similar $UAP_{<50}$ effects on updraft velocity and supersaturation as shown in Figure 3.45.

Therefore, an addition of a descent number of ultrafine particles to the present-day pristine conditions would also drastically invigorate DCCs

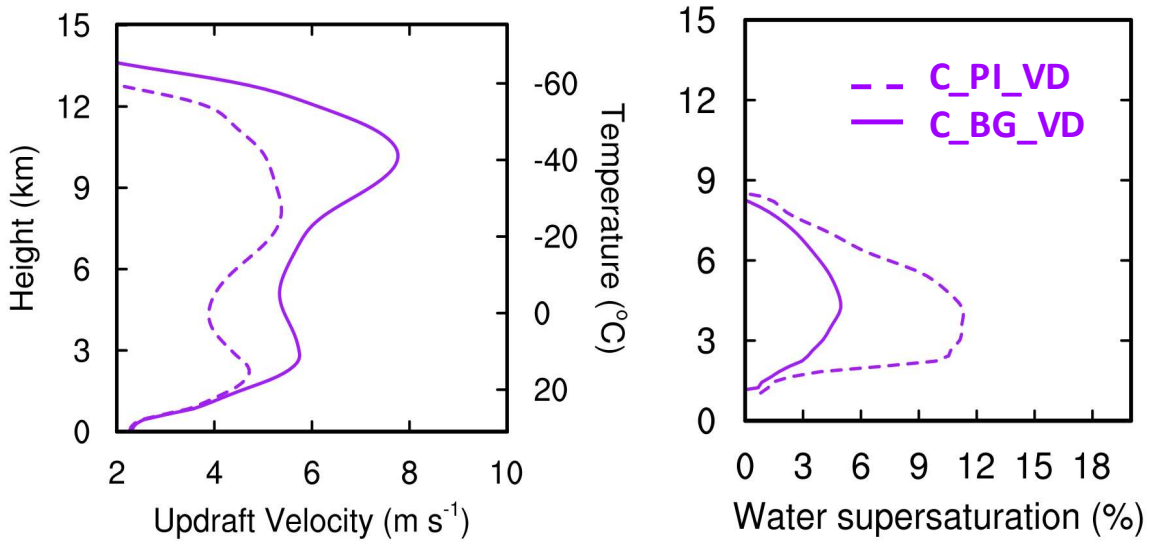

Figure 3.42 Vertical profiles of updraft velocity (left) and vapor supersaturation (right) for the sensitivity tests of aerosol vertical distribution C_PI_VD (dashed) and C_BG_VD (solid). Updraft velocity was processed in the same way as Figure 3.19A, and vapor supersaturation and droplet nucleation rate were processed in the same way as Fig. 3.31.

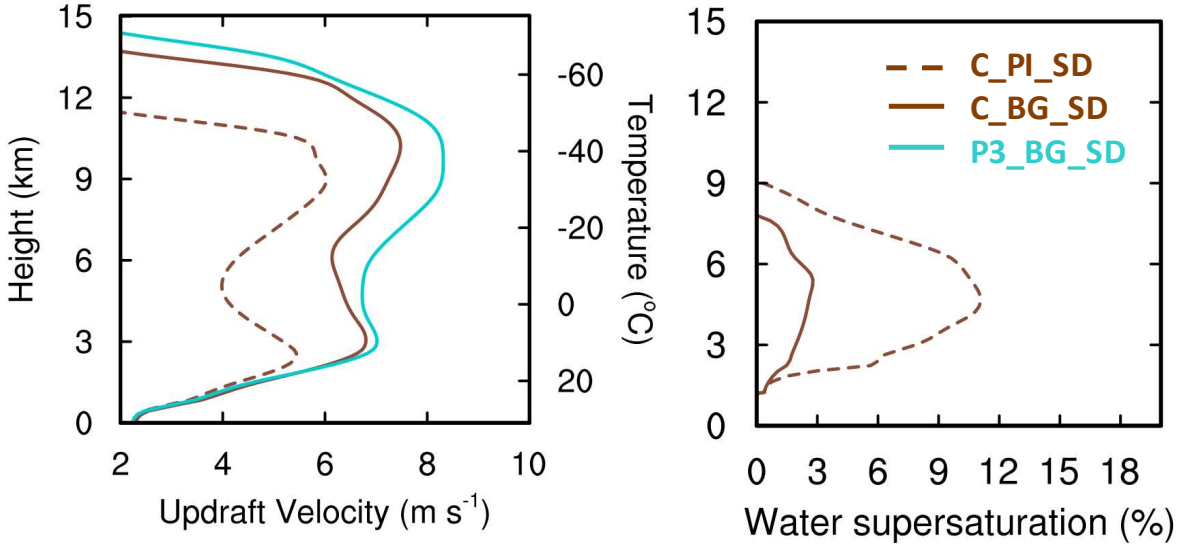

Figure 3.43 Vertical profiles of updraft velocity (left) and vapor supersaturation (right) for the sensitivity tests of aerosol size distribution C_PI_SD (brown dashed), C_BG_VD (brown solid) and P3_BG_SD (cyan solid). Updraft velocity was processed in the same way as Figure 3.19A, and vapor supersaturation and droplet nucleation rate were processed in the same way as Fig. 3.31.

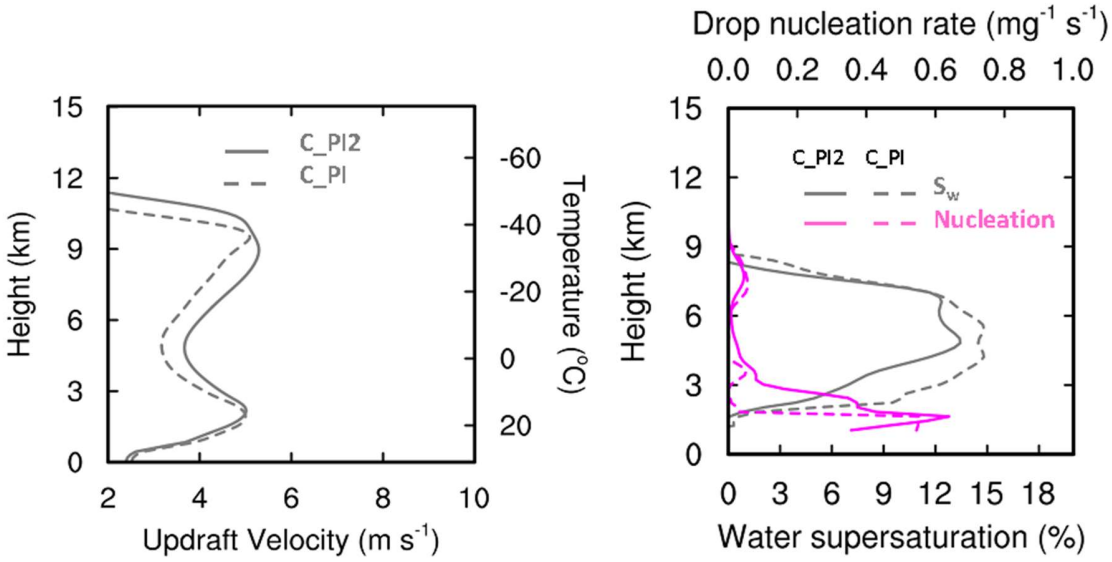

Figure 3.44 Comparison of vertical profiles of updraft velocity (left), and the corresponding vapor supersaturation (right grey) and droplet nucleation rate (right pink) between C_PI (dashed) and C_PI2 (solid). Updraft velocity was processed in the same way as Figure 3.19A, and vapor supersaturation and droplet nucleation rate were processed in the same way as Fig. 3.31.

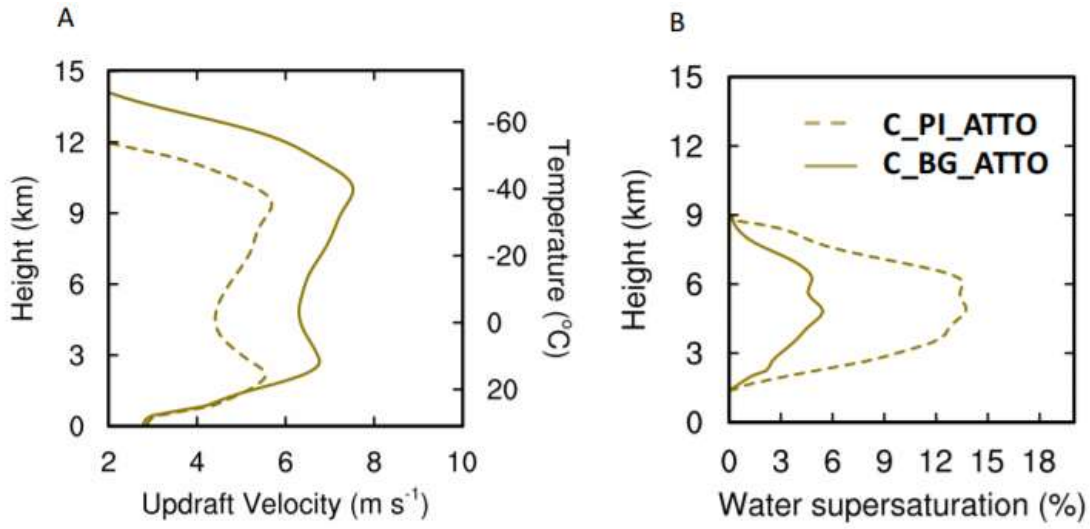

Figure 3.45 (A) updraft velocity and (B) vapor supersaturation for the sensitivity tests of C_PI_ATTO and C_BG_ATTO. Updraft velocity was processed in the same way as Figure 3.19A, and vapor supersaturation and droplet nucleation rate were processed in the same way as Fig. 3.31.

All of our tests with different aerosol properties (SD and VD) indicate that observed and simulated $UAP_{<50}$ effects and the proposed mechanism are robust. Given the importance of the Amazon Basin in global circulation and hydrology, the ultrafine pollution particles introduced by human activities could have profound effects on other places around the globe. A lack of aerosol nucleation (or a low concentration of ultrafine particles) and the existence of ample moisture may not be unique to the Amazon Basin and may also occur in other tropical forests and oceans, further highlighting the global importance of our results. For example, a recent study found a conspicuous enhancement of lightning over shipping lanes in the equatorial Indian Ocean (Thornton et al., 2017). We conclude that $UAP_{<50}$ can modulate convection and rain-forming processes more strongly than previously considered, especially in pristine regions. Therefore, the changes of

ultrafine pollution particles from preindustrial conditions to the present may possibly have appreciably changed deep convective clouds.

Chapter 4. Impacts of Cloud Microphysics Parameterizations on Simulated Aerosol-DCC interactions

4.1 Introduction

In spite of substantial efforts made to identify the governing factors and mechanisms in ACI in recent studies (Yin et al., 2005; van den Heever et al., 2006, 2011; Rosenfeld et al., 2008; Lee et al., 2009; Fan et al., 2013), aerosol impacts on the evolution of various types of clouds and precipitation remain poorly known.

Bulk and bin schemes are both widely used to represent cloud microphysical processes for simulating ACI. Hydrometeor size distributions in bulk schemes are diagnosed from the predicted bulk mass (one-moment) or number and mass (two-moment) mixing ratios of various hydrometeor types and assumed size distribution shapes (e.g., gamma function). The size distributions of hydrometeors in bin scheme are discretized by a number of size bins and predicted, which may physically represent some aerosol-cloud interaction processes (Khain et al., 2000). In general, bin approaches can provide a more rigorous numerical solution and a more robust cloud microphysics representation. Some studies have discovered that two-moment microphysical schemes, which are widely used in regional and global models, have some limitations in representing certain important microphysical processes such as aerosol activation, condensation/deposition, sedimentation, and rain evaporation (Li et al., 2009; Khain et al., 2009; Ekman et al., 2011; Wang et al., 2013; Milbrandt and Yau, 2005; Morrison, 2012; Lee et al. 2018b). However, bin cloud microphysics is often applied with a prescribed aerosol spectrum assuming a fixed composition and a simple aerosol budget treatment without coupling with chemistry/aerosol calculations due to the expensive computation cost. As a result, many

aerosol lifecycle processes such as aerosol nucleation, growth, aqueous chemistry, aerosol resuspension, and below-cloud wet removal are missing or highly parameterized. In addition, aerosol chemical composition and size distribution vary significantly spatially and temporally (Qian and Giorgi, 2000). The simple representations of aerosol lifecycle processes in cloud models limit the feedback mechanisms, the spatial heterogeneity of aerosols, and the duration of simulations (Gao et al., 2016). Therefore, representing detailed aerosol processes is necessary to realistically simulate aerosol-cloud interactions.

Currently, the online released Chemistry version of Weather Research and Forecast (WRF) model (WRF-Chem) (Grell et al., 2005; Skamarock et al., 2008) only couple chemistry and aerosol modules with bulk microphysics for aerosol-cloud interactions. A spectral-bin microphysics (SBM) has been coupled into WRF-Chem with the Model for Simulating Aerosol Interactions and Chemistry (MOSAIC) (Fast et al., 2007) by Gao et al. 2016 to provide realistic simulations of both cloud and aerosol lifecycle processes. The newly coupled system is initially evaluated for warm marine stratocumulus clouds (Gao et al., 2016).

Aerosol-Cloud-Precipitation-Climate (ACPC) working group is a joint initiative of the International Geosphere–Biosphere Programme (IGBP) and the World Climate Research Programme (WCRP), developed through the cooperation of the IGBP's Integrated Land Ecosystem–Atmosphere Processes Study (iLEAPS) and International Global Atmospheric Chemistry (IGAC) and WCRP's Global Energy and Water Cycle Experiment (GEWEX). It aims at a better scientific understanding of these interactions at a fundamental level. The goal is to identify, disentangle, and quantify signals of impacts of aerosol perturbations on clouds, precipitation, and radiation,

taking into account adjustments and feedback processes by synergistically exploiting observations and models across scales. Two cloud regimes have been defined and pursued, one targeting shallow clouds(marine stratocumulus clouds in the VOCALS region and period) and one targeting deep convective clouds(in the Houston, USA, region for a case in June 2013 where observations are available). In this Chapter, we employ WRF-Chem coupled with SBM to simulate the deep convective cloud case over Houston area selected by ACPC and explore the impacts of cloud microphysics parameterization on simulated Aerosol-DCC interactions.

4.2 Model experiments

A local convective event near Houston, Texas on 19-20 June 2013 is selected for the modeling case study owing to the most favorable conditions for simulating primarily isolated cells. Model simulations are conducted using WRF-Chem v3.6.1. Two nested domains with horizontal grids of 2 and 0.5 km are used (Figure 4.1) with 51 vertical levels up to 50 hPa. The Domain 1 simulation is designed for providing a relative realistic aerosol forcing for domain 2. The meteorological and chemical lateral boundary and initial conditions were created from MERRA-2 (Gelaro et al., 2017). The anthropogenic emission was from NEI-2011 emissions. The biogenic emission came from the Model of Emissions of Gases and Aerosols from Nature (MEGAN) product (Guenther et al., 2006). The biomass burning emission was from the Fire Inventory from NCAR (FINN) model (Wiedinmyer et al., 2011). We used the CBMZ gas-phase chemistry (Zaveri and Peters, 1999) and MOSAIC aerosol model with four bins (Zaveri et al., 2008). The physics schemes applied in the simulation are the Unified Noah land surface scheme (Chen and Dudhia, 2001), Mellor-Yamada-Janjic planetary boundary layer scheme (Janjic et al.,

1994), Multi-layer, Building Environment Parameterization (BEP) urban physics scheme (Salamanca and Martilli, 2010), the RRTMG longwave and shortwave radiation schemes (Iacono et al., 2008), and Morrison two-moment microphysics scheme (Morrison et al., 2005). Domain 2 is driven by the same initial and lateral boundary meteorological conditions from MERRA-2 and chemistry conditions from Domain 1 outputs with the lateral boundary conditions updated every 6 h using the "ndown" approach. Domain 2 use the same physics schemes except for applying the SBM cloud microphysics scheme. The modeled dynamic time step was 6 s for 2-km resolution and 3 s for 0.5-km resolution. The simulations in domain 1 were initiated at 0000 UTC on 14 Jun and the meteorological field was reinitialized every 36 hours. The simulations in domain 2 were initiated at 0000 UTC on 19 Jun and ran for 30 hours.

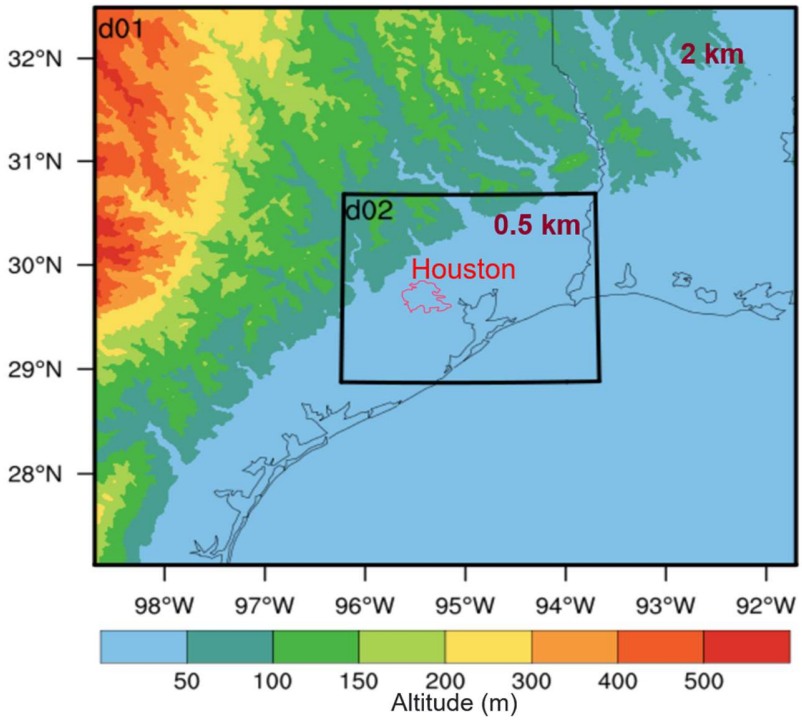

Figure 4.1 The simulation Domain 1 (d01) and Domain 2 (d02) with background of surface height (m). Houston city is denoted by pink contour.

We conducted the simulation in domain 1 to generate two aerosol backgrounds (polluted and clean) for domain 2 by turning on/off the anthropogenic aerosol emission. Six experiments (Table 4.1) are carried out for simulating the convective event near the Houston in domain 2. SBM (LandAero) is the baseline run using SBM cloud microphysics schemes with both urban land and anthropogenic aerosols. It is driven by the polluted aerosol background simulated from domain 1. SBM_NA(No_Aero) is based on the baseline simulation but the anthropogenic aerosols are removed. It was driven by the clean aerosol backgrounds simulated from domain and conducted without anthropogenic emission. MORR and MORR_NA are based on SBM and SBM_NA, except for using Morrison two-moment microphysics schemes. No_Land is the simulation based on LandAero but replacing the land use and vegetation type for urban with the surrounding type. No_LandAero is the simulation based on LandAero but the anthropogenic aerosols are removed and the land use and vegetation type for urban are replaced with the surrounding type. In this Chapter, the impacts of cloud microphysics parameterization on simulated Aerosol-DCC interactions are discussed based on four simulations: SBM, SBM_NA, MORR and MORR_NA. The simulations (LandAero, No_Land, No_Aero, No_LandAero) will be used for investigating the urbanization impact on convective clouds and precipitation in the next Chapter.

Table 4.1 Description of the Experimental Design

Name	Urban Land	Anthropogenic Aerosol	Microphysics
LandAero (SBM)	Y	Y	SBM
No_Aero (SBM_NA)	Y	N	SBM
No_Land	N	Y	SBM
No_LandAero	N	N	SBM
MORR	Y	Y	Morrison
MORR_NA	Y	N	Morrison

4.3 Model Evaluation on Aerosol and Cloud Properties

We first evaluate the aerosol and cloud properties from the domain 1 simulation to ensure a realistic aerosol forcing for domain 2. There are eight PM monitoring sites near Houston, which are ideal for the model evaluation by comparing with the observations. The site descriptions are summarized in Table 4.2.

Table 4.2 Descriptions of the PM2.5 Monitoring Sites near Houston

Abbreviation	Site Descriptions	Latitude	Longitude
HA	Houston Aldine	29.901	-95.326
HDP	Houston Deer Park 2	29.670	-95.129
SFP	Seabrook Friendship Park	29.583	-95.016
CR	Conroe Relocated	30.350	-95.425
KW	Kingwood	30.058	-95.190
CT	Clinton	29.734	-95.258
PP	Park Place	29.686	-95.294
GS	Galveston 99th Street	29.254	-94.861

The hourly variations of ground-level PM2.5 mass concentrations from both observation and simulation for these sites over 1 day before the convection initiation is depicted in Figure 4.2. Generally, the model simulation of hourly PM2.5concentrations is

reasonable compared with the observations. The model reproduces the diurnal variations, especially the increasing trend from 1200 UTC to 1800 UTC 19 Jun which is the period before the convection and the aerosol forcing for domain 2. Table 4.3 summarizes the simulated and measured surface PM2.5 averaged over 24 hours in Figure 4.2. It also shows good agreements between the simulation and measurements.

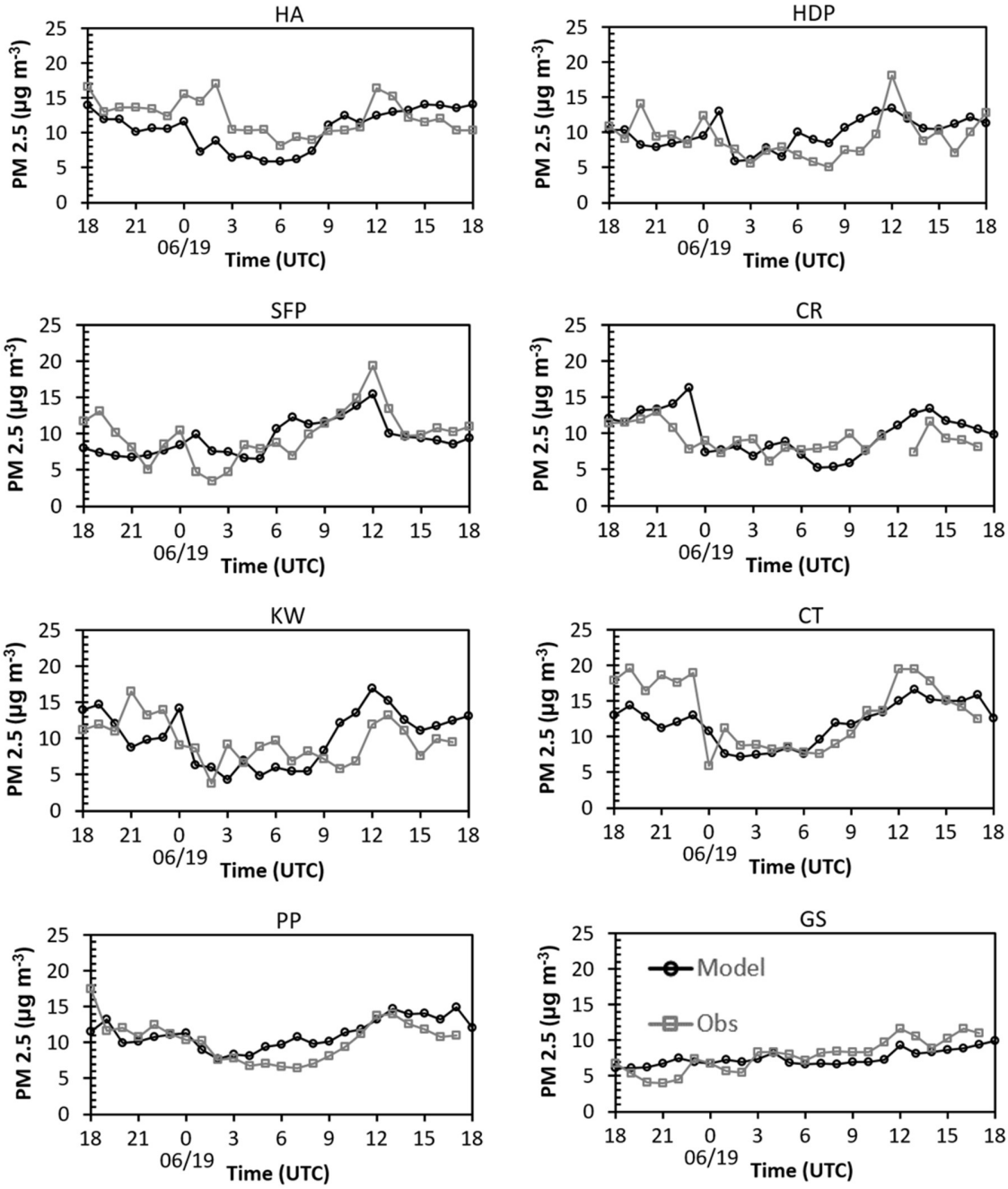

Figure 4.2 Site-by-site comparisons of the simulated and measured hourly PM2.5 mass concentrations over 24 hours (1 day before the convection initiation).

Table 4.3 Site-by-site comparisons of 24-hr averaged PM2.5 mass concentrations

Site	Obs	Model
HA	12.3	10.6
HDP	9.3	10.5
SFP	9.8	9.4
CR	9.1	10.0
KW	9.7	10.2
CT	13.4	11.9
PP	10.4	11.2
GS	8.0	7.5

The VIIRS satellite retrieved cloud base heights and CCN at the cloud base are further used for evaluation (Figure 4.3-4.4). Over the Houston area, the simulated cloud base heights are about 1-2 km, in agreement with the retrieved values, 1.2-1.8 km. The simulated CCN values over the rural areas east to Houston are about 400-600 cm^{-3}, consistent with the satellite retrievals. Note that some high CCN values (1000-1400 cm^{-3}) from the satellite north of Houston are also captured in the simulation.

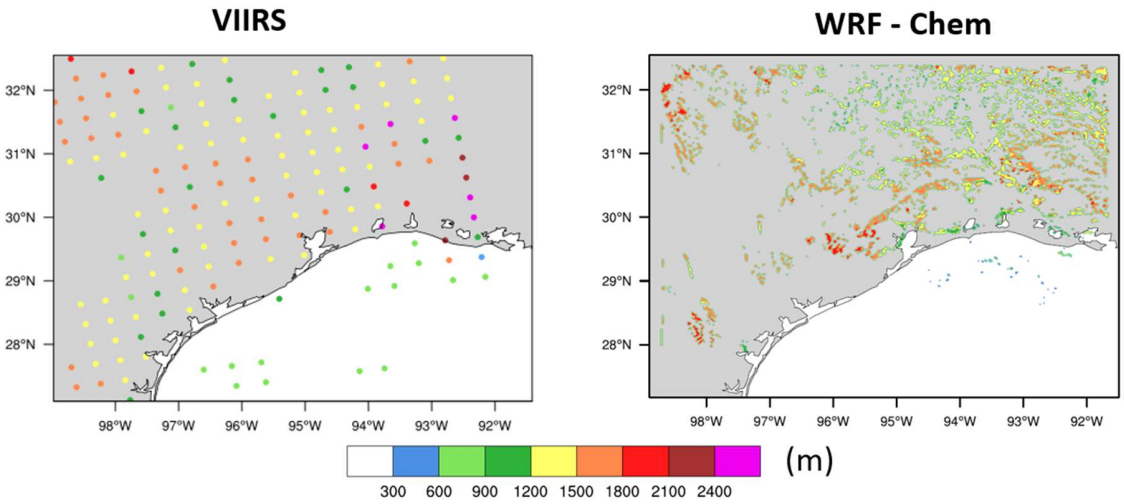

Figure 4.3 Evaluation of cloud base heights (m) from VIIRS satellite retrieved at 1943 UTC (Rosenfeld et al. 2016) and d01 model simulated at 2000 UTC, 19 Jun 2013

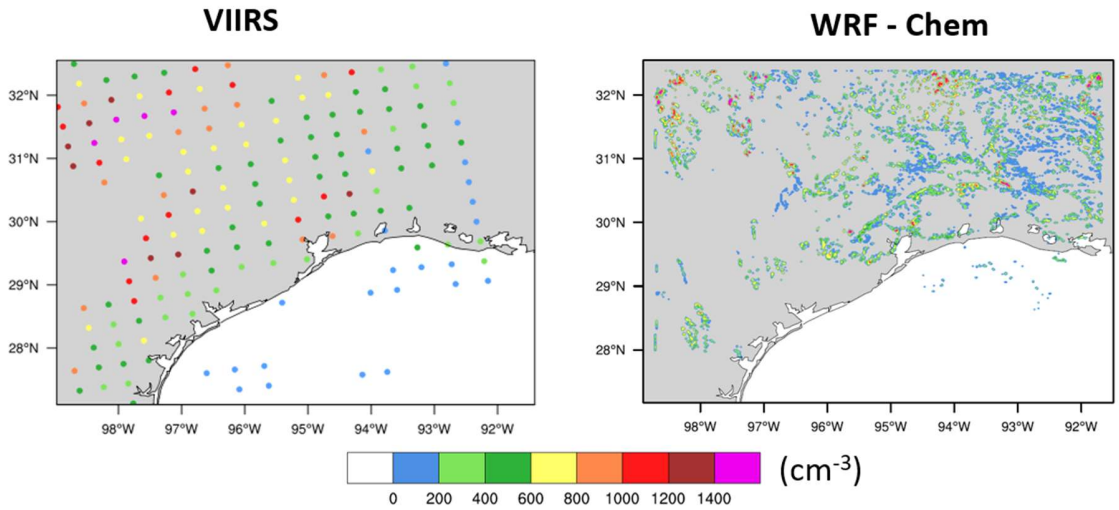

Figure 4.4 Evaluation of CCN number concentration at cloud base (cm^{-3}) from VIIRS satellite retrieved at 1943 UTC (Rosenfeld et al. 2016) and d01 model simulated at 2000 UTC, 19 Jun 2013.

We use the polluted and clean aerosol backgrounds simulated in domain 1 turning on/off the anthropogenic aerosol emission to drive the sensitivity experiments in domain 2 (Figure 4.5). The polluted and clean aerosol backgrounds (Figure 4.5) denote the scenarios with and without the anthropogenic aerosol perturbation. Three aerosol scenarios over the

Houston area (red boxes in Figure 4.5) are obtained. One is the urban area much polluted by anthropogenic aerosols, another is the rural area less polluted by anthropogenic aerosols and the other is the ocean area least polluted by anthropogenic aerosols. The overall size distributions are shown in Figure 4.6. The aerosol loading over the urban area is about 3 times that over rural area and 6 times that over ocean. It is notable that the increase of aerosol number over urban area is mainly contributed by ultrafine aerosols produced from anthropogenic activities.

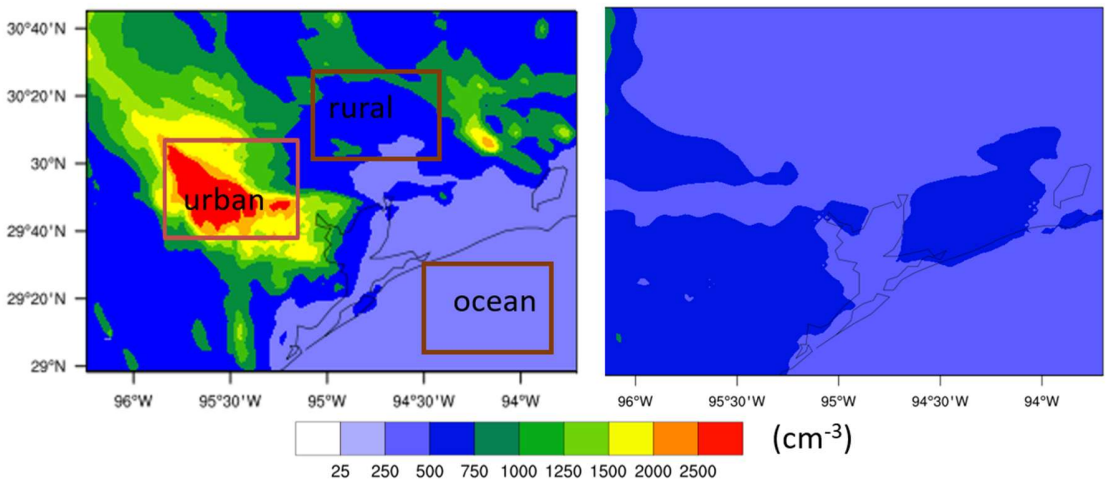

Figure 4.5 Aerosol number concentration of domain 2 with anthropogenic emission (left) and without anthropogenic emission (right) at 1200 UTC, 19 Jun 2016 (6-hr before the convection initiation).

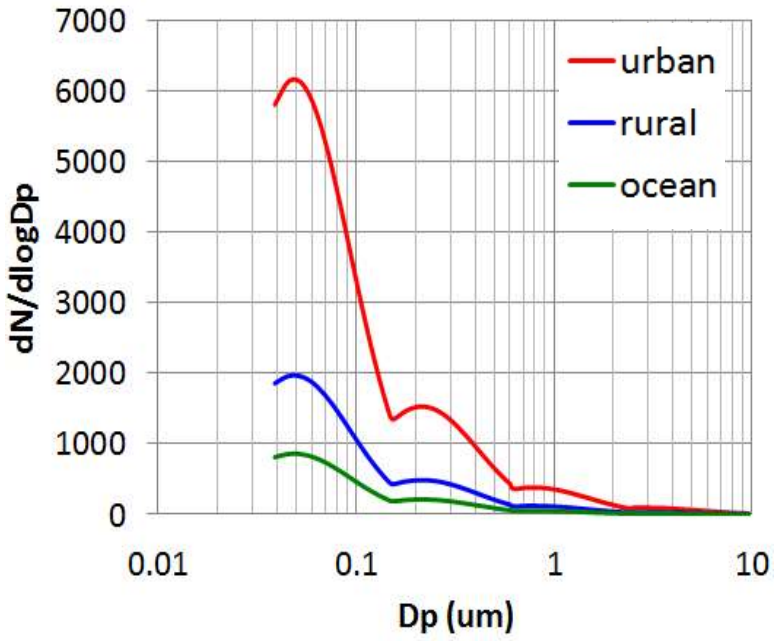

Figure 4.6 Aerosol size distributions for three aerosol scenarios (urban, rural and ocean). The boxes in Figure 4.5(left) are the respective analysis regions.

4.4 Comparison between SBM and Morrison in WRF-Chem

Figure 4.7 shows the evaluation of surface pressure and 10-m winds. Both SBM and MORR can capture the surface pressure pattern and 10-m winds near Houston before convection initiation. However, SBM gets a convection cell near Houston with both location and high reflectivity value in better agreement with observations from NEXRAD (Figure 4.8). Note that both SBM and MORR overestimate the frequency for reflectivity larger than 30 dBZ, but SBM is somewhat better (Figure 4.8). MORR predicts many scattered but weaker reflectivities near the Houston (Figure 4.8). The simulated composite reflectivities (i.e., the column maximum) are up to 55dBZ, which are consistent with NEXRAD. Compared with MORR, SBM get better vertical structures for high reflectivity range (i.e., 45-55dBZ) and agree with NEXRAD (Figure 4.9).

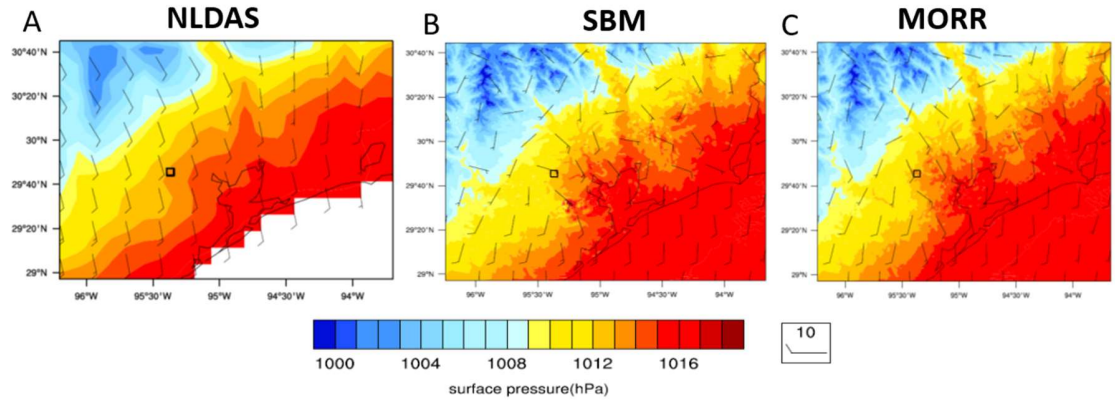

Figure 4.7 Surface pressure (shaded) and 10-m winds (vectors) from NLDAS, SBM and MORR at 2000 UTC, 19 Jun 2013.

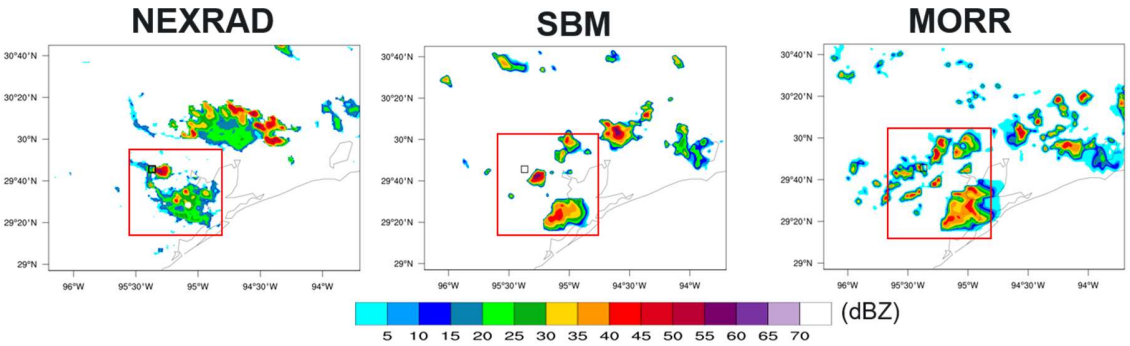

Figure 4.8 Composite reflectivity from NEXRAD, SBM and MORR at 2200 UTC 19 Jun 2013 when maximum reflectivity in Houston is observed. The red boxes are the analysis domains for convection cells near Houston.

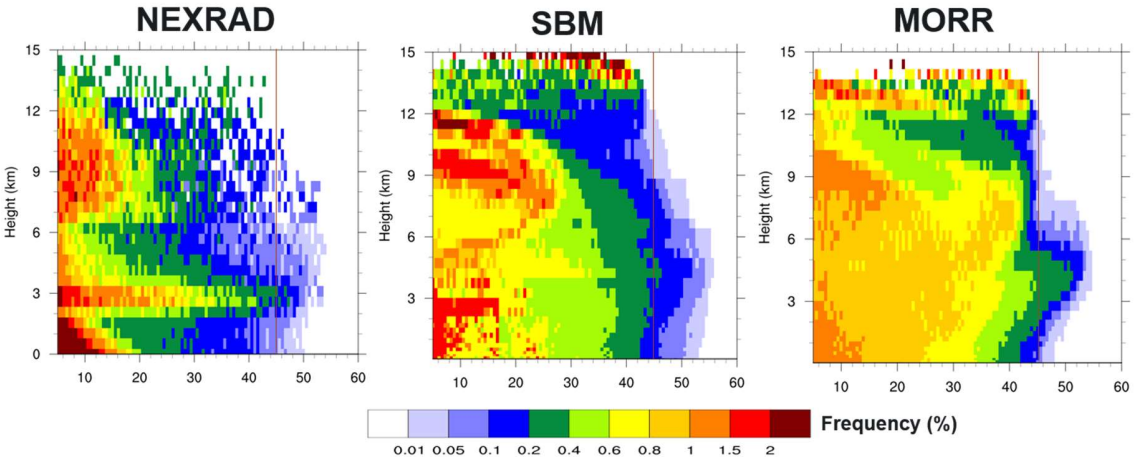

Figure 4.9 The PDFs of reflectivity (>0 dBZ) from NEXRAD, SBM and MORR for convection near Houston (red box in Figure 4.8) from 1800 UTC 19 Jun to 0000 UTC 20 Jun 2013. The red solid lines denote the reflectivity with the value of 45dBZ.

The precipitation results are shown in Figure 4.10 and 4.11. Both MORR and SBM gets the rain rate peak period from 2100UCT to 2300UTC consistent with the observation. SBM has better simulations of surface rain rate peak than MORR does in the intensity (Figure 4.10). The hourly precipitation rate in SBM has the highest occurrence probability in the range greater than 15 mm h^{-1}, which also shows the best agreement with the observations (Figure 4.11). Figure 4.12 shows that the convective intensity in SBM is stronger than MORR. In general, both SBM and MORR simulates the surface rain rate evolution. However, SBM behaves much better in simulating the location and intensity of convective cells and associated precipitation.

The major differences between SBM and MORR come from the drop nucleation and condensation processes. The calculation of aerosol activation and diffusion growth for the coupling of SBM with MOSAIC based on the explicit supersaturation, while Morrison use an Abdul-Razzak and Ghan (2002) type parameterization to estimate the maximum supersaturation for activation and the saturation adjustment method for condensation process. SBM has ~4.5 times higher condensation rate at ~4-5 km than MORR (Figure 4.16). SBM has ~10% smaller activation rate near cloud base but ~30% larger activation rate above cloud base (~4-5 km) than MORR. The smaller activation rate near cloud base is likely due to the overestimation in maximum supersaturation in the Abdul-Razzak and Ghan (2002) parameterization (Gao et al., 2016). The increased droplet nucleation rate and condensation rate above cloud base in SBM is resulted from the

explicit calculation of supersaturation. The convection and precipitation in SBM are stronger than MORR primarily due to the remarkably increased condensation.

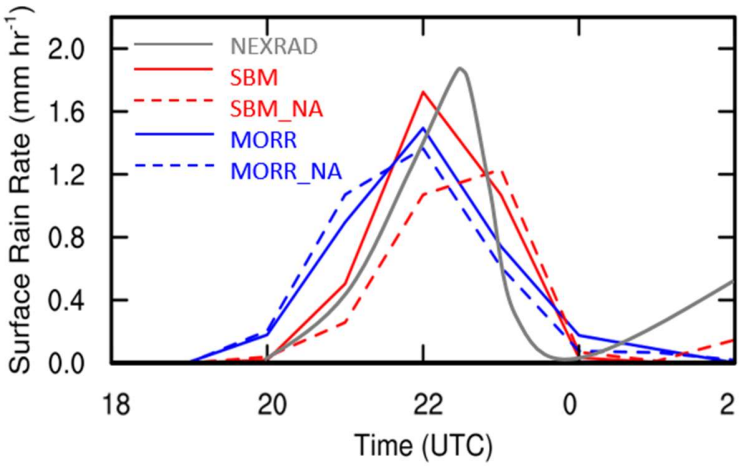

Figure 4.10 Time series of surface rain rate averaged over the red box in Figure 4.8 from NEXRAD, SBM, SBM_NA, MORR and MORR_NA from 1800UTC 19 Jun 2013 to 0200 UTC 20 Jun 2013.

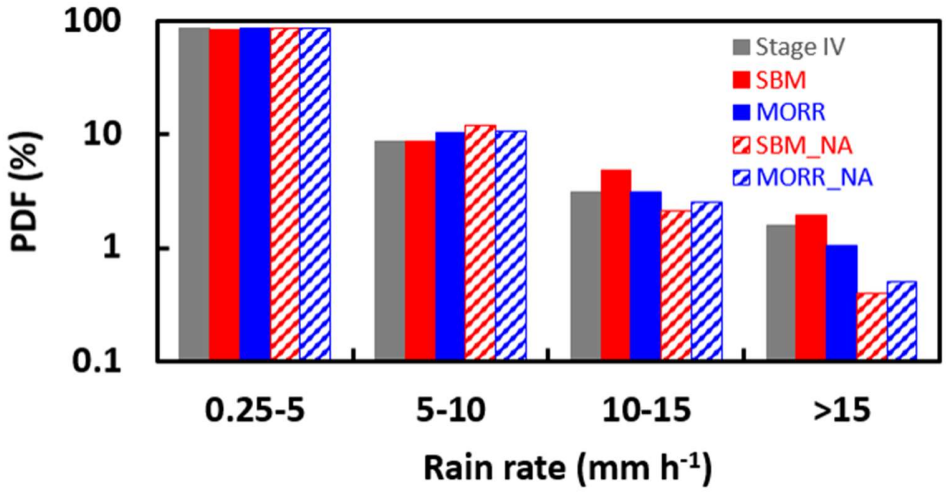

Figure 4.11 The PDFs of rain rate (>0.25 mm h^{-1}) from Stage IV, SBM, SBM_NA, MORR and MORR_NA from 1800UTC 19 Jun 2013 to 0200 UTC 20 Jun 2013 over the analysis domain as shown in the red box in Figure 4.8.

4.5 Simulation of Aerosol Effect on DCC

Figure 4.10 shows that there is a remarkable increase (~35%) in surface rain rate from SBM_NA to SBM. In addition, SBM has higher occurrence probability in the rain rate larger than 10 mm h^{-1} than SBM_NA. However, the enhancement in precipitation from MORR_NA to MORR is much less significant. This is also reflected from the convective intensity as shown in Figure 4.12 and 4.13. Aerosol effects in SBM is much more significant than those in MORR, which contribute to a strong invigoration in upper level updraft speeds (Figure 4.12 and 4.13).

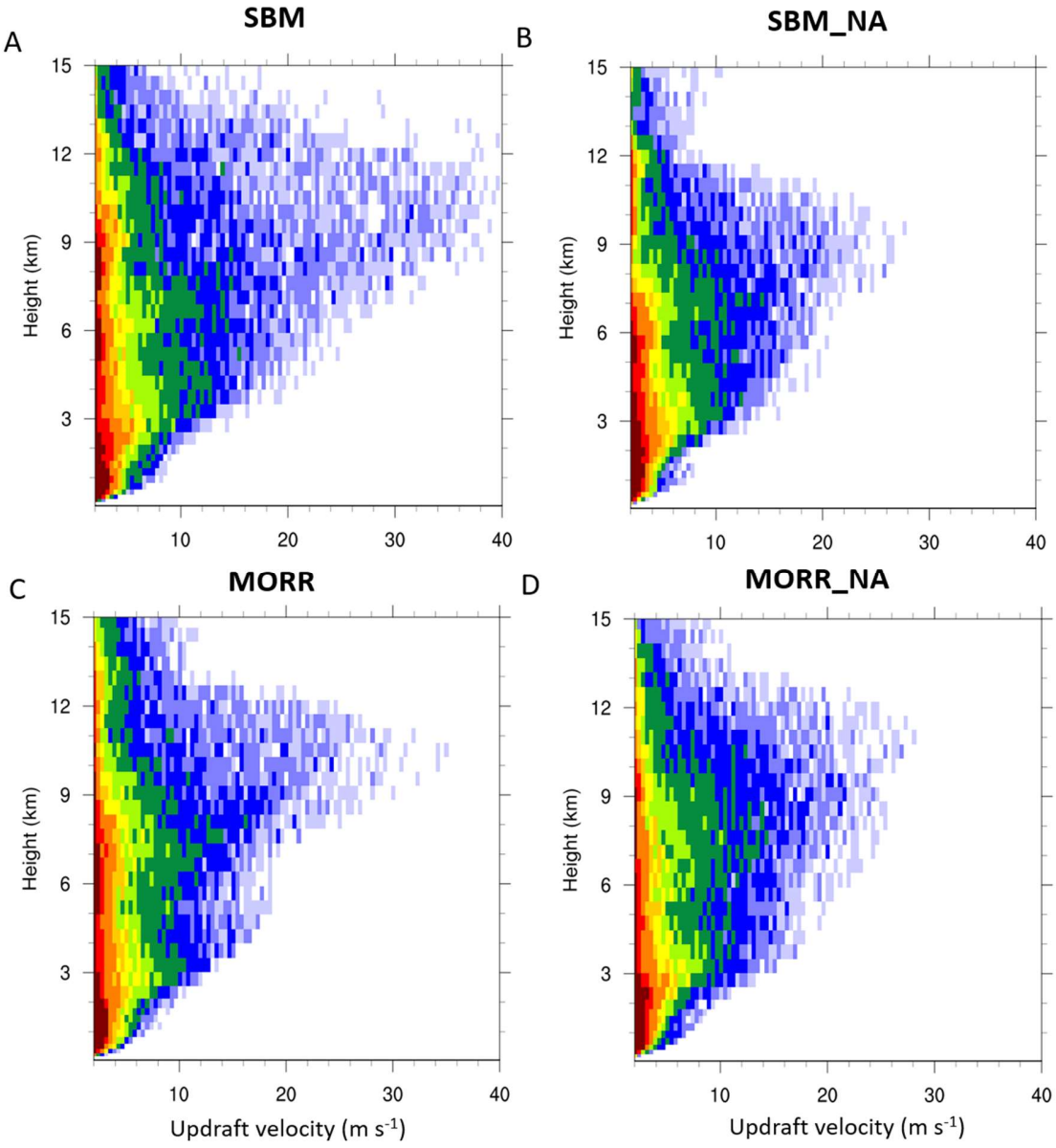

Figure 4.12 The PDFs of updraft velocity ($w>2$ m s^{-1}) during the strong convection period (2100 – 2300 UTC, 19 Jun 2013) over the analysis domain as shown in the red box in Figure 4.8 from the simulations SBM, SBM_NA, MORR and MORR_NA.

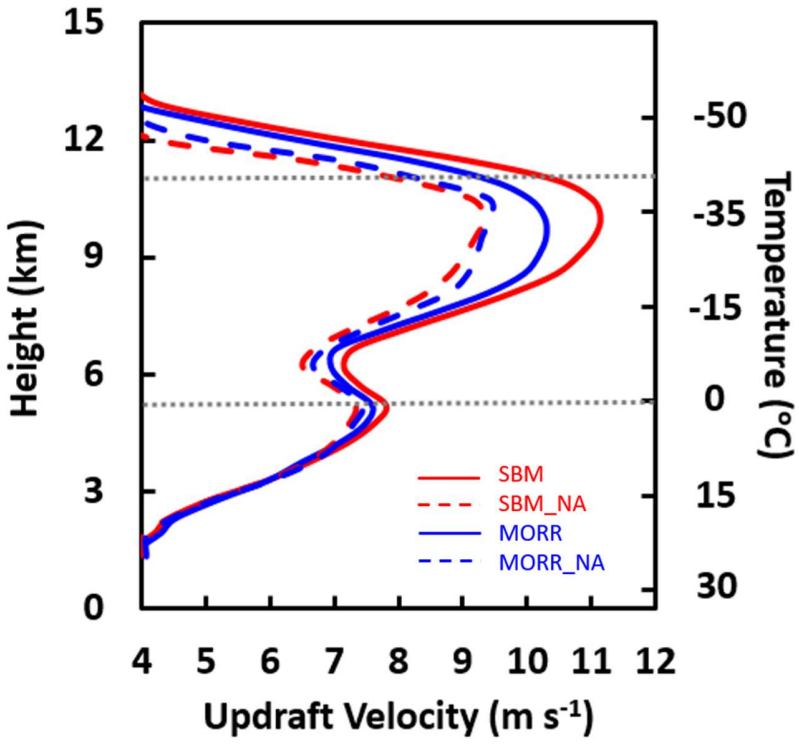

Figure 4.13 Vertical profiles of updraft velocity averaged over the top 25 percentiles (i.e., 75th to 100th) of the updrafts with w>2 m s^{-1} from the simulations SBM, SBM_NA, MORR and MORR_NA during the strong convection period (2100 – 2300 UTC, 19 Jun 2013) over the analysis domain as shown in the red box in Figure 4.8. The dotted lines denote the freezing level (0 ºC) and homogeneous freezing level (-40 ºC).

As shown in Figure 4.13, aerosol markedly invigorates the convection, which can be explained by the increased total buoyancy, although the increased condensate loading effect partially offsets the thermal buoyancy effects (Figure 4.14). Thermal buoyancy, which includes contributions from both temperature and water vapor variations, is the major contributor to the enhanced convection. The increase of thermal buoyancy due to the aerosol effect in SBM is almost doubled than the enhancement in MORR (Figure 4.14), indicating the less significant invigoration of convection by MORR (i.e., MORR_NA vs MORR) than that by SBM (i.e., SBM_NA vs SBM). The thermal buoyancy increase is attributed to the increased net latent heating (Figure 4.14). Note that, from SBM_NA to

SBM, the increase of condensation heating is doubled than the increase in the high-level latent heating (the sum of deposition and freezing), indicating the "warm-phase invigoration" is more important. However, the increase of low-level condensation heating from MORR_NA to MORR is much smaller than that of the high-level. This suggests that the less significant invigoration effect of aerosol by MORR is mainly resulted from the underestimation of the increase in condensation heating which correlates with the warm-invigoration mechanism (Figure 4.14).

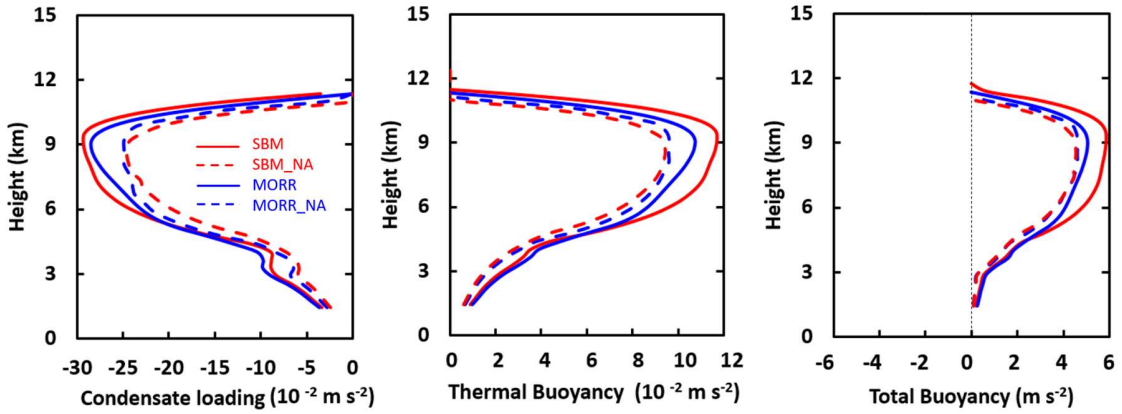

Figure 4.14 Vertical profiles of buoyancy terms (left: condensate loading; middle: thermal buoyancy; right: total buoyancy) averaged over the top 25 percentiles (i.e., 75th to 100th) of the updrafts with w>2 m s^{-1} from the simulations SBM, SBM_NA, MORR and MORR_NA during the strong convection period (2100 UTC – 2300 UTC 19 Jun 2013) over the analysis domain as shown in the red box in Figure 4.8.

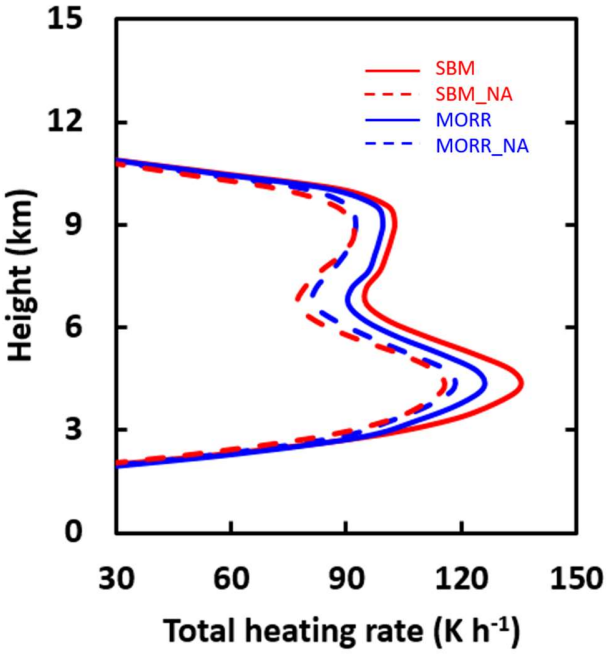

Figure 4.15 Vertical profiles of total latent heating rate averaged over the top 25 percentiles (i.e., 75th to 100th) of the updrafts with w>2 m s^{-1} from the simulations SBM, SBM_NA, MORR and MORR_NA during the strong convection period (2100 – 2300 UTC, 19 Jun 2013) over the analysis domain as shown in the red box in Figure 4.8.

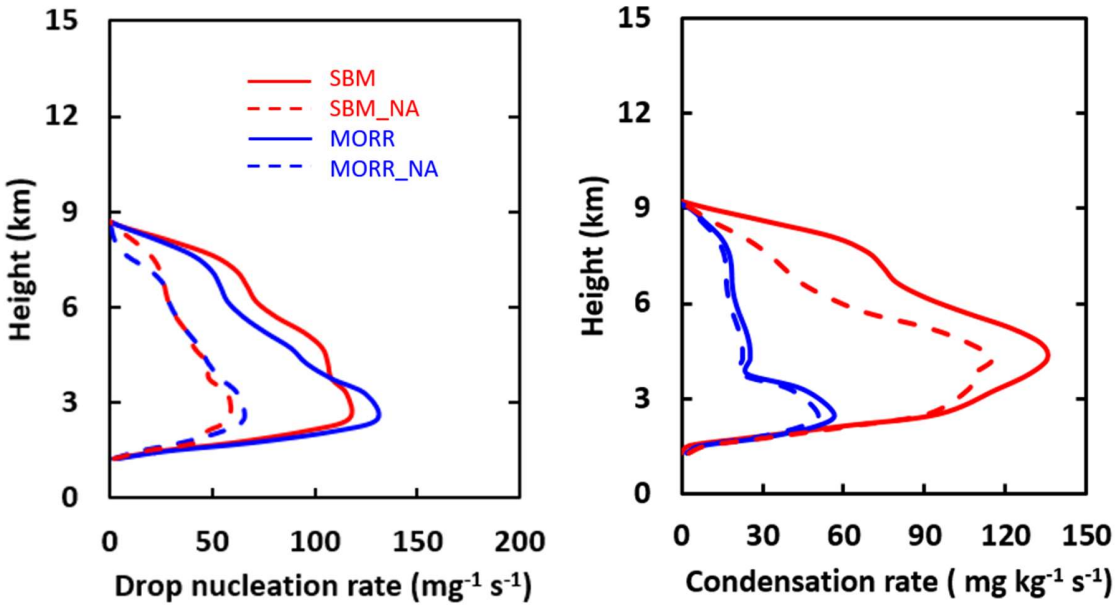

Figure 4.16 Vertical profiles of drop nucleation rate (left) and condensation rate (right) averaged over the top 25 percentiles (i.e., 75th to 100th) of the updrafts with w>2 m s^{-1} from the simulations SBM, SBM_NA, MORR and MORR_NA during the strong convection period (2100 – 2300 UTC, 19 Jun 2013) over the analysis domain as shown in the red box in Figure 4.8.

To understand what processes are mainly responsible for the different latent heat response to aerosols between SBM and MORR, we examine the process rates of droplet nucleation first. As shown in Figure 4.16, the increase in droplet nucleation above 3.5 km from SBM_NA to SBM is ~40% than the enhancement from MORR_NA to MORR. The increase of condensation by SBM (i.e., SBM_NA vs SBM) is ~8 times higher than that by MORR (i.e., MORR_NA vs MORR) (Figure 4.16). The enhanced condensation rate is a result of efficient droplet coalescence above cloud base which reduces integrated droplet surface area for condensation. Compared with drop nucleation, remarkable increase in condensation by SBM (i.e., SBM_NA vs SBM) is the main contributor to the significant aerosol invigorating effect. With the two-moment bulk microphysics, model does not show a significant aerosol impacts on convective intensity and precipitation, due to limitations in the representation of aerosol-cloud interaction processes particularly drop condensation.

4.6 Conclusions

We have conducted model simulations with WRF-Chem to (1) examine aerosol properties over the Houston area, and (2) explore how simulated aerosol impacts are different with bin and bulk microphysics scheme. The increase of aerosol number over urban area is mainly contributed from ultrafine aerosols produced from anthropogenic activities. The simulated surface PM2.5, cloud base heights and CCN at cloud base near the Houston are consistent with observations. Using the WRF-Chem simulated aerosol data, we first employ WRF-Chem coupled with SBM at 0.5 km grid spacing to simulate deep convective clouds occurring on 19-20 June 2013 over the Houston area. The WRF-Chem-SBM can realistically simulate the deep convective clouds in terms of reflectivity

and precipitation better than those by the WRF-Chem coupled with the Morrison two-moment bulk microphysics.

WRF-Chem coupled with SBM shows that with anthropogenic aerosols that have a large number of ultrafine particles lead to a ~35% increase in surface rain rate and a ~30% increase in the mean of top 25 percentiles of updraft speed during the strong precipitation period. The enhanced convective intensity is associated with increased thermal buoyancy, which is attributed to the increased net latent heating. Note that the increase of condensation heating in SBM is doubled than that in the high-level latent heating (the sum of deposition and freezing), indicating warm phase invigoration is more important as far as this case is concerned.

In contrast, the simulations with Morrison bulk scheme do not show a significant aerosol impacts on convective intensity and precipitation, due to limitations in representation of aerosol-cloud interaction processes particularly drop condensation. The bulk scheme has a difficulty in simulating the “warm-phase invigoration” mechanism which is important over the Houston area where the thunderstorms associated with warm cloud bases and humid conditions and large number of ultrafine aerosols are observed.

Chapter 5. Impacts of Land Surface and Aerosol Changes from Houston Urbanization on Convective Storms

5.1 Introduction

Urbanization is an extreme case of land-use change, and it has significant local impacts on weather and climate based on National Climate Assessment (NCA) (2014), including a strong climatological influence on regional thunderstorms (Kellner and Niyogi 2014). Urbanization could impact storm properties through changing urban land-cover and anthropogenic aerosols associated with industrial and population growth.

The land-cover changes associated with urbanization increase surface temperature compared to the surrounding rural area, known as the urban heat island (UHI) effect. Convective storms may be initiated at the UHI convergence zone, created through a combination of increased temperature and mechanical turbulence resulting from complex urban surface geometry and roughness (Bornstein and Lin, 2000; Shepherd, 2005, Hubbart et al., 2014). Urban landscapes can impact sensible and latent heat fluxes, soil moisture, etc, affecting thunderstorm initiation (Haberlie et al., 2015) and changing the location and amount of precipitation compared to pre-urbanization (Shepherd et al. 2002; Niyogi et al. 2011). Another impact of the urbanization is through pollutant aerosols associated with industrial and population growth. Anthropogenic aerosols affect the distribution and radiative properties of non- and precipitating clouds, contribute a substantial forcing to the climate system to varying degrees. Previous studies have shown that urban aerosols invigorate precipitation in urban downwind regions through ACI (Van den Heever and Cotton 2007; Carrió et al. 2010). Few studies have examined the combined effects of both pathways and their relative importance. A very recent study attempting to do this

evaluation for a single storm case showed that land-cover changes increased precipitation over the upstream region but decreased precipitation over the downstream region, while aerosols had the opposite effect (Zhong et al. 2015).

In this Chapter, we examine how urban land and anthropogenic aerosols over Houston impact the evolution of DCCs, convective intensity and precipitation and quantify their respective roles.

5.2 Model experiments

During the summer time over Houston, frequent thunderstorms occur owing to air convergence towards much hotter land surface from the southern humid Gulf air, exacerbated by urban heat island effect. Given warm cloud bases and humid conditions associated with those thunderstorms, it is anticipated that urban anthropogenic aerosols and clouds may exhibit a strong correlation and interaction in this region.

Four experiments (listed in Table 4.1) in this work are (a) LandAero; known as baseline run in which both urban land and anthropogenic aerosols are considered, (b) No_Aero; in which the anthropogenic aerosols are excluded from initial/boundary condition and emission based on LandAero, (c) No_Land; in which the land use and vegetation type for urban are replaced with its surrounding type based on LandAero, and (d) No_LandAero; in which both urban land and anthropogenic aerosols are not considered based on LandAero. The land use types in domain 2 for the simulations with or without urban land are shown in Figure 5.1. In the simulations No_Land and No_LandAero, Houston urban land is replaced by the surrounded Cropland/Grassland.

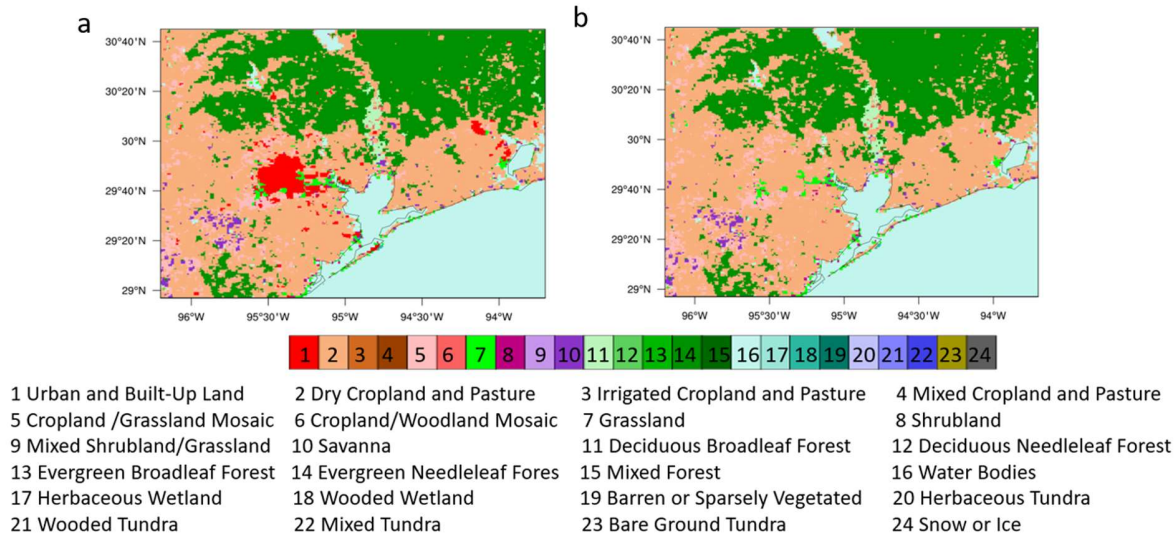

Figure 5.1 Land use categories for the simulations (a) with urban land (LandAero and No_Aero) and (b) without urban land (No_Land and No_LandAero)

5.3 Urbanization Impact on Convective Clouds and Precipitation

The evaluation of baseline run LandAero that has been done in Chapter 4 indicates that the convection and precipitation near Houston is well simulated in terms of location and intensity. Figure 5.2 shows that LandAero has the composite reflectivities (i.e., the column maximum) up to 55dBZ which is consistent with NEXRAD as shown in Figure 4.8 observed over the southeast of Houston city. By comparing LandAero and No_LandAero, urbanization increases the occurrences of high reflectivity (>50 dBZ) and the 0 dBZ echo top height by ~1.5 km (Figure 5.3). Surface peak rain rate is enhanced by ~40% (Figure 5.4). The occurrence probability of heavy rain rates (>15 mm h^{-1}) is an order of magnitude smaller in No_LandAero than in LandAero (Figure 5.5). These results suggest the urbanization over Houston area substantially increases the severity of convective storms and associated precipitation intensity. Both No_Land and No_Aero underestimate the composite reflectivity, 0dBZ echo top height, surface peak rain rate,

frequency of high reflectivity (>50 dBZ) and heavy rain rates (>10 mm h-1). However, the aerosol impact is more evident compared with the urban land effect. The frequency of high reflectivity (>50 dBZ) in No_Land is larger than that in No_Aero (Figure 5.3). Compared with No_LandAero, the surface peak rain rate is enhanced by ~15% in No_Aero and ~30% in No_Land (Figure 5.4), indicating a much larger contribution of aerosols. The weak urban land surface effect in the Houston area might be the dominance of land-sea convergence in triggering convection. The combined effect of urban and aerosol on precipitation is less than the sum of the respective effect from both factors, indicating a nonlinear damping effect on precipitation when two factors work together.

Under the similar initial and boundary meteorological conditions, urbanization of Houston does not significantly affect the initiation of warm clouds near Houston much. However, urbanization leads to the initialization of mixed-phase clouds ~20 min earlier and surface rain ~10 min earlier (Figure 5.4 and 5.6). Those effects are mainly contributed by urban land, not anthropogenic aerosols (Figure 5.6). However, from the mixed-phase to ice phase of deep convection, aerosol effect speeds the development by ~25 min and the urban land does not affect it much (Figure 5.6).

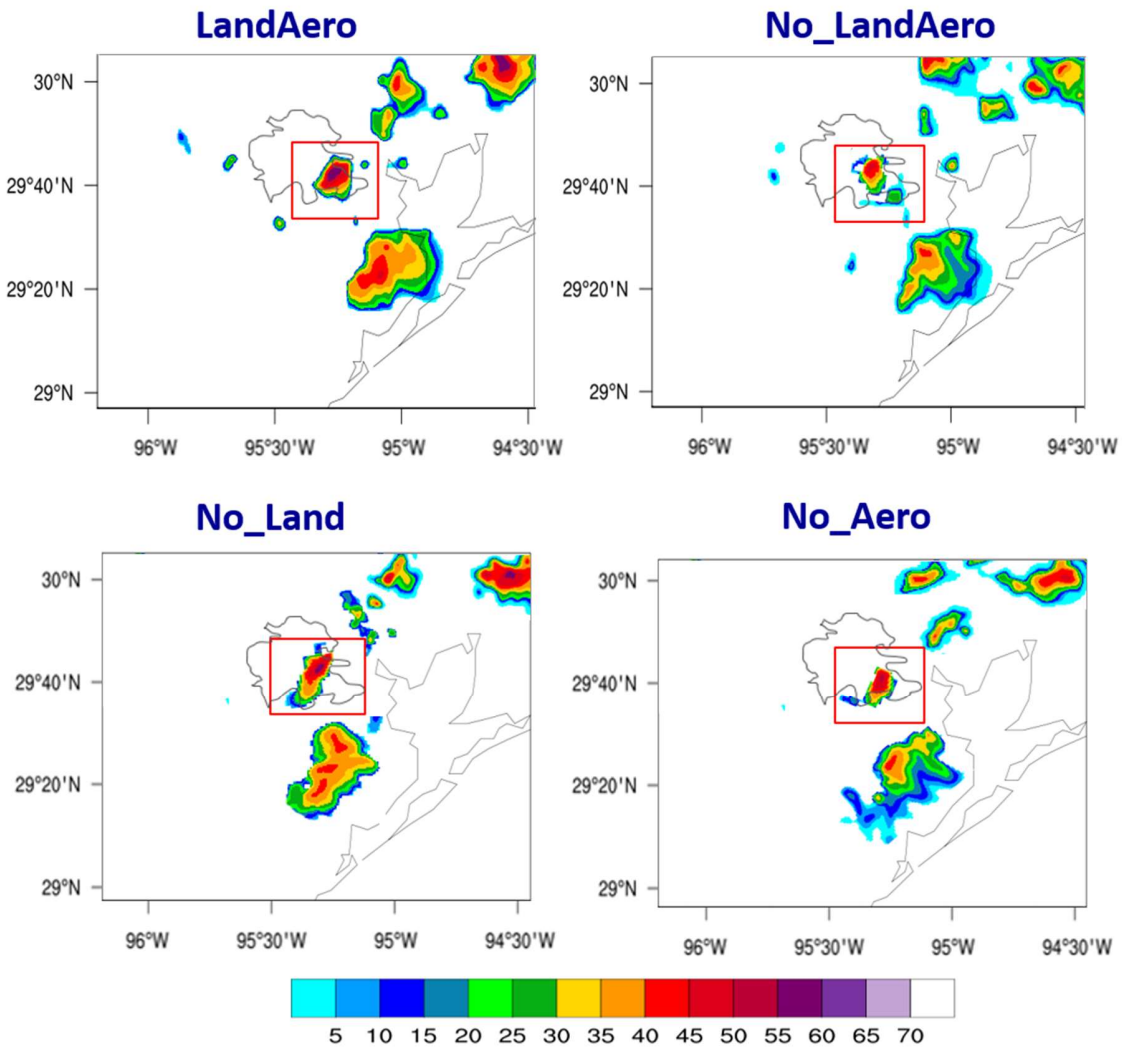

Figure 5.2 Composite reflectivity from LandAero, No_LandAero, No_Land and No_Aero at 2200 UTC 19 Jun 2013 when maximum reflectivity in Houston is observed. Houston city is marked as dark grey solid contour based on the land use in Figure 5.1. The red boxes are the analysis domains for convection cells near Houston.

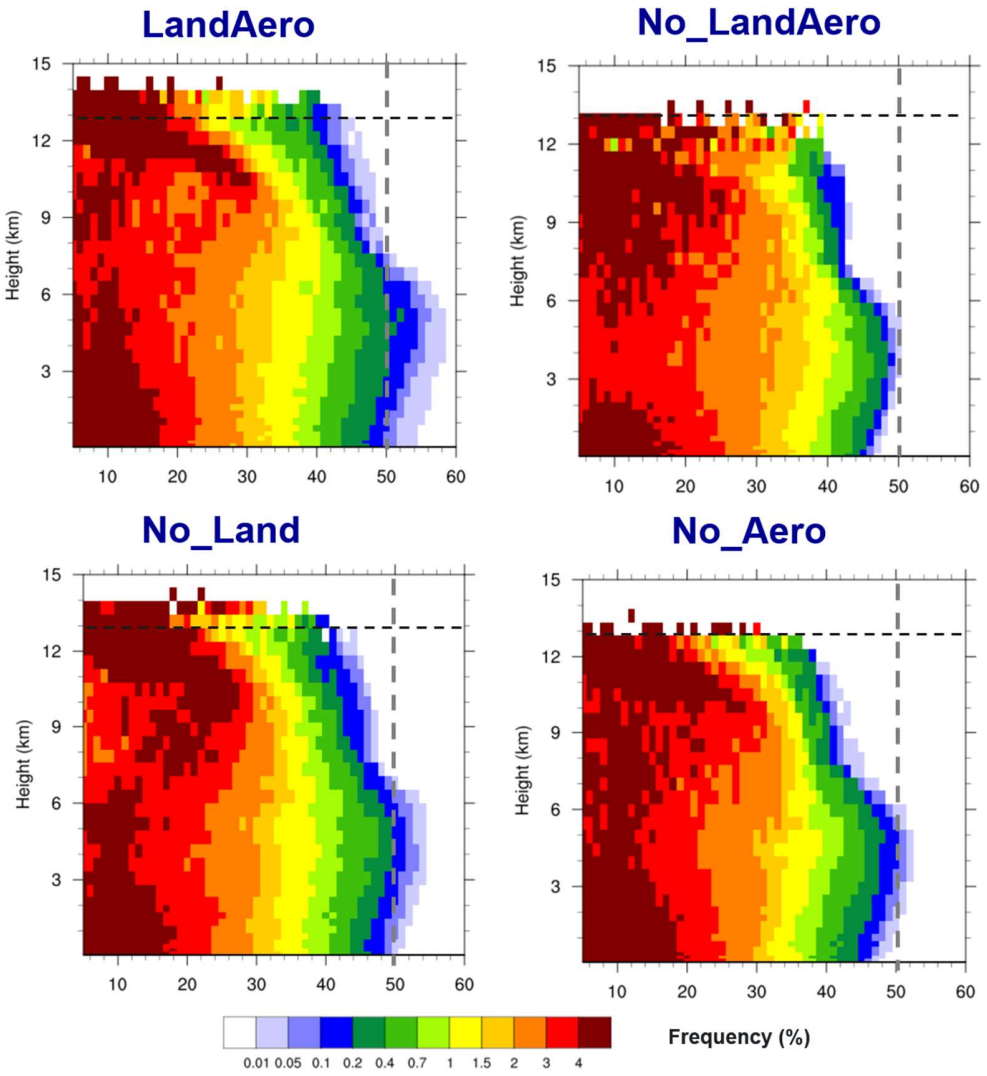

Figure 5.3 The PDFs of reflectivity (>0 dBZ) from LandAero, No_LandAero, No_Land and No_Aero for convection in Houston (red box in Figure 5.2) from 1800 UTC 19 Jun to 0000 UTC 20 Jun 2013.

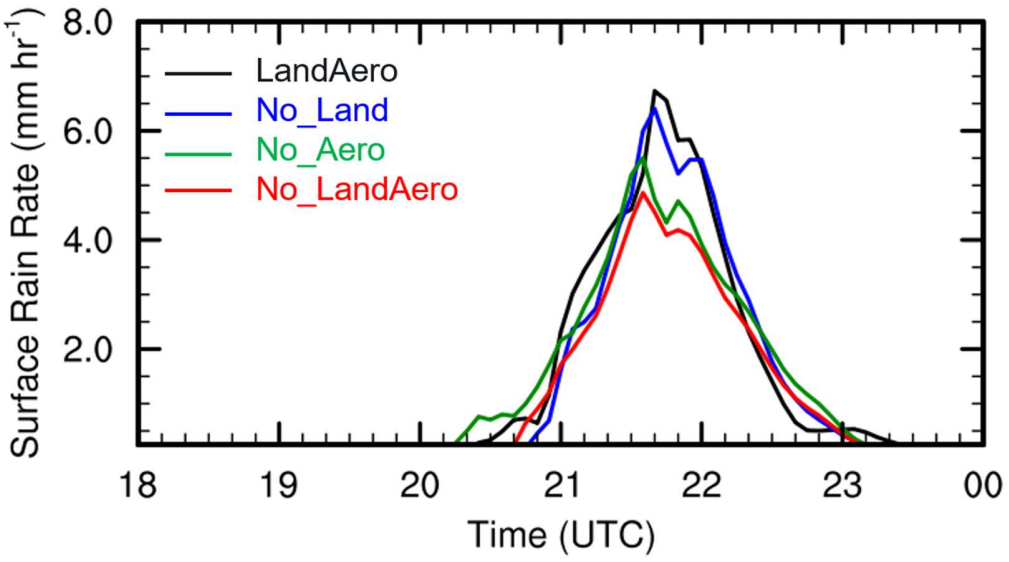

Figure 5.4 Time series of surface rain rate (>0.25 mm h^{-1}) averaged over the red box in Figure 5.2 from LandAero, No_LandAero, No_Land and No_Aero from 1800UTC 19 Jun 2013 to 0000 UTC 20 Jun 2013.

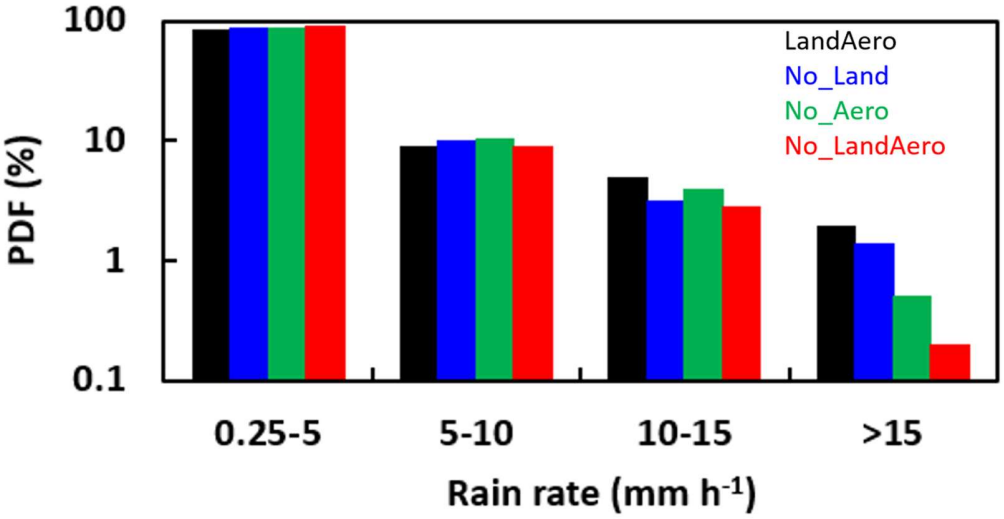

Figure 5.5 The PDFs of rain rate (> 0.25 mm h^{-1}) from LandAero, No_LandAero, No_Land and No_Aero over the analysis domain as shown in the red box in Figure 5.2 from 1800UTC 19 Jun 2013 to 0000 UTC 20 Jun 2013.

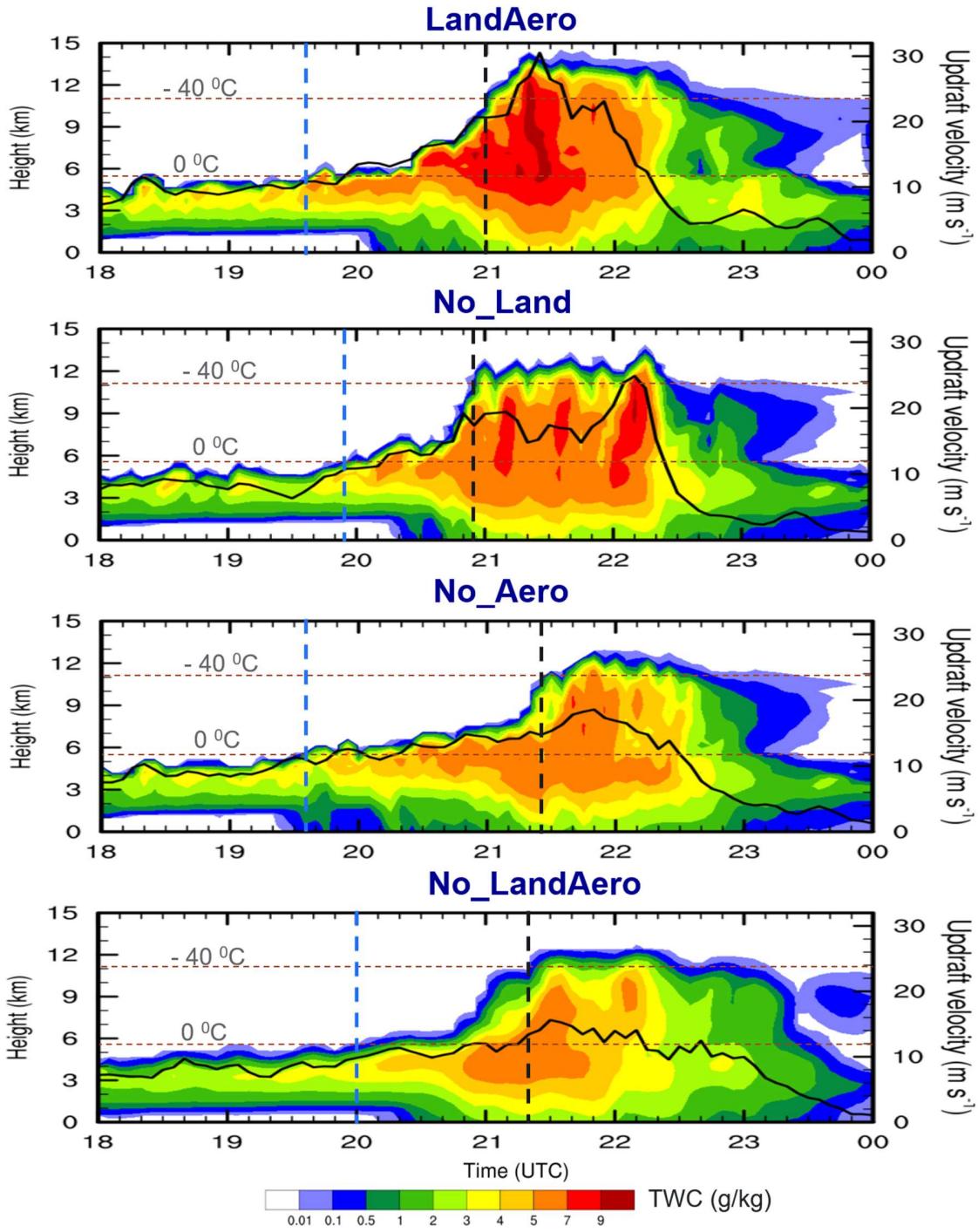

Figure 5.6 Time series of maximum total water content (shaded) and maximum updraft velocity (black line) over the analysis domain as shown in the red box in Figure 5.2 from LandAero, No_LandAero, No_Land and No_Aero. Brown dashed lines denote freezing level (0 ºC) and homogeneous freezing level (-40 ºC). The initiation of mix-phased clouds (blue dashed lines) and ice-phased clouds (black dashed lines) are also marked.

We now explain how the urbanization enhances convective intensity and precipitation and impacts the development of warm clouds to deep convective clouds. As shown in Figure 5.7, urbanization markedly invigorates convection mainly through the effect of increased anthropogenic aerosols. During the strong convection period, the invigoration of updraft velocity (by ~50% in Figure 5.8c) is consistent with the enhancement of thermal buoyancy (Figure 5.9c). The increased thermal buoyancy is contributed from the enhanced latent heating of condensation, deposition, riming and freezing (Figure 5.10), suggesting that anthropogenic aerosols enhance the convective intensity through both "warm-phase invigoration" and "cold-phase invigoration" mechanisms. The dominance of "warm-phase invigoration" is manifested by the remarkable increased condensation heating almost doubling the increase in the high-level latent heating from deposition, riming and freezing (Figure 5.10). The aerosol effect in rain, snow and graupel mass (Figure 5.11) is mainly because of invigorated convection, explaining the enhanced surface peak rain rate.

Next, we explain the urban land effect and aerosol effect in impacting the evolution of convective clouds and precipitation. As shown in Figure 5.6, during 1920 UTC – 1950 UTC, LandAero and No_Aero have developed from warm to mixed-phase clouds when No_Land and No_LandAero are still in the stage of warm clouds. The urban land speeds up the development from the warm cloud regime to the mixed-phase regime and is more significant than the aerosol effect (Figure 5.8a). The invigorated convection due to land effect can be explained by the increased thermal buoyancy from surface to cloud regime (Figure 5.9a), which mainly results from the increased temperature over Houston area (Figure 5.12a). The maximum increase in 2-m Temperature over Houston could be up to 2

ºC because of up to ~20 W m^{-2} increase in total surface heat flux (Figure 5.12). With the urban land effect, air is heated up, which fuels the convection and thus initiate deep clouds much earlier. Surface precipitation starts after the initiation of mixed-phase clouds. Therefore, the land effect also initiates the surface precipitation ~20 min earlier (Figure 5.4). The aerosol effect contributes to a ~10 min delay of precipitation (Figure 5.4) by slowing drop coalescence process. During the developing period from mixed-phase clouds to ice-phase clouds (2000 UTC -2050 UTC), the convection develops higher and invigorates by ~30% from No_LandAero to LandAero (Figure 5.8b). The aerosol effect becomes more important than the land effect by comparing the difference of (No_Land-No_LandAero) with that of (No_Aero- No_LandAero) (Figure 5.8b and 5.9b). This is because the "warm-phase invigoration" due to the aerosol effect becomes more significant in the mixed-phase clouds period after rain start. After the precipitation starts under the warm and moist condition, the atmosphere is highly supersaturated since integrated droplet surface area for condensation is reduced, allowing the additional activation of UAP which release a large amount of additional latent heat at the low and middle levels. As a result, aerosol effect speeds the development to ice phase of deep convection.

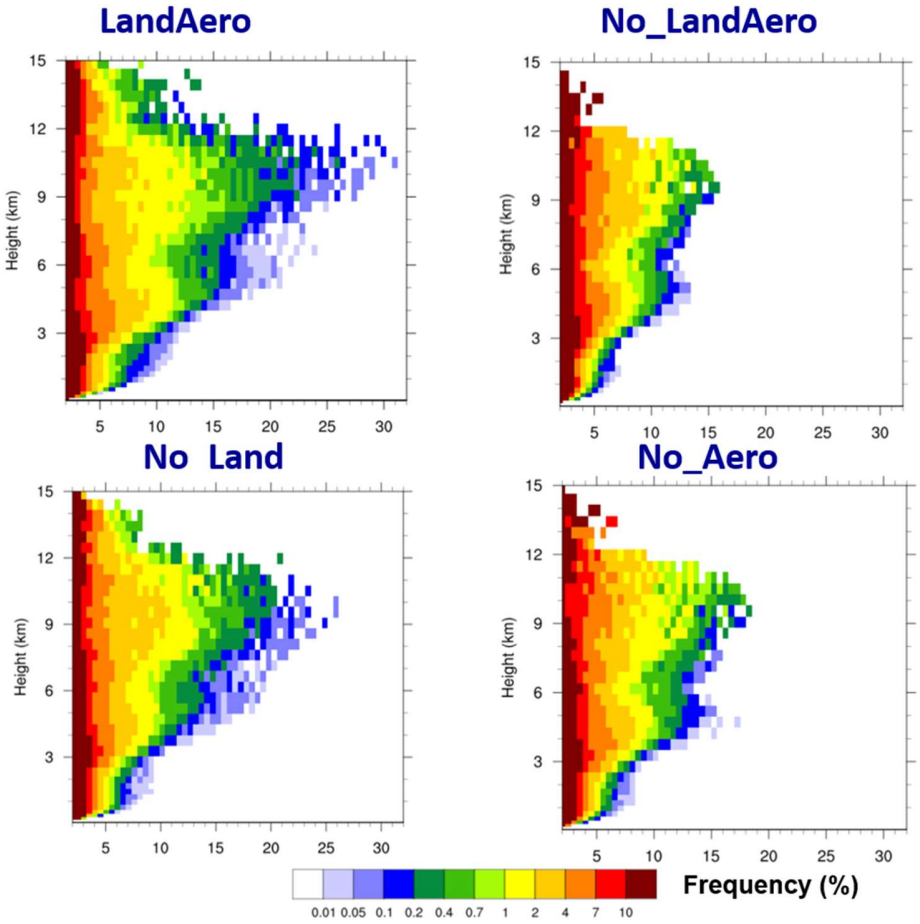

Figure 5.7 The PDFs of updraft velocity (w>2 m s^{-1}) from LandAero, No_LandAero, No_Land and No_Aero over the analysis domain as shown in the red box in Figure 5.2 during the strong convection periods (60-min duration with 30 min before and after the strongest convection).

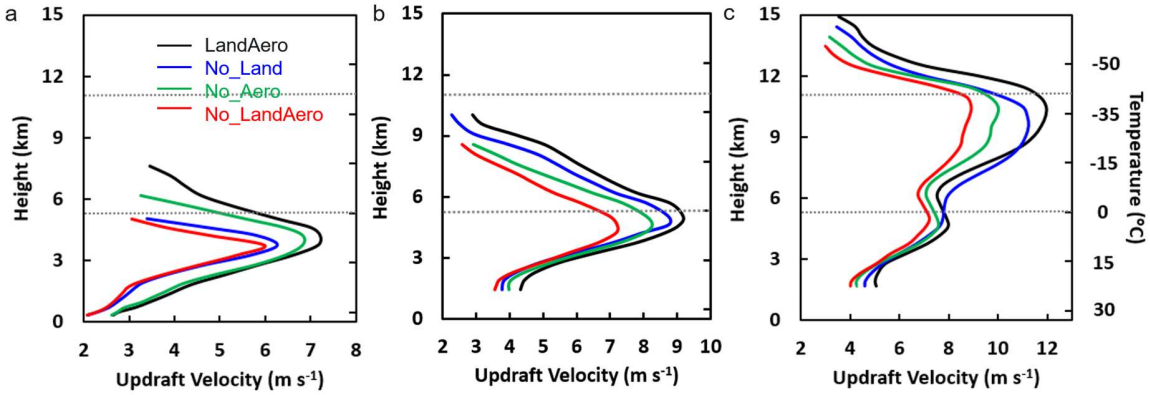

Figure 5.8 Vertical profiles of updraft velocity averaged over the top 25 percentiles (i.e., 75th to 100th) of the updrafts with w>2 m s^{-1} from the simulations LandAero, No_LandAero, No_Land and No_Aero over the analysis domain as shown in the red box in Figure 5.2 during (a) warm clouds developing to mixed-phase clouds period in LandAero (1920 UTC – 1950 UTC), (b) mixed-phase developing to ice-phase clouds period in LandAero (2000 UTC -2050 UTC) and (c) strong convection periods (60-min duration with 30 min before and after the strongest convection). (b) and (c) only plot the cloud regime because of the precipitation.

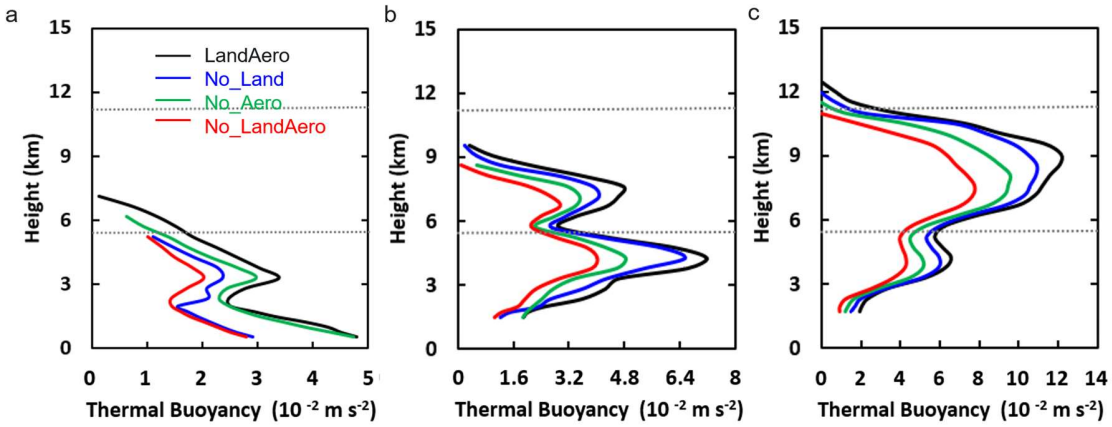

Figure 5.9 Same as Figure 5.8 except for thermal buoyancy averaged over the top 25 percentiles of the updrafts with w>2 m s^{-1}.

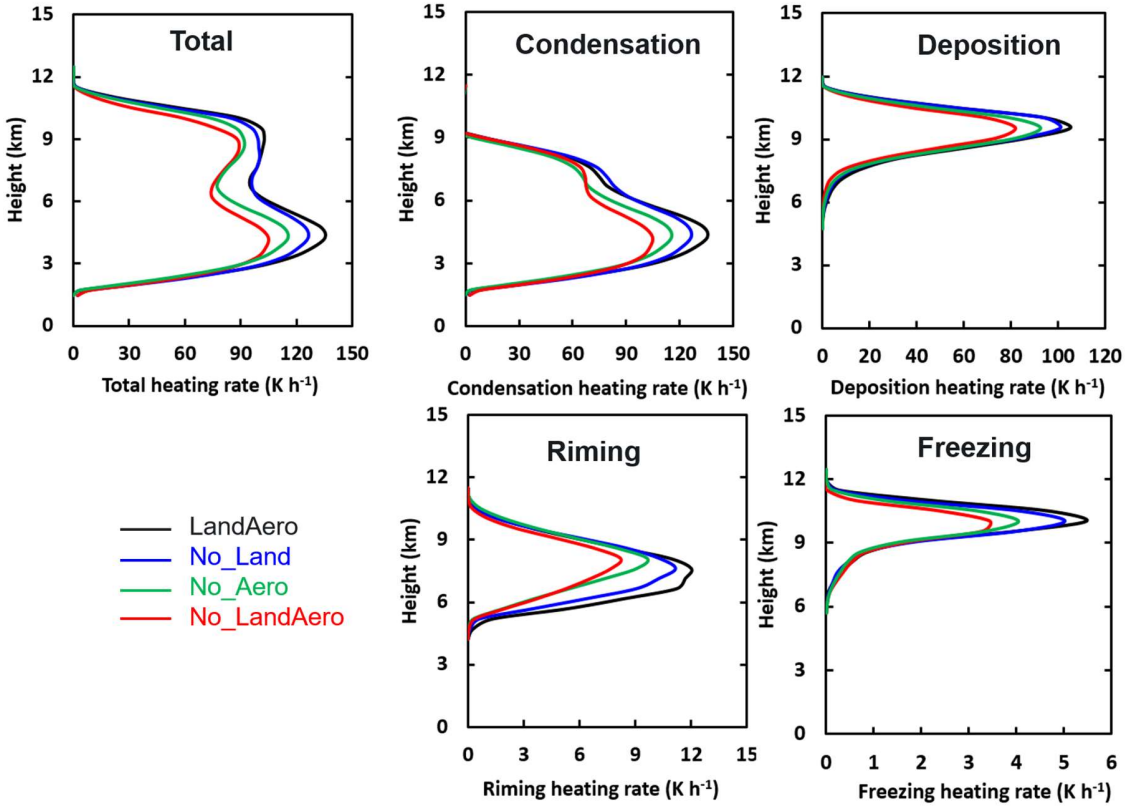

Figure 5.10 Vertical profiles of total latent heating rate, latent heating rates for condensation, deposition, riming and freezing averaged over the top 25 percentiles (i.e., 75th to 100th) of the updrafts with w>2 m s^{-1} from the simulations LandAero, No_LandAero, No_Land and No_Aero over the analysis domain as shown in the red box in Figure 5.2 during the strong convection periods (60-min duration with 30 min before and after the strongest convection).

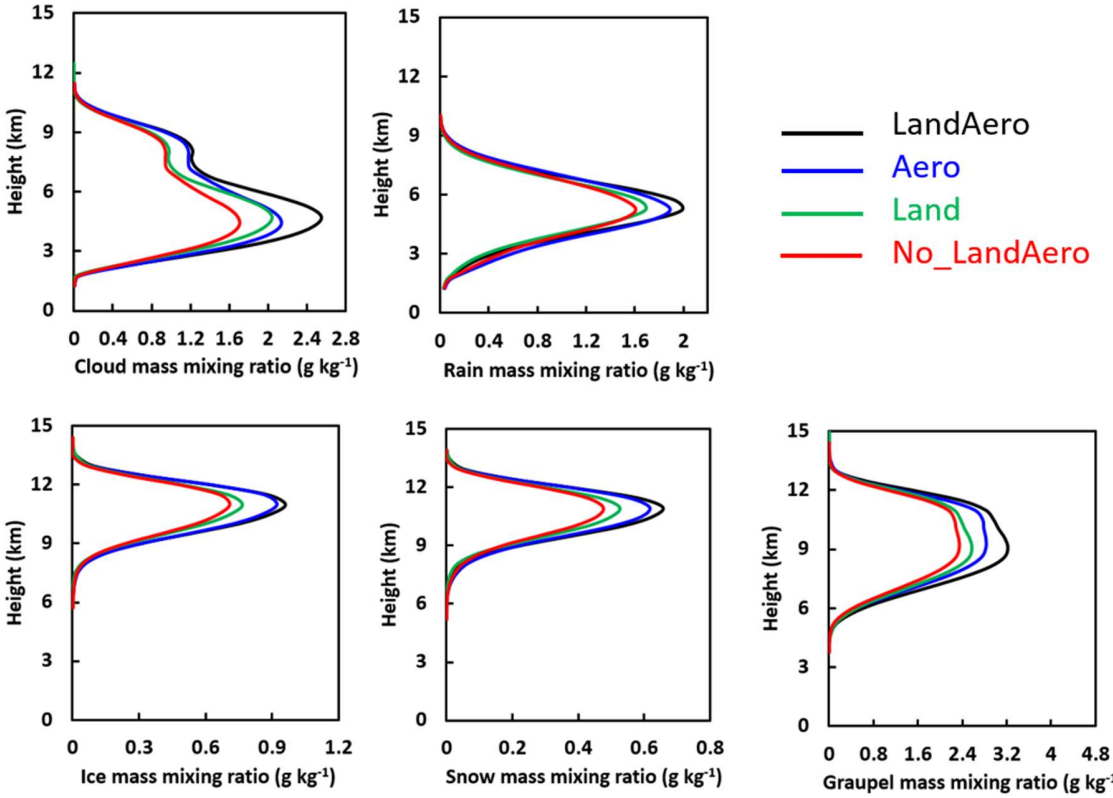

Figure 5.11 Vertical profiles of cloud, rain, ice, snow and graupel mass mixing ratio averaged over the top 25 percentiles (i.e., 75th to 100th) of the updrafts with w>2 m s^{-1} from the simulations LandAero, No_LandAero, No_Land and No_Aero over the analysis domain as shown in the red box in Figure 5.2 during the strong convection periods (60-min duration with 30 min before and after the strongest convection).

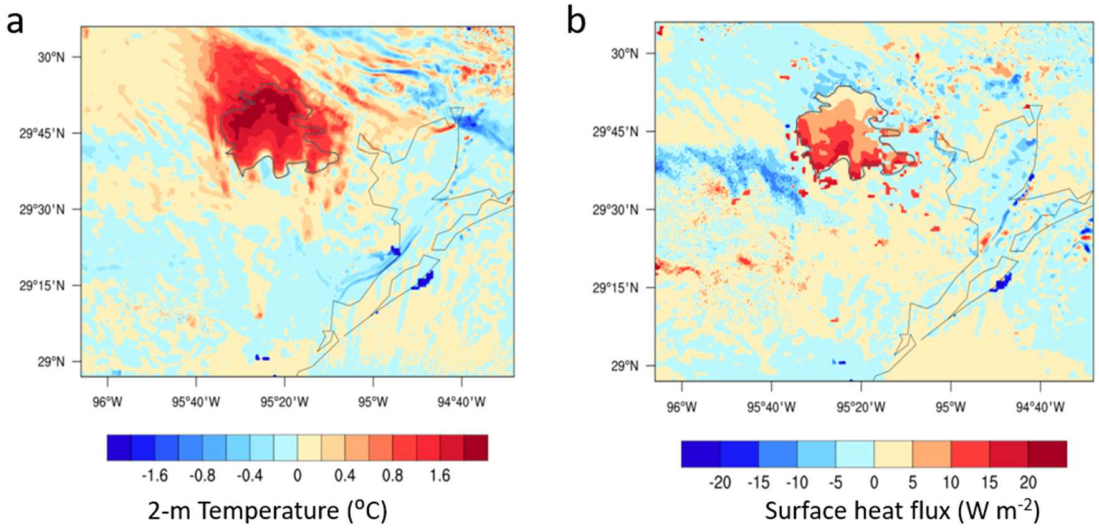

Figure 5.12 Change of (a) 2-m Temperature and (b) total surface heat flux from No_Land to LandAero at 1600 UTC 19 Jun 2013 (2 h before the warm clouds formed near Houston).

5.4 Conclusions

During the summer time over Houston, thunderstorms occur frequently initiated by warm clouds of low bases under humid conditions, which may be affected by urban land and anthropogenic aerosols. We conduct sensitivity tests to examine how urban land and anthropogenic aerosols impact the deep convective clouds and precipitation individually, as well as jointly, based on the case chosen on 19-20 June 2013 over Houston. We find that urbanization in Houston enhances convective intensity and precipitation, primarily due to the urban aerosol effects. The aerosol enhances the convection through both "warm-phase invigoration" and "ice-phase invigoration", and the former is more significant. The urban land effect does impact convective evolution. The land effect fastens the convection developing above the freezing level and forms deep clouds ~20 min earlier due to urban heating. The anthropogenic aerosols do not affect the initiation of mixed-phase clouds much. However, it enhances the development of from the mixed-phase and ice-phase

regimes due to much increased latent heating from microphysical processes (mainly through condensation).

Chapter 6. Wildfire Impact on Environmental Thermodynamics and Severe Convective Storms

6.1 Introduction

Wildfire frequency and burned area have been increasing in recent decades globally, particularly in the western United States (e.g., Miller et al., 2012; Dennison et al., 2014). It is well-known that wildfires can cause substantial increases in the emissions of gases including health-hazardous gas pollutants and greenhouse agents such as carbon monoxide, nitrogen oxides, ozone, as well as aerosol particles (Phuleria et al., 2005; Liu et al., 2017). Much less is known about the latter than the former effects. Aerosols released from wildfires can affect weather and climate through aerosol-radiation-cloud-interactions (Lindsey and Fromm, 2008; Lu and Sokolik, 2013; Lee et al., 2018a; Logan, 2018; Logan et al., 2018). Besides the emissions of gases and aerosol particles, they simultaneously release a large amount of heat to the lower and middle troposphere and dramatically impact environmental thermodynamics (Trentmann et al., 2006; Kablick et al., 2018). Large fires also release water vapor as a by-product of combustion, which could affect environmental thermodynamics (Peterson et al., 2016). PyroCb clouds, a fire-induced variety of deep convection that often rises to the upper troposphere or lower stratosphere (Luderer et al., 2006), can be impacted by the fire emissions of sensible heat, aerosol particles, and water vapor in a complex way that is still poorly understood, due to poor model capability of simulating their combined effects.

Pyrocumulonimbus (PyroCb) is associated with a hot surface temperature, strong surface winds, low relative humidity, and deep mixed layer (Fromm et al., 2006, 2012; Cruz et al., 2012; Lareau and Clements, 2016; Clements et al., 2018). This

type of deep convective cloud is unique in its microphysical structure for the following reasons: (1) there exist high concentrations of small cloud droplets that result from a large number of CCN due to the aerosol particles emitted by fire that compete for limited condensable water vapor (Andreae at al., 2004), and (2) these clouds initiate and develop under the vigorous dynamics and thermodynamics induced by the fire itself. The buoyancy generated by the sensible heat of wildfires can produce very strong updrafts (Lareau and Clements, 2017; Tory et al., 2018) which can further enhance the aerosol activation at the cloud base by increasing the supersaturation (Luderer et al., 2006; Trentmann et al., 2006; Kablick et al., 2018). Note that pyroCbs often produce severe weather events that include large hail (>25 mm), enhanced lightning activity, extreme low-level winds, and in some cases even tornadoes (Fromm et al., 2006; Rosenfeld et al., 2007, Lareau et al., 2018). PyroCbs are also found to produce an anomalously high number of positive lightning flashes, while the lightning produced in ordinary thunderstorms is typically dominated by negative lightning flashes (Rosenfeld et al., 2007; Jungwirth et al., 2005). Positive lightning is often an order of magnitude stronger than negative lightning (Jungwirth et al., 2005). The occurrence of high percentage, high rate, and high density of positive lightning has a direct relationship with storm severity and is coincident with the production of large hail (Rosenfeld and Woodley, 2000; Williams et al 2005; Logan, 2018, Wang et al., 2018).

Previous studies (Luderer et al., 2006; Kablick et al., 2018) simulated the impact of wildfires by changing the initial backgrounds with prescribed heat and aerosol emitted by the wildfire. Modeling of wildfire impact in regional and global climate models (RGCMs) has been difficult because (1) wildfire plume rise is often a complex function of the size of the wildfire, fire heat flux, and the atmospheric environmental conditions, and (2) model

grid-spacing needs to be very small (e. g., <100 m) to simulate fire dynamics, which is generally not yet affordable in RGCMs. Various schemes for parameterizing the rise of a plume, ranging from simple empirical-based schemes such as Briggs, Sofiev, and DAYSMOKE (Briggs 1975; Liu et al., 2017; Sofiev et al., 2012) to relatively sophisticated prognostic 1-D parcel models that include cloud microphysics and entrainment (Freitas et al., 2007), have been developed over the years in an effort to determine the injection height of wildfire emissions. There are detailed fire models that can explicitly resolve fire spread and fire plume dynamics, e.g., MesoNH-ForeFire (Filippi et al., 2011) and SFIRE that was coupled with WRF (Mandel et al., 2011 and Mandel et al., 2014) and WRF-Chem (Kochanski et al., 2012, 2013). However, such fire models are computationally expensive. For example, the WRF-Chem-SFIRE simulation costs about 50% more than the simulation without SFIRE in the Mallard Fire case that will be discussed in the following section. In addition, it is challenging to run these expensive simulations in weather forecasts and RGCMs. Furthermore, our poor understanding of fire ignition and the limitation on defining variable ignition locations and sources in a detailed fire model could pose a large model uncertainty. Thus, a relatively simplified subgrid plume parameterization is more practical in model applications, particularly considering the computational cost.

In WRF-Chem, the subgrid plume model is represented by embedding a 1-D time dependent cloud model (Freitas et al., 2007) within each column of WRF-Chem. However, currently the subgrid dispersion is only considered for aerosols emitted from wildfires (Grell et al., 2011). The heat effect of wildfires on environmental thermodynamics has not been considered, which was noted as a potential development area in Grell et al. (2011). At a relatively coarse resolution (e.g., ~30 km), fire burning has a much smaller scale than

the model grid, so the heat likely has a small impact on the grid-mean temperature. However, models that run at cloud-resolving and convection-permitting scales (km) at which the grid-size is comparable to or even smaller than the burned areas of wildfires, the heat effect of wildfires on grid-scale temperature can become important and should be considered.

Therefore, the first goal of this Chapter is to enable WRF_Chem to account for impacts of both aerosols and heat from wildfires without adding obvious computational cost. Second, we will use the new WRF-Chem model to examine the role of the wildfire in altering pyroCb properties including convective intensity, hailstone size, and lightning behavior, as well as the relative importance of the heat impact relative to the aerosol impact. The unique aspects of this study lie in the development of a new model capability to account for heat effect computational efficiently in RGCMs, the application to a real fire event that was well characterized in a field experiment, and the quantification of the respective heat effect and aerosol effect on convective extremes. This is the first step for the community to systematically examine wildfire impacts on regional and global extreme storms and precipitation.

6.2 Model Development and Evaluation

In order to account for the heat effect of wildfires without adding significant computational cost to the WRF-Chem model, our method is based on the existing subgrid 1-D plume rise model (Freitas et al., 2007). The evolution and injection height of the fire plume is estimated by the 1-D plume rise model originally developed by Latham (1994) at each grid column of the 3-D host model (i.e., WRF-Chem). The final height that the plume reaches is determined by the thermodynamics of the atmospheric environment acquired

from the host model and the surface heat flux release from wildfires. All wildfires are aggregated into three categories (forest, woody savanna, and grassland) by merging the fire location with the land use dataset. The heat fluxes of different types of wildfires are obtained from the data in Table 1 of Freitas et al. (2006). The heat fluxes used for forest, woody savanna, and grassland are 80, 23, and 3.3 kW m^{-2}, respectively. The sub-grid plume rise model is driven by environmental dynamics from the atmosphere model in WRF-Chem and the plume dynamics is estimated based on fire information from FINN (Freitas et al., 2007). The hourly biomass emission, active fire location, and burning area were obtained from FINN model (Wiedinmyer et al., 2011). The location and timing for the fires are identified globally using the Moderate Resolution Imaging Spectroradiometer (MODIS) Thermal Anomalies Product. The Global Land Cover Characteristics 2000 dataset and the MODIS Vegetation Continuous Fields Product were used to determine the burned area for each vegetation type based on percentage vegetative cover in each 1 km^2 fire pixel. The FINN data are then interpolated to the host model grid. For grid points with fire according to FINN, the sub-grid plume rise model is driven by the environmental dynamics from the atmosphere model in WRF-Chem and the plume dynamics are estimated based on fire information from FINN (Freitas et al., 2007). The final height of the plume is then used in the source emission field of the host model to determine the effective injection height where heat and aerosols emitted during the flaming phase would be released and interact with the atmosphere circulation and transport. The aerosol emission from the fire is added as described in Grell et al. (2011). The heat flux from the plume model which assumes an exponential decay with altitude is input to the atmosphere model by being treated as an

additional forcing term in the thermodynamics equation of the atmosphere model for potential temperature θ, equal to the vertical divergence of the heat flux,

$$\frac{d(\mu\theta)}{dt}(x,y,z) = \boldsymbol{R_\Theta}(\boldsymbol{\Phi}) + \frac{\mu(x,y)\phi_h(x,y)}{\sigma\rho(x,y,z)}\frac{\partial}{\partial z}exp\left(-\frac{z}{z_{ext}}\right)$$

where μ(x,y) is the hydrostatic component of the pressure differential of dry air between the surface and the top of the domain, $\boldsymbol{R_\Theta}(\boldsymbol{\Phi})$ is the component of the source term (commonly called "tendency" in WRF) in the atmospheric model thermodynamic equation, σ is the specific heat of the air, ρ(x,y,z) is the density, and zext is the heat extinction depth (Mandel et al. 2011). This is done in the same way as WRF-SFIRE as described in Mandel et al. (2011). Note that, unlike WRF-SFIRE, in which the heat fluxes are calculated by SFIRE, we estimate the heat fluxes in a simple and less-expensive way following the equation $\sum_i(HF_i \times BA_i)/grid\ size$, where HF_i denotes the heat flux of each fire type and BA_i is the burned area of each type. Thus, no significant computational cost is added.

Our initial evaluation of the new model capability in WRF-Chem uses 3-km resolution for wildfires without accompanied pyroCb. For the evaluation of the improved WRF-Chem model at 3-km resolution for wildfires without pyroCb, we run the WRF-Chem simulations of wildfires over the central United States from 1200 UTC 15 July to 1200 UTC 19 July 2016. The simulated domain is shown in Figure 6.4 with 65 vertical levels. We use the CBMZ gas-phase chemistry (Zaveri and Peters, 1999) and MOSAIC aerosol model with four bins (Zaveri et al., 2008). The physics schemes applied in the simulation are the Unified Noah land surface scheme (Chen and Dudhia, 2001), Yonsei University planetary boundary layer scheme (Hong et al., 2006), the RRTMG longwave and shortwave radiation schemes (Iacono et al., 2008), and Morrison two-moment

microphysics scheme (Morrison et al., 2005) with the hail option. The initial and lateral boundary conditions for the meteorological fields were produced from the Rapid Refresh (RAP) model that is comprised primarily of a numerical forecast model and an analysis/assimilation system at 13-km resolution (Benjamin et al. 2016). The chemical lateral boundary and initial conditions were created from MERRA-2 (Gelaro et al., 2017). The meteorological field was reinitialized every 30 hours with the RAP data. The anthropogenic emission was from NEI-2011 emissions. The biogenic emission came from MEGAN product (Guenther et al., 2006). To evaluate the temperature profiles on 18 July 2016, we use the sounding data from the National Oceanic and Atmospheric Administration / Earth System Research Laboratory ((NOAA/ESRL) radiosonde database. Soundings are found at the three locations having near surface winds blowing from an adjacent significant wildfire (Figure 6.1). We evaluate the low-level temperature profiles with the radiosonde data. The evaluation shows an environmental temperature increase of roughly 2-3 °C near the surface by accounting for the sensible heat flux from wildfires by comparing with the simulation without wildfire heat, leading to a better agreement with observed temperature (Figure 6.2).

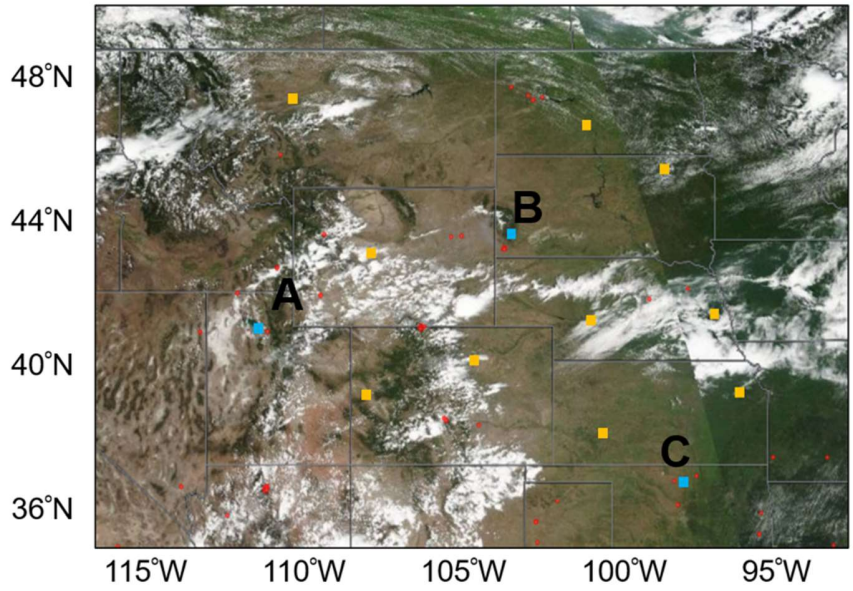

Figure 6.1 True Color image and Fires/Thermal Anomalies (red dots) from Suomi NPP/ VIIRS and NOAA/ESRL Radiosonde stations (blue or yellow squares) in the simulated domain on 17 July 2016.

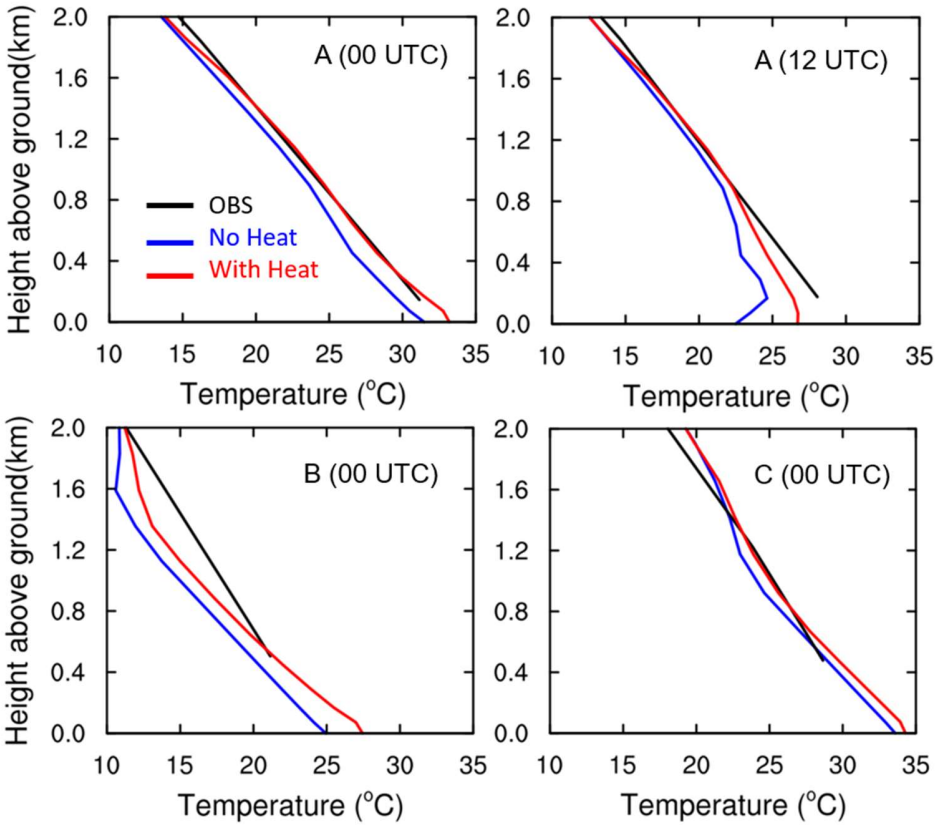

Figure 6.2 Temperature profiles from the observation (black), the simulation with the original WRF-Chem (blue) and the simulation from the improved WRF-Chem with heat flux accounted (red) for three sounding stations close to fires (blue squares in a) on 18 July 2016. Other stations did not have measurements obviously influenced by wildfires.

The WRF-Chem model with the new plume model development is further evaluated at 1-km resolution with observations from a well-observed wildfire event that induced a pyroCb and a corresponding simulation from WRF-Chem-SFIRE, which explicitly simulates fires. The Mallard Fire in the panhandle of Texas, which burned more than 260 square kilometers, began on the evening of 8 May 2018 and lasted for over one week and charred primarily savannah vegetation. The Mallard Fire induced a pyroCb occurred on 11-12 May 2018 as observed from GOES-16 (Figure 6.4). This impressive pyroCb was initiated at the Mallard Fire region and intensified when moving downwind (Figure 6.3). It produced both large hailstones (25 mm) and frequent lightning (numerous positive cloud-to-ground and intra-cloud lightning pulses) over the region between Texas and Oklahoma (35.2-35.7ºN, 99.5-100.5ºW). The baseline simulation includes the impact of both heat flux and aerosol emissions using the new plume model and is referred to as Wildfire. The WRF-Chem-SFIRE simulation uses the same model setup as Wildfire. The simulations are conducted at 1-km resolution over a domain shown in Figure 6.4. The simulations are initiated at 0000 UTC 9 May and run out to 0000 UTC 14 May 2018. To evaluate Wildfire with the new plume model development, WRF-Chem-SFIRE is run, which uses the similar model configuration as Wildfire. The inner fuel model for fire in WRF-Chem-SFIRE uses a resolution of 50 meters that is 20 times finer than the atmospheric model grid. To examine temperature anomalies induced by the fires in Wildfire and WRF-Chem-SFIRE, we conduct an additional WRF-Chem simulation in

which both the heat flux and aerosol emissions from the wildfire are turned off (referred to as No_Wildfire).

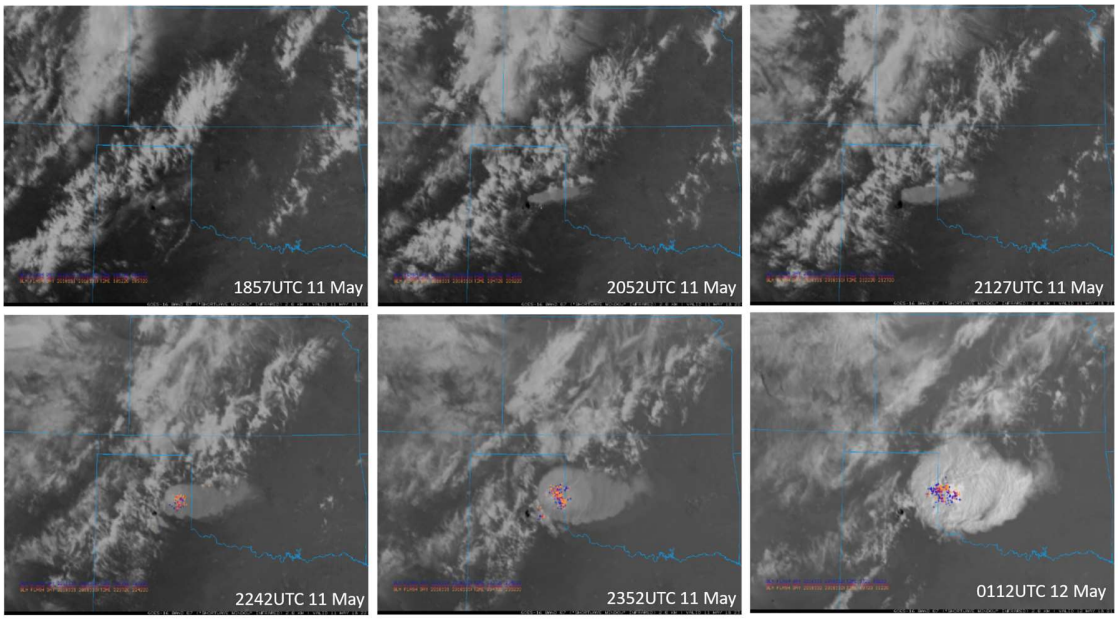

Figure 6.3 The observed evolution of pyroCb from GOES-16 Band 7 ("shortwave window" Infrared) and the lightning strokes (marked as "+") from the Geostationary Lightning Mapper (GLM). The black dot is the Mallard Fire.

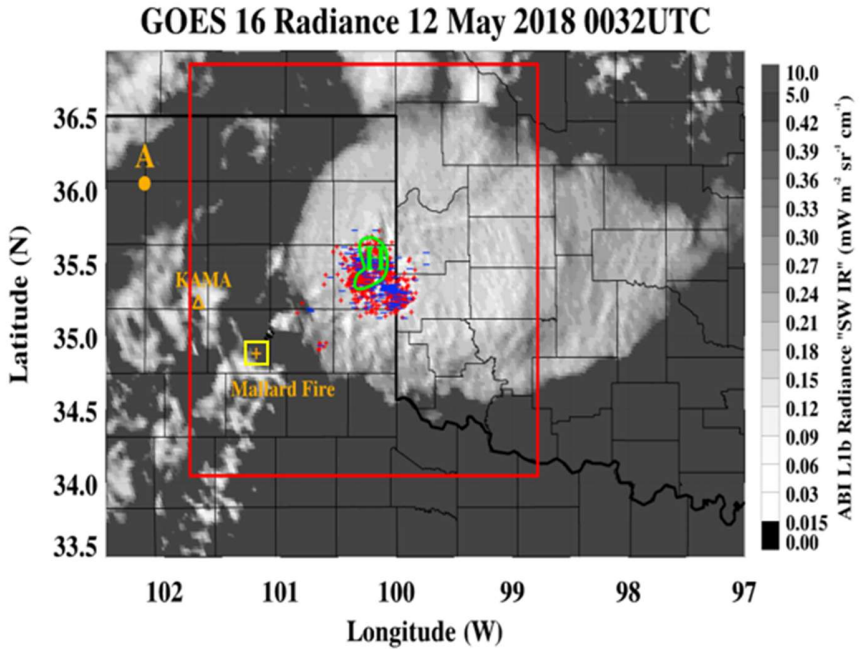

Figure 6.4 The pyroCb observed from GOES-16 Band 7 ("shortwave window" Infrared) and the lightning strokes (marked as "+") from the National Lightning Detection Network (NLDN) at 0032 UTC 12 May 2018, and the area of observed hail (green contour line) from the MESH data at 0030 UTC. The location of A is a site that was not influenced by wildfire and KAMA is a sounding site. The latitude and longitude ranges show the model simulation domain.

The fire burned area simulated in Wildfire (black box in Figure 6.5) on 11 May is ~300 km^2, which is similar to the burned area in WRF-Chem-SFIRE (black box in Figure 6.5b). The heat fluxes from the Mallard Fire averaged over the fire burned area during 1200-1800 UTC 11 May 2018 (several hours before the pyroCb) simulated by Wildfire have a range of 10-23 kW m^{-2} (Figure 6.5a) with a mean of ~18.7 kW m^{-2}, which is a slight underestimate of ~20.3 kW m^{-2}, the corresponding mean value from WRF-Chem-SFIRE (Figure 6.5b). Wildfire and WRF-Chem-SFIRE simulate similar temperature perturbations near the surface over the fire area and the downwind regions two hours before the pyroCb is initiated, which exceeds 5 ºC at Mallard (Figure 6.5a, b).

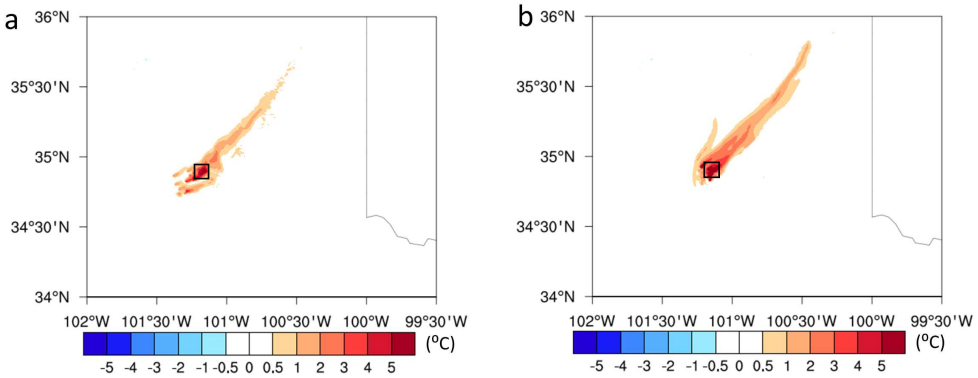

Figure 6.5 Temperature anomaly at 2-m altitude due to the Mallard Fire simulated by (a) Wildfire and (b) WRF-Chem-SFIRE by comparing with No_Wildfire at 1800 UTC on 11 May (2-hour before the initiation of convection). Black boxes denote the fire burned areas.

We also evaluate Wildfire and WRF-Chem-SFIRE with a sounding from the KAMA site. It is evident that the KAMA site was indeed influenced by a small fire near Amarillo (~7 km to the south; shown as a red dot adjacent to the white dot in Figure 6.6) on 10 May due to the southwesterly winds at low levels (Figure 6.6). Overall, Wildfire predicts the temperature and relative humidity that are consistent with the sounding data at 0000 UTC 11 May at KAMA (Figure 6.7). The results are very similar to those in WRF-Chem-SFIRE.

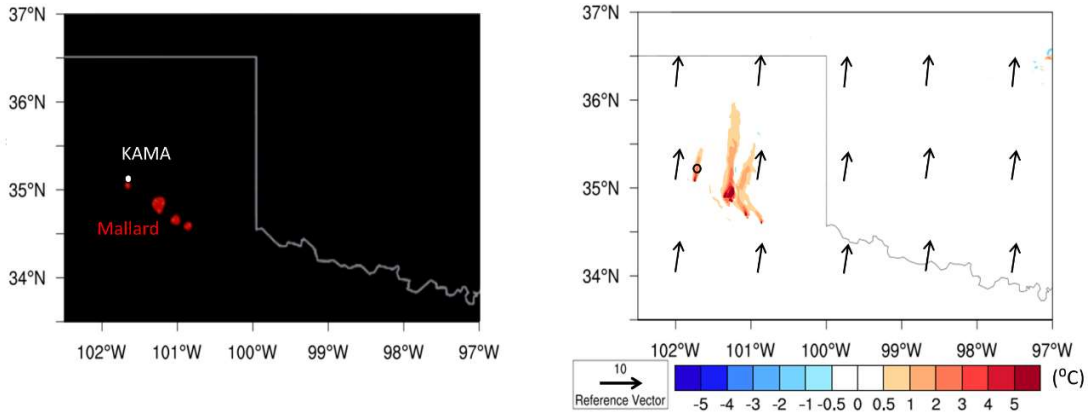

Figure 6.6 Fire location detected by MODIS Thermal Anomalies Product on 10 May (left). 2-m temperature anomaly (shaded) from No_Wildfire to Wildfire and 10-m wind (arrows) in Wildfire at 0000 UTC 11 May (right). KAMA sounding site is marked as circle.

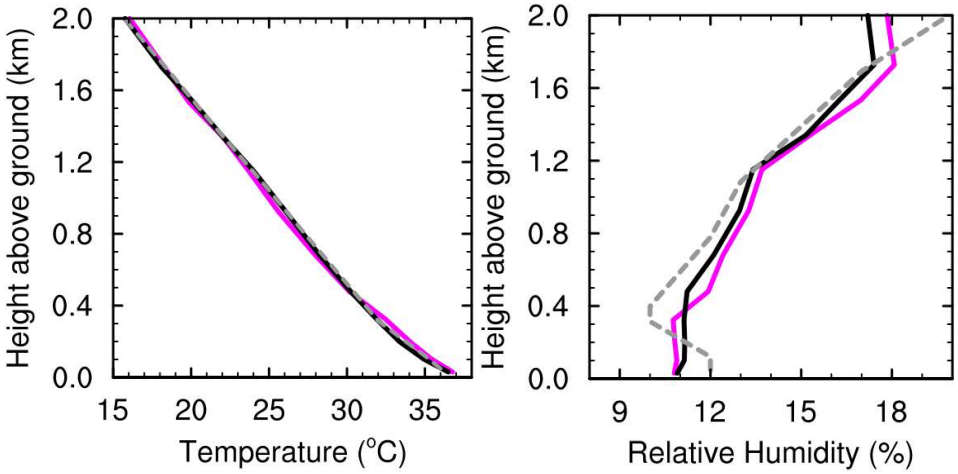

Figure 6.7 The profiles of temperature and relative humidity at 0000 UTC 11 May at KAMA from the sounding (grey dashed), Wildfire (black solid), and WRF-Chem-SFIRE (magenta solid).

Wildfire generally overestimates plume heights by 100-300 m (Figure 6.8), which is within the measurement uncertainty range of about ±500 m (Martin et al., 2018). WRF-Chem-SFIRE agrees with the observations slightly better. The 0 dBZ echo top height from Wildfire is very similar to WRF-Chem-SFIRE (Figure 6.9), with the maximum value occurring roughly one hour earlier and underestimated by ~1 km in comparison to the observations from NEXRAD. The computational cost of the WRF-Chem-SFIRE simulation is about 45% more than Wildfire. Those validations show that our new development can capture the heat effects from the fires in a similar way as the detailed fire simulation from SFIRE but more computationally efficient, which is more applicable to weather forecast and RGCMs.

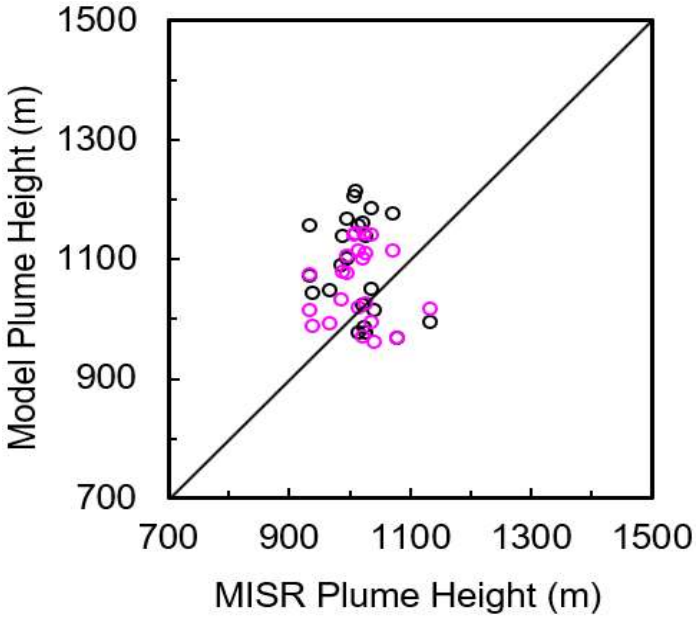

Figure 6.8 Comparison of plume heights among MISR, Wildfire (black circles), and WRF-Chem-SFIRE (magenta circles) during 1730-1800 UTC on 13 May.

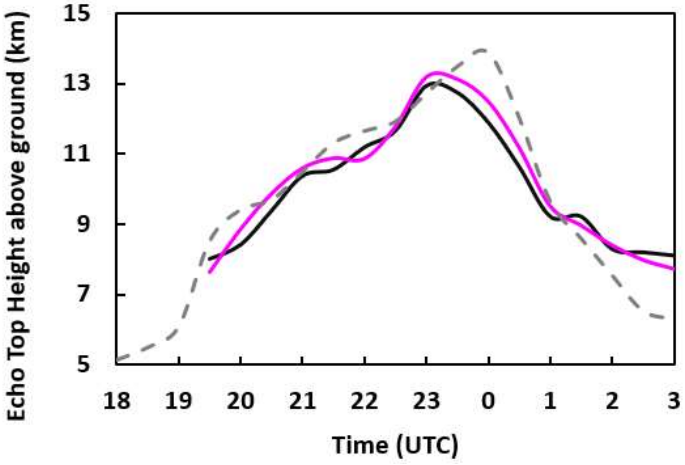

Figure 6.9 Comparison of radar echo top heights averaged over the red box in Figure 6.4 among the NEXRAD observation (grey dashed), Wildfire (black solid), and WRF-Chem-SFIRE (magenta solid). The echo top heights are defined with the threshold of reflectivity of 0 dBZ.

Note that the simulations for all above evaluations are driven by RAP reanalysis data, which assimilates various observational data, including radar, satellite, and radiosondes (Benjamin et al. 2016). Both the KAMA sounding and NEXRAD data were used for data assimilation in RAP, it is fair to say that part of the heat impact from the wildfires is already accounted for. This is a model dilemma: without being driven by reanalysis data, real-case model simulations can be unsuccessful. Therefore it is difficult to use observations to evaluate model fidelity. On the other hand, the use of the reanalysis data may lead to an underestimation of the heat effect. The underestimation of the heat effect will be further estimated in the last section.

Table 6.1 Description of the Experimental Design

Name	Description
Wildfire	The baseline run with the heat fluxes and aerosol emission from the wildfire
No_Heat	Turn off the heat fluxes from the wildfire
No_Aerosol	Turn off the aerosol emission from the wildfire
No_Wildfire	Without both heat fluxes and aerosol emission from the wildfire
No_PBLheat	Based on No_Heat except the upward sensible heat flux from PBL is disabled

We then apply the WRF-Chem with the new plume model to study the impact of wildfire on the pyroCb. We mainly consider the effects of heat and aerosol emissions from the wildfire since water vapor was found to contribute little to the intensity of convection (Trentmann et al. 2006; Lee et al. 2018a). In addition to Wildfire and No_Wildfire simulations, we conduct the following sensitivity tests: (a) No_Heat; in which the heat fluxes from the wildfire is turned off based on Wildfire, (b) No_Aerosol; in which the aerosol emission from the wildfire is turned off based on Wildfire, and (c) No_PBLheat; which is based on No_Heat except the upward sensible heat flux from planetary boundary layer (PBL) is disabled. The descriptions of these experiments are listed in Table 6.1. The maximum hail sizes from the simulations are estimated using a physically-based hail forecasting model (HAILCAST), which is online coupled with WRF-Chem simulations (Adams-Selin and Ziegler, 2016). HAILCAST forecasts the maximum expected hail diameter at the surface using updraft and microphysical information produced by WRF-Chem. We incorporate the most updated HAILCAST version from WRF v4.0 (Adams-Selin et al., 2018) into the WRF-Chem V3.9.1 for this study. The prediction of lightning

activity from model simulations is estimated with the utilization of the lightning potential index (LPI) described in Yair et al. (2010).

6.3 Wildfire Impacts on PyroCb

Figure 6.10 shows that, in Wildfire, the near surface temperature over the Mallard fire area (no sounding data available) was high (~37.5 ºC) with a low relative humidity (~13.5%) two hours prior to convective initiation. Note the terrain height is about 1.1 km over the area. By comparing Wildfire with No_Wildfire, the wildfire contributes to the remarkable increase in temperature (~ 4 ºC at 0.4 km and ~5.5 ºC near the surface; Figure 6.10) and the decrease in relative humidity (from 18% to 13.5% near surface; Figure 6.10). As expected, the temperatures are similar among different simulations at site A (Figure 6.4) where there is not much of a wildfire influence (Figure 6.11). The heat effect warms the lower atmosphere substantially (~4.5 ºC near the surface; Figure 6.10). However, the aerosol effect only slightly warms the atmosphere (~ 1ºC near the surface), as a result of absorbing radiation by smoke aerosols. Note that the difference in relative humidity is mainly due to the change in temperature since the water vapor mixing ratio does not differ much between the simulations.

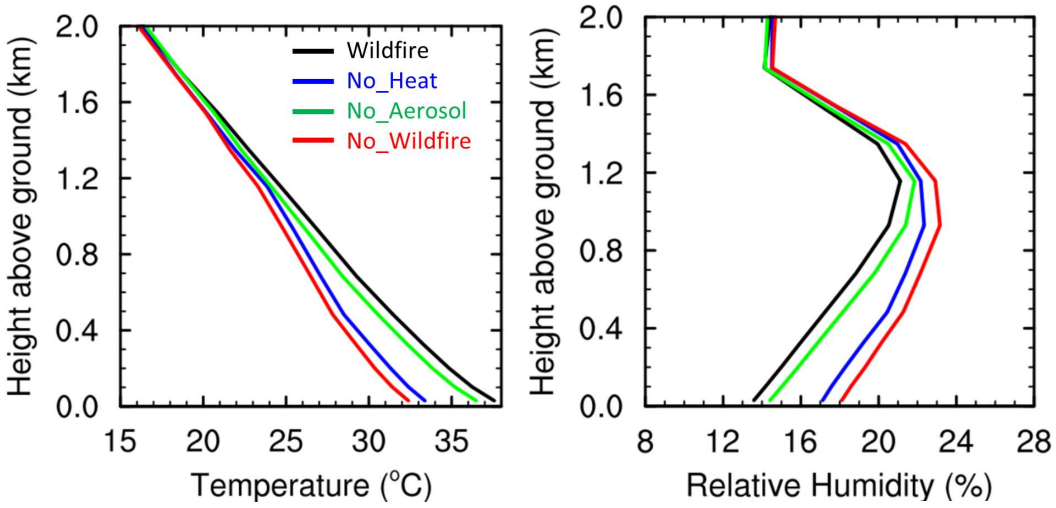

Figure 6.10 Temperature and relative humidity profiles at 1800 UTC 11 May at the Mallard fire area (yellow box in Figure 6.4) from Wildfire (black), No_Heat (blue), No_Aerosol (green), and No_Wildfire (red).

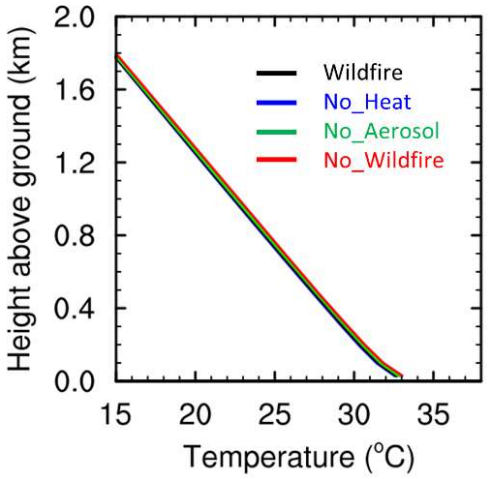

Figure 6.11 Profile of temperature at 0000 UTC 11 May at the site A from the simulations.

The impacts of the Mallard wildfire on precipitation, hail, and lightning are shown in Figures 6.12 - 6.14). Changes from Wildfire to No_Wildfire include the decrease in convective rain rates (>15 mm h^{-1}), extreme hailstone sizes (>20 mm), and very high reflectivity (>55 dBZ) (Figure 6.12). The lightning stroke rates are reduced by ~40%. These results suggest the wildfires substantially increase the severity of the convective

storm. In fact, the convective intensity is markedly enhanced when the full effects of the wildfire are considered (Figure 6.16a). The Wildfire simulation reproduces well the 6-h accumulated precipitation as observed from 2000 UTC 11 May to 0200 UTC 12 May (Figure 6.13a-b), except for a northwestward shift of the location of heavy rain. The hourly precipitation rate in Wildfire has the highest occurrence probability in the range of 15-20 mm h^{-1}, which also shows the best agreement with the observations (Figure 6.12a). Without considering the wildfire impacts, No_Widlfire underestimates the accumulated precipitation by ~30% (Figures 6.13b vs. 6.13e) and the heavy rain rates do not occur (Figure 6.12a).

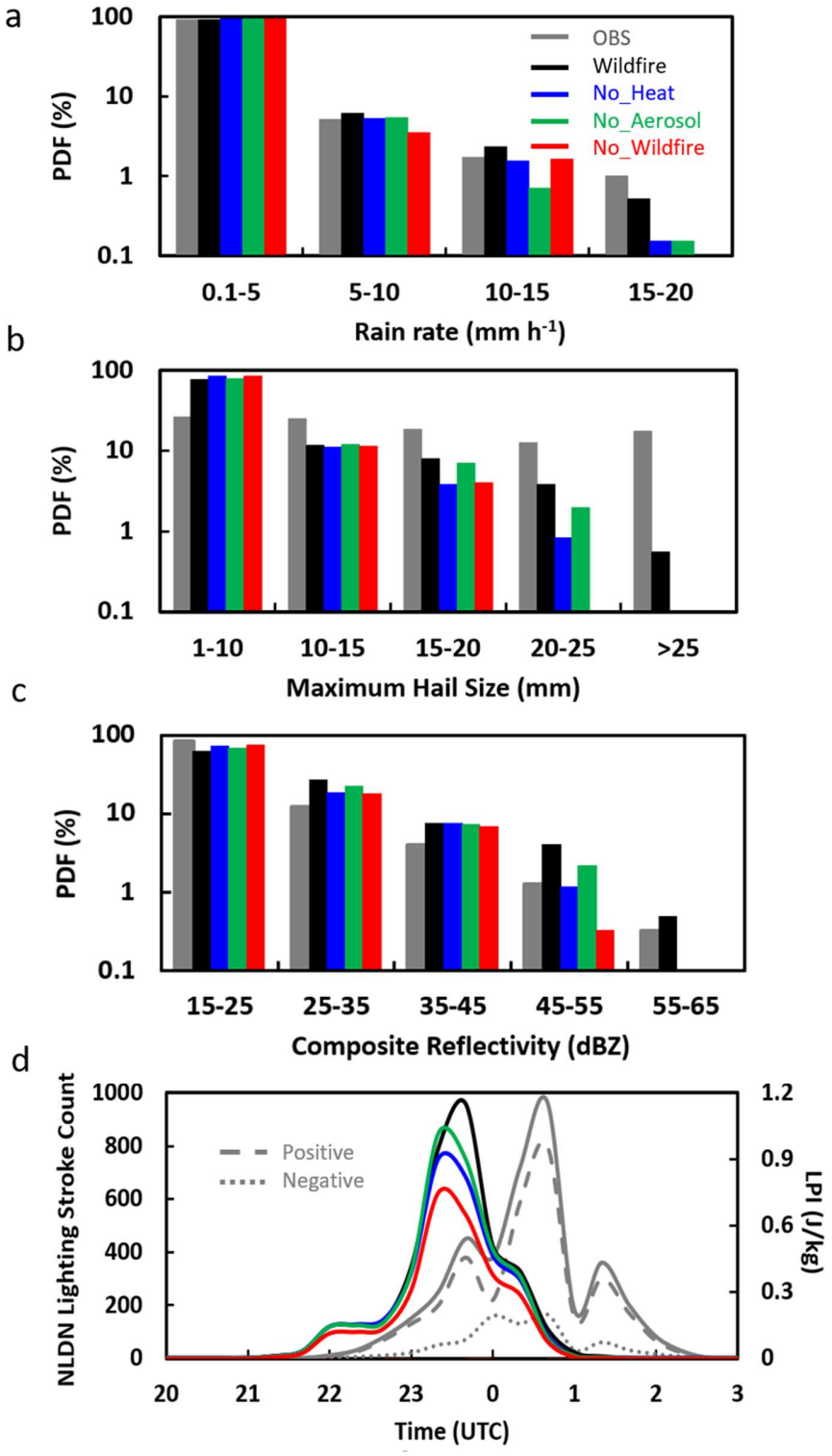

Figure 6.12 Probability density functions (PDFs) of (a) rain rates (>0.1 mm), (b) maximum hail size (>1 mm) and (c) composite reflectivity (>15 dBZ) from 2000 UTC 11 May to 0200 UTC 12 May when the proCb occurs. The value in the parentheses is the threshold

applied to the data for the PDF calculation. (d) Time series of total lightning stroke count per 5 min (IC + CG; grey solid) from NLDN (grey dashed for the total (IC + CG) positive lightning and grey dotted for the total negative lightning) and the LPI from the simulations. The observed maximum hail size is from the MESH data. The analysis domain is the red box marked in Figure 6.4.

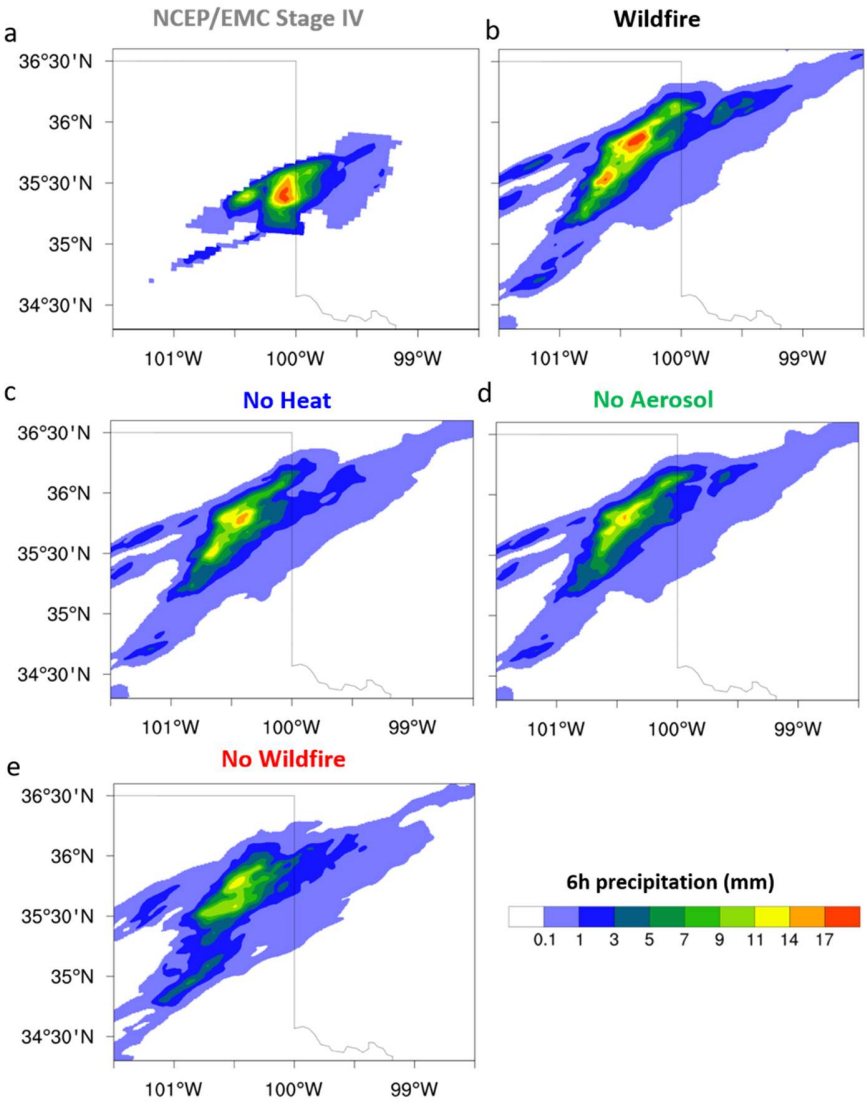

Figure 6.13 Accumulated precipitation from (a) NCEP/EMC Stage IV data, (b) Wildfire, (c) No_Heat, (d) No_Aerosol, and (e) No_Wildfire over a 6-h time period from 2000 UTC 11 May to 0200 UTC 12 May.

The simulated composite reflectivities (i.e., the column maximum) are up to 55-65 dBZ, which are consistent with the presence of hail, and agree with NEXRAD (GridRad; Homeyer and Bowman, 2017). In addition, Wildfire captures a similar region for hail occurrence as observed from both SPC reports and MESH (Figure 6.14a-b) and simulate the largest hail size of ~26 mm, which is in agreement with the reported 25.4 mm from the SPC report but ~10 mm smaller than that from the radar-retrieved MESH. The MESH data used in this study are developed from a newly-improved algorithm (Murillo and Homeyer, 2019), and generally has an uncertainty of ±7 mm. Without considering the wildfire impacts, the hail region shrinks, and the maximum hail size decreases to 18 mm (Figure 6.14b vs. 6.14e).

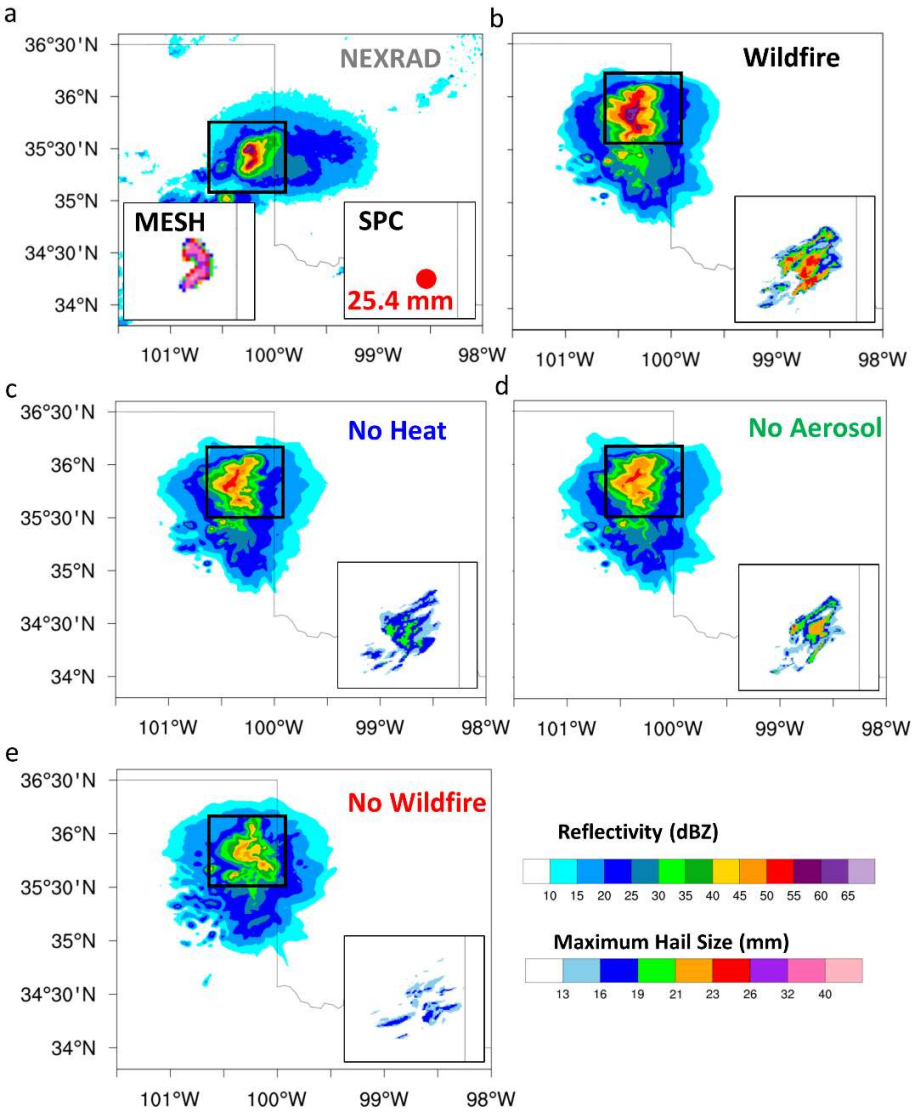

Figure 6.14 Composite reflectivity at the time when the maximum reflectivity is reached in temporal evolution from (a) NEXRAD at 0015 UTC 12 May, (b) Wildfire, (c) No_Heat, (d) No_Aerosol, (e) No_Wildfire at 2330 UTC 11 May. The corresponding maximum hail size is shown in the bottom-embedded small boxes for the black box region marked on the reflectivity plot. Both the SPC report and MESH data are shown on (a). The modeled results are from the HAILCAST estimation.

The observation shows the lightning stroke rate maximum of ~200 Strokes min^{-1} where most of those strokes are positive, Intra-Cloud (IC) pulses (compare Figure 6.12d with Figure 6.15). On the other hand, the Cloud-to-Ground (CG) strokerate is much lower

than IC especially for positive CG strokes (<2 s min^{-1}) (Figure 6.15), which suggests an absence of the dynamic forcing needed to produce the high positive CG stroke rates typically observed in polluted deep convective clouds (Lyons et al., 1998; Rosenfeld et al., 2007; Wang and Zhang 2009; Logan, 2018). The modeled LPI from Wildfire peaks about one hour ahead of the observed peak that is at 0030 UTC 12 May in lightning strokes (Figure 6.12d). Without the wildfire effect, LPI is drastically reduced by ~40%.

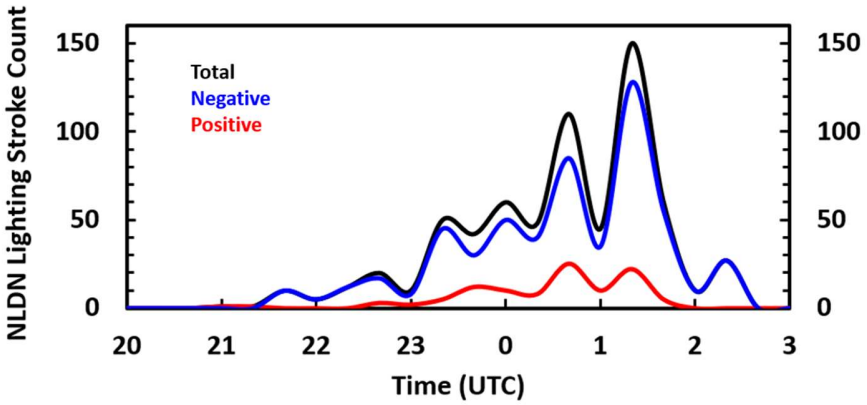

Figure 6.15 Time series of CG lightning stroke count per 5 min from NLDN for the Mallard pyroCb (red for the positive lightning; blue for the negative lightning, and black for total lightning). CG are all strokes with all positive CG lightning greater than or equal to 15 kA.

Both No_Heat and No_Aerosol underestimate the 6-hour total precipitation by ~3 mm and the frequency of rain rates larger than 10 mm h^{-1} (Figures 6.13c, d, and 6.12a). The relative significance of the heat effect on precipitation is similar to the aerosol effect. Both the sensible heat and aerosol effects of the wildfire contribute to higher reflectivity, larger hail size, and higher lightning potential. However, the sensible heat impact is more evident. The frequency of high reflectivity (>45 dBZ) is ~4% in No_Aerosol and ~1% in No_Heat (Figure 6.12c). The maximum hail size decreases by ~4 mm when neglecting the

aerosol effect and by ~6 mm when neglecting the heat effect (Figure 6.14). The LPI maximum is reduced by ~25% in No_Heat and ~15% in No_Aerosol (Figure 6.12d). Taking the two factors into account, the maximum hail size decreases by ~8 mm from Wildfire to No_Wildfire simulation. The mutual effect of heat and aerosols from wildfires on hail size is less than the sum of the respective effect from both factors, indicating a nonlinear damping effect on the hail size when the two factors work together.

We now explain how the wildfire enhances convective extremes (larger precipitation and reflectivity, extreme hailstone size, and more lightning). As shown in Figure 6.16, the wildfire markedly invigorates convection (Figure 6.16a), which can be explained by the increased thermal buoyancy from the sub-cloud to cloud regime (Figure 6.16b). Note that there is an appreciable sub-cloud vertical velocity (below 3 km) in Wildfire and No_aerosol, about 4-6 times larger compared with No_Heat and No_Widlfire, which is consistent with large sub-cloud vertical velocity in a developing pyroCb plume observed in Clements et al. (2018). This large sub-cloud vertical velocity appears before and at the initial stage of the pyroCb storm (Figure 6.17), a result of the sensible heating due to the heat released from wildfires. At the high-levels after storm is initiated, latent heating because of cloud microphysics is another reason for the increased thermal buoyancy in Wildfire compared with No_Wildfire. We find that the two major microphysical processes that dominate the latent heating are condensation and riming as shown in Figure 6.16c-d, respectively. The wildfire leads to an increase in latent heating by ~4 K h^{-1} through condensation and ~6 K h^{-1} through riming. After 2130 UTC as storm develops deeper, the effect of latent heating can be seen therefore the role of aerosol effect is shown clearly (Figure 6.17). Overall during the strong precipitation and lightning period

from 2300 UTC 11 May to 0000 UTC 12 May, the respective heat effect leads to ~25% increase in the vertical maximum of the averaged profile of top 25 percentiles of updraft speeds, while the aerosol effect leads to ~15% increase. By comparing with the ~50% enhancement due to the combined effect, the mutual effects of heat and aerosol from the wildfire have a nonlinear amplification effects on convective intensity.

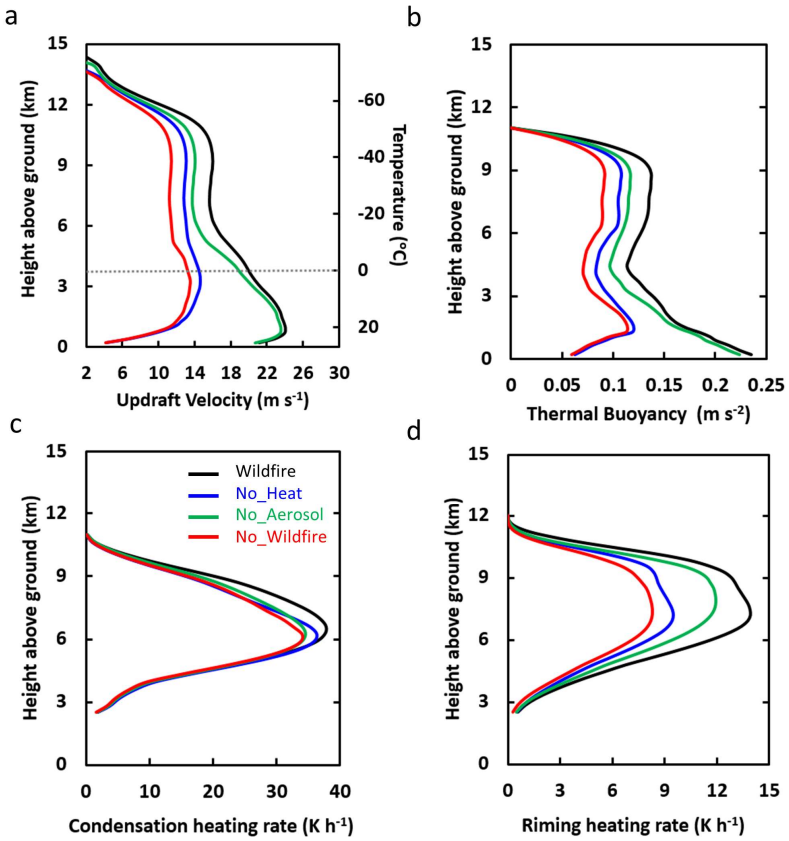

Figure 6.16 Vertical profiles of (a) updraft velocity, (b) thermal buoyancy, (c) condensation heating rate, and (d) riming heating rate averaged over the top 25 percentiles (i.e., 75th to 100th) of the updrafts with w>2 m s^{-1} from the simulations during the convection period from 2000 UTC 11 May to 0000 UTC 12 May over the analysis domain as shown in the red box in Figure 6.4. The dotted line in (a) denotes the freezing level (0 ^{o}C).

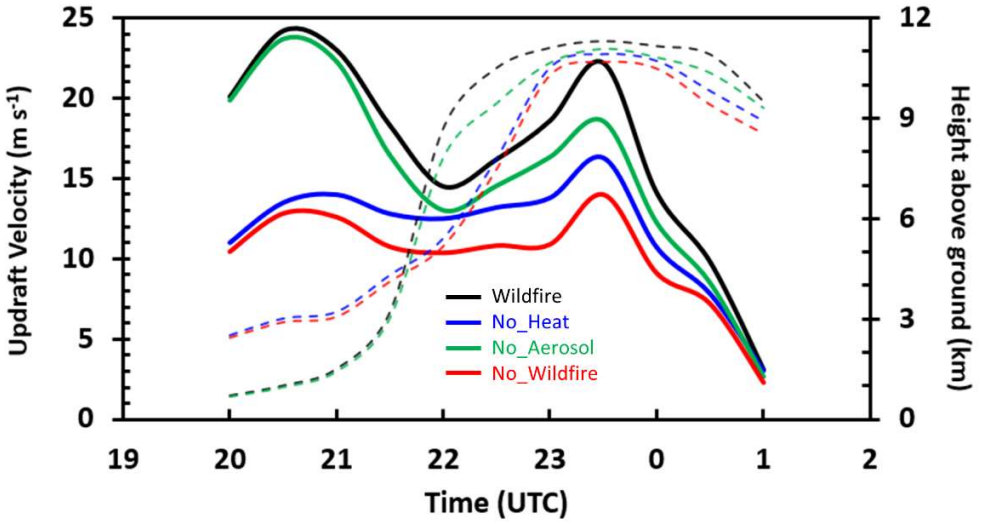

Figure 6.17 Time series of vertical maximum of updraft velocities (solid lines) and the corresponding altitudes above ground (dashed lines) of the averaged top 25 percentile updraft profiles for w >2 m s^{-1} over the analysis domain as shown in the red box in Figure 6.4 from the simulation Wildfire (black), No_Heat (blue), No_Aerosol (green) and No_Wildfire (red).

The larger hail and cloud electrical activity are likely due to a larger amount of supercooled water content from No_Wildfire to Wildfire (~40%; Figure 6.18a). The droplet number concentrations are doubled from the cloud base that is at 3.5-4 km above the surface (Figure 6.19a). It is interesting to note that No_Aerosol even has higher supercooled cloud droplet number and mass mixing ratios compared with No_Heat above 8 km, despite a much smaller droplet number concentration at low levels as a result of lower aerosol number concentrations, indicating that the stronger updrafts in No_Aerosol (Figure 6.16a) lift more cloud droplets to high levels. This shows the important role of updraft intensity that is enhanced by the heat effect in producing supercooled water at high levels. Mainly through riming, more supercooled droplets participate in forming more ice, snow, and hail, thereby releasing a large amount of heat aloft (Figures 6.18c-e and 6.19c-

e). It is known that larger amount of supercooled water available for accretion at subfreezing temperatures boosts the hail growth rate in cloud updrafts (Ilotoviz et al., 2018). In addition, the stronger updrafts provide more time for sufficient growth of a hailstone in its favored growth region (Guo and Huang, 2002), ultimately leading to larger hail size. As a result, both hail mass and number are increased (by ~45% and ~27%, respectively) by the wildfire (Figures 6.18e, 6.19e), with the mean hail size increased by ~25% (Figure 6.18f).

Lightning forms from the non-inductive charge separation caused by collisions between ice particles in the presence of supercooled liquid water within strong updrafts (Takahashi and Miyawaki, 2002). In the absence of strong dynamic forcing (e.g., a front or outflow boundary) in this case, the sensible heat helps air parcel overcome the large amount of surface-based convective inhibition (SBCIN) (~220 J kg-1) by increasing the surface heat flux and updraft strength. The aerosols from wildfires further invigorate convection through enhanced latent heating from condensation and riming as shown in Figure 6.16c-d (Fan et al., 2018; Rosenfeld et al., 2008). In addition, the aerosols increase supercooled droplets evidently. Therefore, the combination of sensible heat flux and aerosol loading contribute to the overall enhanced electrical activity of the pyroCb from No_Wildfire to Wildfire. Compared with the aerosol effect, the heat effect from wildfire contributes more significantly to developing larger hail size and more lightning, mainly because stronger convective intensity and the stronger updrafts lifts more liquid condensate to higher levels.

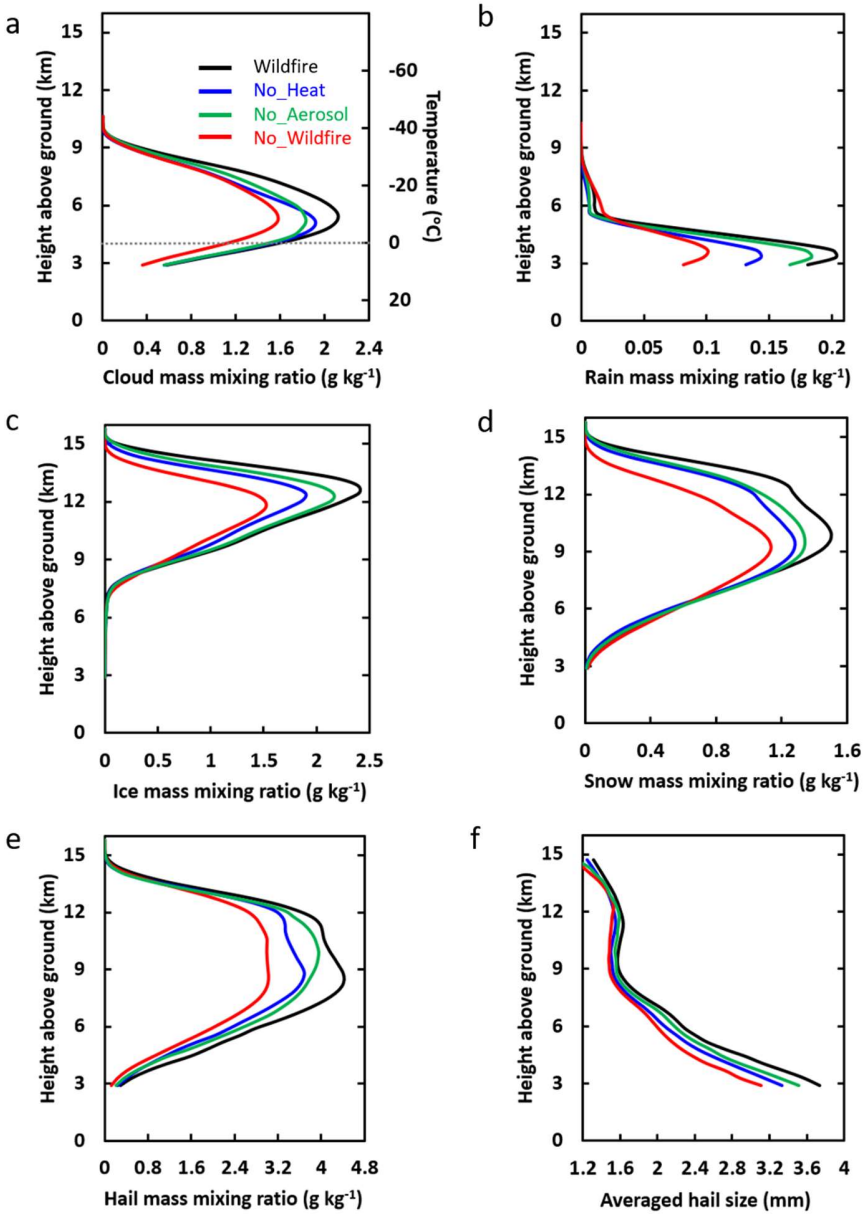

Figure 6.18 Vertical profiles of mass mixing ratios for (a) cloud, (b) rain, (c) ice, (d) snow, and (e) hail; and mean hail size for (f) hail averaged over the top 25 percentiles (i.e., 75th to 100th) of the updrafts with w>2 m s^{-1} from the simulations during the strong precipitation and lightning period from 2300 UTC 11 May to 0000 UTC 12 May over the analysis domain as shown in the red box in Figure 6.4. The dotted line in (a) denotes the freezing level (0°C).

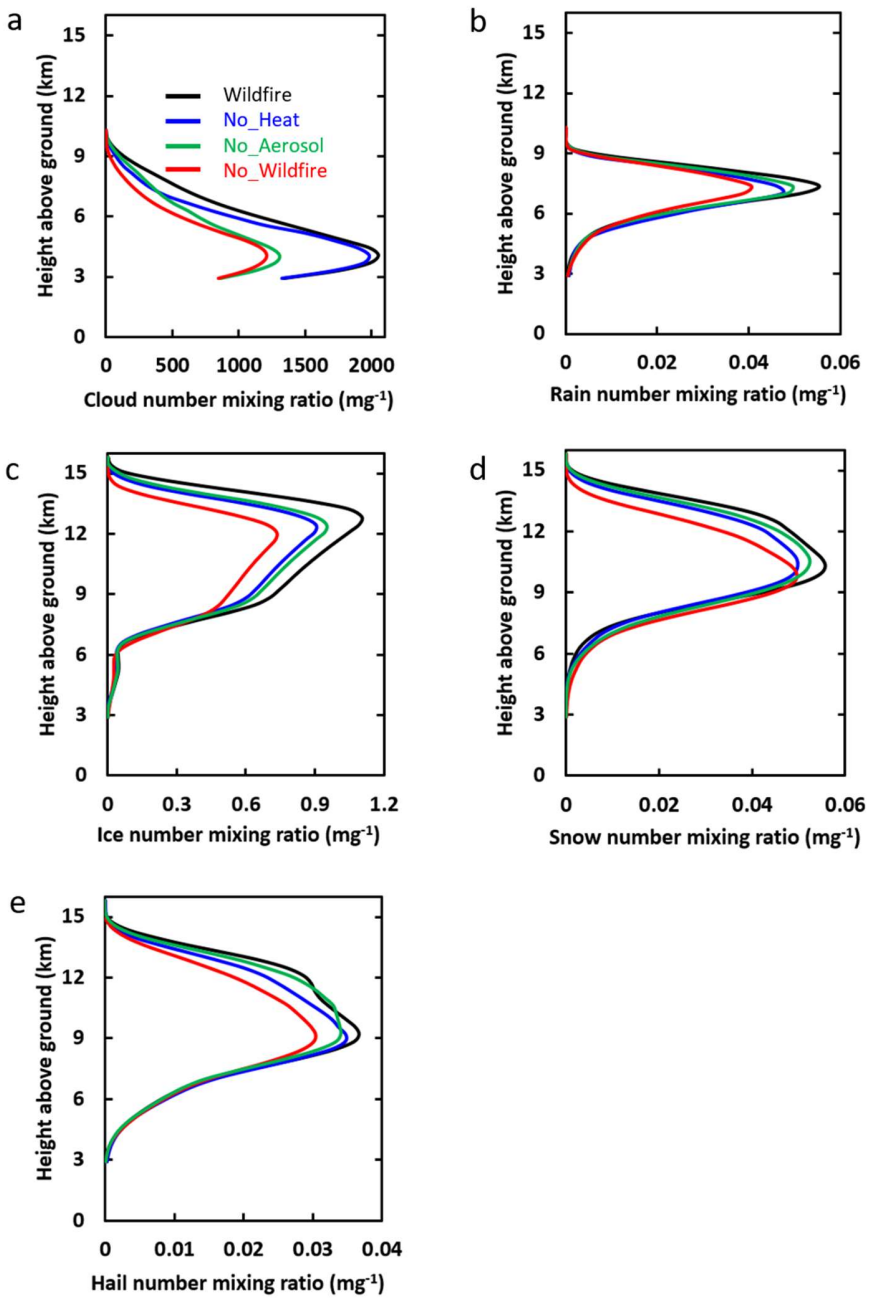

Figure 6.19 Vertical profiles of number mixing ratios for (a) cloud, (b) rain, (c) ice, (d) snow, and (f) hail averaged over the top 25 percentiles (i.e., 75th to 100th) of the updrafts with w>2 m s^{-1} from the simulations of Wildfire (black), No_Heat (blue), No_Aerosol (green), and No_Wildfire (red) during the strong convection period from 2300 UTC 11 May to 0000 UTC 12 May over the analysis domain as shown in the red box in Figure 6.4.

6.4 Conclusions and Discussion

We have developed a computationally efficient model capability to account for heat flux from wildfires in the WRF-Chem model. Using a combination of observations and a detailed fire module (i.e., SFIRE) for evaluation, the new model improves the simulation of temperature profiles at low-levels and simulates the fire-related properties (e.g., burned area, heat fluxes, plume height) consistent with the explicit fire simulations that requires approximately 45% more computation time than our new model simulation in the test case. This indicates a practical application of our new model development to weather and climate models to account for the impact of heat fluxes released from wildfires on atmospheric thermodynamics. We applied the new model to explore the impacts of the Mallard wildfire on the severity of a rare mesocyclonic pyroCb event occurring in Texas and Oklahoma on 11-12 May 2018, which is unique in the North American inventory of pyroCb and explored the total and individual contributions by heat flux and aerosol emissions from the wildfire event to the pyroCb properties.

The simulation accounting for both sensible heat flux and aerosol emissions from the wildfire reproduces reflectivity, precipitation, maximum hail size, and lightning, showing better agreements with observations than the simulations that do not account for either heat or aerosol emissions. Both heat and aerosols emitted from the wildfire increase low-level temperatures and enhance frequencies of extreme precipitation rate (>15 mm h^{-1}), high reflectivity (>55 dBZ), large hailstone size (>20 mm), and lightning potential. Even with a background meteorology where part of heat effect is already accounted for, the heat effect is more significant than the aerosol effect in enlarging maximum hail size by ~2 mm more and enhancing lightning potential by ~10%. We do see a role of aerosols in enhancing

convective intensity (through increased latent heat release by condensation and riming) and the frequency of heavy precipitation rates. The effect of the wildfire on convective intensity is remarkable (a 50% increase in the mean of top 25 percentiles of updraft speed during the strong precipitation and lightning period), which is solely contributed by the added heat from the wildfire at the initial stage of the storm with a noticeable role of aerosol in increasing latent heating as storm developing. The intensified updrafts lift more liquid condensate to higher levels and produce a larger amount of supercooled water, enhancing hail growth and resulting in larger hailstones. The larger ice particles in the presence of more supercooled liquid within stronger updraft can enhance positive lightning, which may explain the large portion of positive IC lightning stroke rate in the observations, but not necessarily the positive CG lightning stroke rate that is typically observed in polluted deep convective clouds. It is interesting to note that when the two factors are considered together, there is a nonlinear amplification effect on the intensity of convection compared with their respective singular effects, but a nonlinear damping effect on hail size. The nonlinear amplification effect on convective intensity suggests that aerosol invigoration through enhancing latent heat release may be more significant for stronger storms compared with weaker ones.

Although we demonstrate that the heat effect from the wildfire contributes significantly to pyroCb formation, intensity, and consequently severe weather (i.e., hail and lightning), the heat effect is still underestimated in our simulations because the initial and boundary meteorological conditions from RAP have accounted for heat impact due to the assimilation of the KAMA sounding and NEXRAD radar data in RAP. This is also evidenced from the fact that convection still occurs in No_Wildfire. Based on the sounding

at KAMA at 1200 UTC 11 May (about 8 hours before the initiation of convection), there is a stout capping inversion with no CAPE along with positive value for the lifted index (LI), suggesting the environment was not conducive to convection in the morning (Figure 6.20). In the afternoon, the environment could become less adverse to convection but unfortunately there is no sounding data to validate it. To corroborate the key role of the heat flux in triggering the convection, we have conducted another sensitivity test No_PBLheat based on No_Heat by removing the PBL heat tendency. This is to completely exclude the heat effect from the surface and PBL. No pyroCb occurs in this simulation and the temperatures below 300 m is about ~1.5-2 ºC lower compared with No_Wildfire (Figure 6.20b-c). This suggests the heat impact on the environmental temperature could be underestimated by up to ~1.5-2 ºC.

It should be noted that in our development of the model, the heat is added as a source term impacting grid-scale temperature, similar to the treatment in WRF-SFIRE. Whether the added capability can trigger pyroCb or not depends on host model resolution and atmospheric conditions. In this study, with 1-km grid spacing and an environmental temperature close to the convective temperature, the pyroCb is triggered and is well simulated.

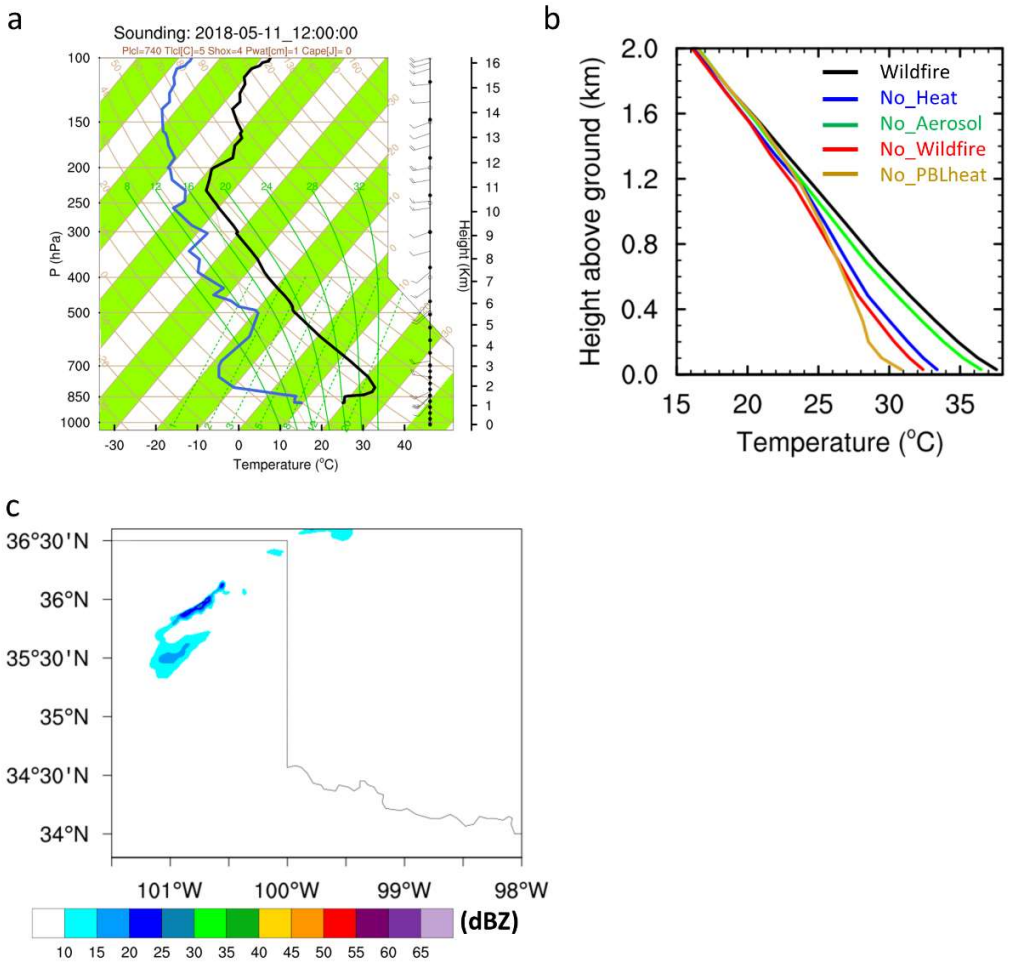

Figure 6.20 (a) The skew-T plot for the sounding at KAMA at 1200 UTC 11 May (~8 hours before the initiation of convection). (b) Temperature profiles of Wildfire (black), No_Heat (blue), No_Aerosol (green), No_Wildfire (red), and No_PBLheat (gold) at 1800 UTC (2-hour before the initiation of convection) 11 May at the Mallard fire region (yellow box in Figure 6.4). (c) Composite reflectivity from No_PBLheat at 2330 UTC when the maximum reflectivity is reached.

Chapter 7. Summary and Future Work

7.1 Summary

This study aims to gain a better understanding of how aerosol effect affects convective cloud under the context of urbanization and wildfires, both of which have been increasing and changed land, sensible heat and aerosols. Firstly, we examine how aerosols particularly the numerous ultrafine aerosol particles from mega-cities in the Amazon warm and humid regions affect convective intensity and precipitation (Chapter 3). Secondly, we investigate how aerosols and land surface change as a result of urbanization jointly and separately affect convective development and precipitation in Houston region (Chapter 4-5). Finally, we explore the influences of wildfires on environmental thermodynamics and the subsequent severe storm properties by developing a model capability that can computationally efficiently account for the impact of sensible heat fluxes from wildfires (Chapter 6). More detailed conclusions are organized below.

Aerosol-cloud interactions remain the largest uncertainty in climate projections. We use the retrieved updraft velocity from RWP to directly examine and help constrain aerosol impacts on updraft intensity, revealing the potentially substantial convective updraft and precipitation enhancements by $UAP_{<50}$ from the Manaus pollution plume. Real-case 3-D simulations show the observed convective updraft and precipitation enhancements by $UAP_{<50}$ over the Amazon region. The physical mechanism for such strong intensification of convection stems from the strong capacity of these DCCs in activating $UAP_{<50}$ that usually have a much higher number concentration than $CCN_{>50}$ particles. Note that the fast droplet coalescence in pristine conditions removes integrated droplet surface area for condensational growth, leaving a highly supersaturated condition.

The subsequent condensational growth of an additional number of droplets considerably lowers the water supersaturation, liberating a large amount of additional latent heat at the low and middle levels of DCCs and considerably enhancing updraft strength. This "warm-phase invigoration" is demonstrated to have much stronger effects than the "cold-phase invigoration" previously proposed and does not affect the timing of precipitation.

Urbanization could impact storm properties through changing urban land-cover and anthropogenic aerosols associated with industrial and population growth. We conduct ensemble WRF-Chem simulations coupled with SBM at 0.5 km grid spacing to simulate a thunderstorm occurring on 19 June 2013 and sensitivity tests to examine how urban land and anthropogenic aerosols over Houston impact the convective intensity and precipitation. We find that urbanization in Houston drastically enhances convective intensity and precipitation, primarily due to the urban aerosol effects. The aerosol enhances the convection through both "warm-phase invigoration" and "ice-phase invigoration", and the former is more significant. The effect of the urbanization on convective intensity is contributed by the land heat effect with an increasing significant role of aerosol in increasing latent heating through microphysical processes. Urban land effect does not change precipitation much. but initiates mixed-phase regime 20 min earlier due to urban heating. Urban aerosols fasten the development of convective cell into ice phase clouds, resulting from larger latent heat release. We also evaluate the performance of WRF-Chem coupled with SBM in simulating deep convective clouds and aerosol-cloud interaction by comparing with the Morrison microphysics. WRF-Chem-SBM shows the improvement in simulating the convection and precipitation and also the aerosol effect on deep convective clouds. With the two-moment bulk microphysics, model does not show a significant

aerosol impacts on convective intensity and precipitation, due to limitations in representation of aerosol-cloud interaction processes particularly drop condensation.

Wildfires, which have been increasing globally in frequency, burn season length, and burned area, could influence severe convective storms through releasing heat and aerosols into the atmosphere. We develop a computationally efficient model capability to account for heat flux from wildfires in the WRF-Chem model. Using a combination of observations and a detailed fire module (i.e., SFIRE) for evaluation, the new model improves the simulation of temperature profiles at low-levels and simulates the fire-related properties (e.g., burned area, heat fluxes, plume height) consistent with the explicit fire simulations that requires approximately 45% more computation time than our new model. We applied the new model to explore the impacts of the Mallard wildfire on the severity of a pyroCb event occurring in Texas and Oklahoma on 11-12 May 2018 and explored the total and individual contributions by heat flux and aerosol emissions from the wildfire event to the pyroCb properties. The simulation accounting for both sensible heat flux and aerosol emissions from the wildfire reproduces reflectivity, precipitation, maximum hail size, and lightning, showing better agreements with observations than the simulations that do not account for either heat or aerosol emissions. Both heat and aerosol effects increase low-level temperatures and mid-level buoyancy and enhance convective intensity. Intensified convection along with more supercooled liquid condensate at high altitudes due to stronger vertical transport, results in larger hailstones and enhanced lightning. The effects of heat flux on the convective extremes are more significant than those of aerosol emissions.

7.2 Future work

Urbanization may impact storm initiation, intensity, and spatial distribution through modifying land-surface conditions and increasing aerosols (Haberlie et al. 2015; Niyogi et al. 2011; Shepherd et al. 2002). The Houston case discussed in Chapter 4-5 is one scenario that urbanization enhances the storm intensity but does not affect the convection initiation and location much. The urban land effect primarily stemmed from the increased temperature due to urban heating. We will select other cases that the storms initiated over the urban areas and the initiation or location are affected to examine the urban land effect through a combination of increased temperature and mechanical turbulence resulting from complex urban surface geometry and roughness. Another category of the cases that initiated over non-urban areas but intensified over the urban areas will further be analyzed to study the impacts of urbanization on storm development and propagation. After that, we will postulate more plausible mechanisms concerning the impact of urbanization under different storm initiating and propagating conditions. In addition, we will also investigate the long-term impact of urbanization.

Wildfires which have been occurring more frequently in response to climate warming are projected to increase in frequency and intensity more significantly in the future, especially in Western United States. The work in Chapter 5 is the application of our new model computational efficiently accounting for the impact of heat flux on thermodynamics from wildfires in WRF-Chem in simulating a local pyroCb induced by wildfire occurred in a small region. We will next employ this new model to simulate the impacts of wildfire over a large region (i.e., Western and Central US) on storm initiation and intensity (through changing the cold front and subtropical high). Wildfire may also

impact storms through long-range transported aerosols (Saide et al. 2015). We will further use the new model to study how wildfires from Central America and over the Rocky Mountains and the region further west impact the storms through transported smoke aerosols and the possible perturbation to the atmosphere circulation through wildfire-atmosphere interaction. The long-term impact of wildfire will also be discussed.

Both urbanization and wildfire impacts may be more and more important in the projection of future global warming. Some storms may be mutually impacted by the urbanization and wildfire. We will further examine the impacts of urbanization and wildfire and investigate the relative role of each.

Bibliography

Abdul-Razzak, H., and S. J. Ghan (2002), A parameterization of aerosol activation. 3. Sectional representation, *J. Geophys. Res*., 107(D3), 4026

Adams-Selin, R. D., and C. L. Ziegler, (2016), Forecasting hail using a one-dimensional hail growth model within WRF. *Mon. Wea. Rev.,* 144, 4919–4939, doi:10.1175/MWR-D-16-0027.1.

Albrecht B. Aerosols, 1989: cloud microphysics, and fractional cloudiness. *Science*, 245: 1227-1230.

Anderson T. L., et al., 2005: An "A-Train" strategy for quantifying direct climate forcing by anthropogenic aerosols. *Bull. Am. Meteor. Soc.*, 86, 1795–1809.

Andreae M. O., D. Rosenfeld, P. Artaxo, A. A. Costa, G. P. Frank, K. M. Longo, and M. A. Silva-Dias, 2004: Smoking rain clouds over the Amazon. *Science* 303, 1337-1342.

Andreae M. O., C. D. Jones, and P. M. Cox, 2005: Strong present-day aerosol cooling implies a hot future. *Nature*, 435, 1187–1190.

Andreae M. O., 2007: Aerosols before pollution, *Science*, 315, 50.

Andreae, M. O., Afchine, A., Albrecht, R., Holanda, B. A., Artaxo, P., Barbosa, H. M. J., Borrmann, S., Cecchini, M. A., et al. 2018: Aerosol characteristics and particle production in the upper troposphere over the Amazon Basin, Atmos. Chem. Phys., 18, 921-961.

Arakawa A., 1975: Modeling clouds and cloud processes for use in climate models. In: The Physical Basis of Climate and Climate Modelling. ICSU/WMO, GARP Publications Series N° 16, Geneva, Switzerland, pp. 181–197.

Arakawa A., 2004: The cumulus parameterization problem: Past, present, and future. *J. Clim.*, 17, 2493–2525.

Barnes H. C., and R. A. Houze Jr., 2016: Comparison of observed and simulated spatial patterns of ice microphysical processes in tropical oceanic mesoscale convective systems, *J. Geophys. Res. Atmos*. 121, 8269–8296.

Beck V., Gerbig, C., Koch, T., Bela, M. M., Longo, K. M., Freitas, S. R., Kaplan, J. O., Prigent, C., Bergamaschi, P., and Heimann, M. , 2013: WRF-Chem simulations in the Amazon region during wet and dry season transitions: evaluation of methane models and wetland inundation maps, *Atmos. Chem. Phys.*, 13, 7961-7982.

Benjamin, S. G., S. S. Weygandt, et al. 2016: A North American Hourly Assimilation and Model Forecast Cycle: The Rapid Refresh. *Mon. Wea. Rev.,* 144, 1669-1694.

Bornstein, R., and Q. Lin (2000), Urban heat islands and summertime convective thunderstorms in Atlanta: Three case studies, *Atmos. Environ.*, 34, 507–516.

Boucher O, Randall, D and Artaxo, P et al. Clouds and aerosols, in Climate Change 2013: The Physical Science Basis. Contribution of Working Group I to the Fifth Assessment Report of the Intergovernmental Panel on Climate Change, edited by T. Stocker, D. Qin, G.-K. Plattner, M. Tignor, S. Allen, J. Boschung, A. Nauels, Y. Xia, V. Bex, and P. Midgley, 2013; pp. 571–658, Cambridge University Press, Cambridge, United Kingdom and New York, NY, USA.

Briggs, G.A. (1975): Plume rise predictions. In Lectures on Air Pollution and Environmental Impact Analyses; Haugen, D.A., Ed.; American Meteorological Society: Boston, MA, USA, 1975; pp. 59–111

Carrió GG, WR Cotton, and WYY Cheng. 2010. "Urban Growth and Aerosol Effects on Convection over Houston." *Atmospheric Research*. 96(4). 560–574. DOI:10.1016/j.atmosres.2010.01.005

Cecchini M. A., L. A. T. Machado, J. M. Comstock, F. Mei, J. Wang, J. Fan, J. M. Tomlinson, B. Schmid, R.Albrecht, S. T. Martin, P. Artaxo, (2016), Impacts of the Manaus pollution plume on the microphysical properties of Amazonian warm-phase clouds in the wet season. Atmos. Chem. Phys. 16, 7029–7041.doi:10.5194/acp-16-7029-2016

Chapman, E. G., Gustafson Jr., W. I., Easter, R. C., Barnard, J. C., Ghan, S. J., Pekour, M. S., and Fast, J. D. (2009), Coupling aerosol-cloud-radiative processes in the WRF-Chem model: Investigating the radiative impact of elevated point sources, *Atmos. Chem. Phys.,* 9, 945-964, https://doi.org/10.5194/acp-9-945-2009.

Chen, F, and J. Dudhia (2001) Coupling an advanced land surface–hydrology model with the Penn State–NCAR MM5 modeling system. Part I: Model implementation and sensitivity. *Mon Weather Rev* 129(4):569–585.

Chen Y.-C., M. W. Christensen, L. Xue, A. Sorooshian, G. L. Stephens, R. M. Rasmussen, and J. H. Seinfeld, 2012: Occurrence of lower cloud albedo in ship tracks. *Atmos. Chem. Phys.*, 12, 8223–8235.

Clements, C.B.; Lareau, N.; Kingsmill, D.E.; Bowers, C.L.; Camacho, C.P.; Bagley, R.; Davis, B. (2018), RaDFIRE–The rapid deployments to wildfires experiment (RaDFIRE): Observations from the fire zone. *Bull. Am. Meteorol. Soc.* 99, 2539–2559.

Cruz, M. G., A. L. Sullivan, J. S. Gould, N. C. Sims, A. J. Bannister, J. J.Hollis, and R. J. Hurley, 2012: Anatomy of a catastrophic wildfire: The Black Saturday Kilmore East fire in Victoria, *Australia. For. Ecol. Manage.,* 284, 269–285.

Cummins, K. L., & Murphy, M. J. (2009). An overview of lightning locating systems: History, techniques, and data uses, with an in-depth look at the U.S. NLDN. *IEEE Transactions on Electromagnetic Compatibility*, 51(3), 499–518.

Dennison, P. E., S. C. Brewer, J. D. Arnold, and M. A. Moritz (2014), Large wildfire trends in the western United States, 1984–2011, *Geophys. Res. Lett.,* 41, 2928–2933, doi:10.1002/2014GL059576.

Ding A.J, Fu, CB and Yang, XQ et al., 2013: Intense atmospheric pollution modifies weather: a case of mixed biomass burning with fossil fuel combustion pollution in eastern China. *Atmos. Chem. Phys*, 13:10545-10554.

Ekman, A. M. L., A. Engström, and A. Söderberg, 2011: Impact of two way aerosol-cloud interaction and changes in aerosol size distribution on simulated aerosol-induced deep convective cloud sensitivity, *J. Atmos. Sci*., 68(4), 685–698.

Fan, J., R. Zhang, G. Li, and W.-K. Tao (2007), Effects of aerosols and relative humidity on cumulus clouds, *J. Geophys. Res.*, 112, D14204.

Fan, J., and Coauthors, 2009: Dominant role by vertical wind shear in regulating aerosol effects on deep convective clouds. *J. Geophys. Res.*, 114, D22206

Fan J., D. Rosenfeld, Y. Ding, L. R. Leung, and Z. Li, 2012: Potential aerosol indirect effects on atmospheric circulation and radiative forcing through deep convection. *Geophys. Res. Lett.,* 39, L09806.

Fan J., L. R. Leung, D. Rosenfeld, Q. Chen, Z. Li, J. Zhang, and H. Yan, 2013: Microphysical effects determine macrophysical response for aerosol impacts on deep convective clouds. *Proc. Natl. Acad. Sci.* USA, 110, E4581–E4590.

Fan J., D. Rosenfeld, Y. Yang, C. Zhao, L. R. Leung, and Z. Li, 2015: Substantial contribution of anthropogenic air pollution to catastrophic floods in Southwest China. *Geophys. Res. Lett.*, 42, 6066–6075.

Fan J., Y. Wang, D. Rosenfeld, and X. Liu, 2016: Review of Aerosol-Cloud Interactions: Mechanisms, Significance, and Challenges. *J. Atmos. Sci.*, 73, 4221-4252.

Fan J., D. Rosenfeld, Y. Zhang, S. Giangrande, Z. Li, L. Machado, and S.T. Martin, et al. (2018), Substantial Convection and Precipitation Enhancements by Ultrafine Aerosol Particles. *Science* 359, 6374:411-418. doi:10.1126/science.aan8461.

Fast J. D., Gustafson Jr., W. I., Easter, R. C., Zaveri, R. A., Barnard, J. C., Chapman, E. G., Grell, G. A., and Peckham, S. E., 2006: Evolution of ozone, particulates, and aerosol direct radiative forcing on the vicinity of Houston using a fully coupled meteorology-chemistry-aerosol model, *J. Geophys. Res*., 111, D21305.

Filippi, J. B., Bosseur, F., Pialat, X., Santoni, P., Strada, S., and Mari, C., (2011), Simulation of coupled fire/atmosphere interaction with the MesoNH-ForeFire models, J. Combust., 2011, 540390, doi:10.1155/2011/540390.

Freitas, S. R., Longo, K. M., and Andreae, M. O. (2006), Impact of including the plume rise of vegetation fires in numerical simulations of associated atmospheric pollutants, *Geophys. Res. Lett.,* 33, L17808, doi:10.1029/2006GL026608.

Freitas, S. R., Longo, K. M., Chatfield, R., Latham, D., Silva Dias, M. A. F., Andreae, M. O., Prins, E., Santos, J. C., Gielow, R., and Carvalho Jr., J. A. 2007: Including the

sub-grid scale plume rise of vegetation fires in low resolution atmospheric transport models, *Atmos. Chem. Phys*., 7, 3385-3398

Fromm, M. D., A. Tupper, D. Rosenfeld, R. Servranckx, and R. McRae, 2006: Violent pyro-convective storm devastates Australia's capital and pollutes the stratosphere. *Geophys. Res. Lett.,* 33, L05815.

Fromm, M. D., R. H. D. McRae, J. J. Sharples, and G. P. Kablick III, 2012: Pyrocumulonimbus pair in Wollemi and Blue Mountains National Parks, 22 November 2006. *Aust. Meteor. Oceanogr. J*., 62, 117–126.

Gao W., J. Fan, R.C. Easter, Q. Yang, C. Zhao and S.J. Ghan, 2016: Coupling spectral-bin cloud microphysics with the MOSAIC aerosol model in WRF-Chem: Methodology and results for marine stratocumulus clouds, *J. Adv. Model. Earth Syst.*, 8,1289-1309.

Gelaro, R, McCarty W, Suárez MJ, Todling R, Molod A, Takacs L, Randles CA, Darmenov A, Bosilovich MG, Reichle R, Wargan K, et al., (2017), The modern-era retrospective analysis for research and applications, version 2 (MERRA-2). *J. Clim.,* 30(14):5419–5454

Grell G.A., Peckham, S.E., Schmitz, R., McKeen, S.A., Frost, G., Skamarock, W.C., Eder, B., 2005: Fully coupled "online" chemistry within the WRF model. *Atmospheric Environment,* 39, 6957-6975.

Grell, G., Freitas, S. R., Stuefer, M., and Fast, J. (2011), Inclusion of biomass burning in WRF-Chem: impact of wildfires on weather forecasts, *Atmos. Chem. Phys.,* 11, 5289-5303, https://doi.org/10.5194/acp-11-5289-2011.

Guenther, A., T. Karl, P. Harley, C. Wiedinmyer, P. I. Palmer, C. Geron (2006), Estimates of global terrestrial isoprene emissions using MEGAN (Model of Emissions of Gases and Aerosols from Nature), *Atmos. Chem. Phys.,* 6, 3181-3210.

Guo, X. and M. Huang (2002), Hail formation and growth in a 3D cloud model with hail-bin microphysics, *Atmospheric Research,* 63, 59-99.

Haberlie AM, WS Ashley, and TJ Pingel. 2015. "The Effect of Urbanisation on the Climatology of Thunderstorm Initiation: Urbanisation and Thunderstorm Initiation." *Quarterly Journal of the Royal Meteorological Society*. 141(688). 663–675. DOI:10.1002/qj.2499.

Haywood J., and O. Boucher, 2000: Estimates of the direct and indirect radiative forcing due to tropospheric aerosols: A review. *Rev. Geophys.*, 38, 513–543.

Homeyer, C. R., and K. P. Bowman, (2017), Algorithm Description Document for Version 3.1 of the Three-Dimensional Gridded NEXRAD WSR-88D Radar (GridRad) Dataset. Available online at: http://gridrad.org/pdf/GridRad-v3.1-Algorithm-Description.pdf.

Hong, S-Y, Y. Noh, J. Dudhia (2006), A new vertical diffusion package with an explicit treatment of entrainment processes. *Mon Weather Rev* 134(9):2318–2341.

Houze R. A., Jr., 2014: *Cloud Dynamics* (Elsevier/Academic Press, Oxford, ed. 2), pp. 432.

Hubbart J, E Kellner, L Hooper, A Lupo, P Market, P Guinan, K Stephan, N Fox, and B Svoma. 2014. "Localized Climate and Surface Energy Flux Alterations across an

Urban Gradient in the Central U.S." *Energies*. 7(3). 1770–1791. DOI:10.3390/en7031770.

Iacono, M.J, et al. (2008), Radiative forcing by long-lived greenhouse gases: Calculations with the AER radiative transfer models. *J Geophys Res* 113(D13):D13103.

Ilotoviz. E, A. Khain, A. V. Ryzhkov and J. C. Snyder (2018), Relationship between Aerosols, Hail Microphysics, and Z_{DR} Columns, *Journal of the Atmospheric Sciences,* 75, 1755-1781.

Janjic, Zavisa I., 1994: The Step–Mountain Eta Coordinate Model: Further developments of the convection, viscous sublayer, and turbulence closure schemes. *Mon. Wea. Rev.*, **122**, 927–945.

Jungwirth, P., D. Rosenfeld, and V. Buch (2005), A possible new molecular mechanism of thundercloud electrification, *Atmospheric Research,* 76, 190–205.

Kablick, G. P., Fromm, M. D., Miller, S. D., Partain, P., Peterson, D., Lee, S. S., Y. Zhang, A. Lambert and Z. Li (2018), The Great Slave Lake pyroCb of 5 August 2014: Observations, simulations, comparisons with regular convection, and impact on UTLS water vapor. *Journal of Geophysical Research: Atmospheres*, 123, 12,332–12,352.

Kellner O, and D Niyogi. 2014. "Land Surface Heterogeneity Signature in Tornado Climatology? An Illustrative Analysis over Indiana, 1950–2012." *Earth Interactions*. 18(10). 1–32.

Khain, A. P., M. Ovtchinnikov, M. Pinsky,A. Pokrovsky, and H. Krugliak, 2000: Notes on the state-of-the-art numerical modeling of cloud microphysics, *Atmos. Res.,* 55, 159–224.

Khain A. P., A. Pokrovsky, M. Pinsky, A. Seifert, V. Phillips, 2004: Simulation of Effects of Atmospheric Aerosols on Deep Turbulent Convective Clouds Using a Spectral Microphysics Mixed-Phase Cumulus Cloud Model. Part I: Model Description and Possible Applications, *J. Atmos. Sci*. 61, 2963-2982.

Khain A. P., N. BenMoshe, and A. Pokrovsky, 2008: Factors determining the impact of aerosols on surface precipitation from clouds: An attempt at classification. *J. Atmos. Sci.*, 65, 1721–1748.

Khain, A. P., L. R. Leung, B. Lynn, and S. Ghan, 2009: Effects of aerosols on the dynamics and microphysics of squall lines simulated by spectral bin and bulk parameterization schemes, *J. Geophys. Res*., 114, D22203,

Khain A. P., V. Phillips, N. Benmoshe, A. Pokrovsky, 2012: The Role of Small Soluble Aerosols in the Microphysics of Deep Maritime Clouds, *J. Atmos. Sci.* 69, 2787-2807.

Kochanski, A. K., Beezley, J. D., Mandel, J., and Kim, M., (2012), WRF fire simulation coupled with a fuel moisture model and smoke transport by WRF-Chem, 13th WRF Users' Workshop, National Center for Atmospheric Research, 20–24 June 2012, arXiv:1208.1059.

Kochanski, A. K., Jenkins, M. A., Sun, R., Krueger, S., Abedi, S., and Charney, J., (2013), The importance of low-level environmental vertical wind shear to wildfire

propagation: Proof of concept, J. Geophys. Res.-Atmos., 118, 8238–8252, doi:10.1002/jgrd.50436.

Koren I., J. V. Martins, L. A. Remer, H. Afargan, 2008: Smoke invigoration versus inhibition of clouds over the Amazon, Science 321, 946-949.

Koren I., G. Dagan, and O. Altaratz, 2014: From aerosol-limited to invigoration of warm convective clouds. *Science*, 344, 1143– 1146, doi:10.1126/science.1252595.

Kulmala, M., Asmi, A., Lappalainen, H. K., Baltensperger, U., Brenguier, J.-L., Facchini, M. C., et al., 2011: General overview: European Integrated project on Aerosol Cloud Climate and Air Quality interactions (EUCAARI) – integrating aerosol research from nano to global scales, *Atmos. Chem. Phys.*, 11, 13061-13143.

Lareau, N. P. and Clements, C. B., (2016), Environmental controls on pyrocumulus and pyrocumulonimbus initiation and development, *Atmos. Chem. Phys.,* 16, 4005-4022, https://doi.org/10.5194/acp-16-4005-2016.

Lareau N.P., C.B. Clements, (2017), The mean and turbulent properties of a wildfire convective plume, *J. Appl. Meteorol. Climatol.*, 56 (8), 2289-2299.

Lareau, N.P.; Nauslar, N.J.; Abatzoglou, J.T., (2018), The Carr Fire Vortex: A Case of Pyro-tornadogenesis? *Geophys. Res. Lett.* 45, 13–107. doi.org/10.1029/2018GL080667.

Latham, D., (1994), PLUMP: A one-dimensional plume predictor and cloud model for fire and smoke managers, General Technical Report INT-GTR-314, Intermountain Research Station, USDA Forest Service, Nov 1994.

Lebo Z. J., H. Morrison, and J. H. Seinfeld, 2012: Are simulated aerosol-induced effects on deep convective clouds strongly dependent on saturation adjustment? *Atmos. Chem. Phys.*, 12, 9941–9964.

Lee, H., Jeong, S.-J., Kalashnikova, O.,Tosca, M., Kim, S.-W., & Kug, J.-S. (2018a), Characterization of wildfire-induced aerosol emissions from the Maritime Continent peatland and Central African dry savannah with MISR and CALIPSO aerosol products. *Journal of Geophysical Research: Atmospheres,* 123, 3116–3125.

Lee. S. S., J. Penner, and S. Saleeby, 2009: Aerosol effects on liquid-water path of thin stratocumulus clouds, *Geophys Res Atmos,* 14, D07204.

Lee S. S., 2012: Effect of aerosol on circulations and precipitation in deep convective clouds. *J. Atmos. Sci.*, 69, 1957–1974.

Lee S. S., W.-K. Tao, and C.-H. Jung, 2014: Aerosol effects on instability, circulations, clouds, and precipitation. *Adv. Meteor.*, 2014, 683950.

Lee S. S., Z. Li, Y. Zhang, H. Yoo, S. Kim, B.-G. Kim, Y.-S. Choi, J. Mok, J. Um, K. O. Choi, and D. Dong, 2018b: Effects of model resolution and parameterizations on the simulations of clouds, precipitation, and their interactions with aerosols, Atmos. Chem. Phys., 18, 13-29.

Li, X., W.-K. Tao, A. P. Khain, J. Simpson, and D. E. Johnson (2009), Sensitivity of a cloud-resolving model to bulk and explicit bin microphysical schemes. Part I: Comparisons, *J. Atmos. Sci.*, 66(1), 3–21.

Li Z., Xia X. and Cribb M. et al. 2007: Aerosol optical properties and their radiative effects in northern China. *J Geophys Res Atmos*, 112: D22S01.

Li Z., F. Niu, J. Fan, Y. Liu, D. Rosenfeld, and Y. Ding, 2011: Longterm impacts of aerosols on the vertical development of clouds and precipitation. *Nat. Geosci.,* 4, 888–894.

Li, Z. J. Guo, A. Ding, H. Liao, J. Liu, Y. Sun, T. Wang, H. Xue, H. Zhang, and B. Zhu, 2017a: Aerosols and boundary-layer interactions and impact on air quality, *Natl. Sci. Rev.*, 4, 810-833, doi:10.1093/nsr/nwx117.

Li, Z., D. Rosenfeld, and J. Fan, 2017b: Aerosols and their impact on radiation, clouds, precipitation, and severe weather events, *Oxford Research Encyclopedias*, doi:10.1093/acrefore/9780199389414.013.126.

Lin J. C., T. Matsui, R. A. Pielke Sr., and C. Kummerow, 2006: Effects of biomass-burning-derived aerosols on precipitation and clouds in the Amazon Basin: a satellite-based empirical study, *J. Geophys. Res.* 111, D19204.

Lin, Y. and K. E. Mitchell, 2005: The NCEP Stage II/IV hourly precipitation analyses: development and applications. Preprints, 19th Conf. on Hydrology, American Meteorological Society, San Diego, CA, 9-13 January 2005, Paper 1.2.

Lindsey, D. T., and M. Fromm (2008), Evidence of thecloud lifetime effect from wildfire-induced thunderstorms, *Geophys. Res. Lett.*, 35, L22809, doi:10.1029/2008GL035680.

Liu, X., et al. (2017), Airborne measurements of western U.S. wildfire emissions: Comparison with prescribed burning and air quality implications, *J. Geophys. Res. Atmos.,* 122, 6108–6129, doi:10.1002/2016JD026315.

Liu, Y.; Achtemeier, G.L.; Goodrick, S.L.; Jackson, W.A. (2010), Important parameters for smoke plume rise simulation with Daysmoke. Atmos. Pollut. Res., 1, 250–259.

Logan, T., X. Dong, and B. Xi (2018), Aerosol properties and their impacts on surface CCN at the ARM Southern Great Plains site during the 2011 Midlatitude Continental Convective Clouds Experiment. *Adv. Atmos. Sci.,* 35(2), 224–233, https://doi.org/10.1007/s00376-017-7033-2.

Logan, T. (2018), Anomalous Lightning Behavior during the 26-27 August 2007 Northern Great Plains Severe Weather Event. *J. Geophys. Res. Atmos.,* 123, https://doi.org/10.1002/2017JD027750.

Lohmann U., and J. Feichter, 2005: Global indirect aerosol effects: A review. *Atmos. Chem. Phys.*, 5, 715–737.

Lu, Z., and I. N. Sokolik (2013), The effect of smoke emission amount on changes in cloud properties and precipitation: A case study of Canadian boreal wildfires of 2007, *J. Geophys. Res. Atmos.*, 118, 11,777–11,793, doi:10.1002/2013JD019860.

Lu Z., X. Liu, Z. Zhang, C. Zhao et al. 2018: Biomass smoke from southern Africa can significantly enhance the brightness of stratocumulus over the southeastern Atlantic Ocean, *Proc Natl Acad Sci U S A.* 2018 Mar 20;115(12):2924-2929.

Luderer, G., Trentmann, J., Winterrath, T., Textor, C., Herzog, M., Graf, H. F., and Andreae, M. O. (2006), Modeling of biomass smoke injection into the lower stratosphere by a large forest fire (Part II): sensitivity studies, *Atmos. Chem. Phys.,* 6, 5261-5277.

Lyons, W. A., Uliasz, M., & Nelson, T. E. (1998). Large peak current cloud-to-ground lightning flashes during the summer months in the contiguous United States. *Monthly Weather Review*, 126 (8), 2217– 2233.

Mandel, J., J. D. Beezley, and A. K. Kochanski, (2011), Coupled atmosphere-wildland fire modeling with WRF 3.3 and SFIRE 2011, *Geosci. Model Dev.*, 4, 591-610.Mandel, J., Amram, S., Beezley, J. D., Kelman, G., Kochanski, A. K., Kondratenko, V. Y., Lynn, B. H., Regev, B., and Vejmelka, M. (2014), Recent advances and applications of WRF–SFIRE, *Nat. Hazards Earth Syst. Sci.*, 14, 2829-2845.

Martin S., P. Artaxo, L. Machado, A. Manzi, R. Souza, C. Schumacher, J. Wang, et al., 2017: The Green Ocean Amazon Experiment (GoAmazon2014/5) Observes Pollution Affecting Gases, Aerosols, Clouds, and Rainfall over the Rain Forest, *Bull. Amer. Meteor. Soc*. 98, 981-997.

Martin, M., R. A. Kahn, and M. G. Tosca, (2018), A Global Analysis of Wildfire Smoke Injection Heights Derived from Space-Based Multi-Angle Imaging, *Remote Sens.,* 10, 1609; doi:10.3390/rs10101609.

Milbrandt, J. A., and M. K. Yau (2005), A multimoment bulk microphysics parameterization. Part II: A proposed three-moment closure and scheme description, *J. Atmos. Sci.*, 62(9), 3065–3081, doi:10.1175/JAS3535.1.

Miller, J. D., C. N. Skinner, H. D. Safford, E. E. Knapp, and C. M. Ramirez (2012), Trends and causes of severity, size, and number of fires in northwestern California, U.S.A., *Ecol. Appl.,* 22(1), 184–203.

Morrison, H., J. A. Curry, and V. I. Khvorostyanov (2005), A new double moment microphysics parameterization for application in cloud and climate models. Part I: Description, *J. Atmos. Sci.*, 62(6), 1665–1677.

Morrison H., 2012: On the robustness of aerosol effects on an idealized supercell storm simulated with a cloud systemresolving model. *Atmos. Chem. Phys.*, 12, 7689–7705.

Murillo, E. M., and C. R. Homeyer, (2019), Severe Hail Fall and Hail Storm Detection using Remote Sensing Observations, *J. Appl. Meteor. Climatol*. doi:10.1175/JAMC-D-18-0247.1.

Nelson, D. L., and R. A. Kahn, 2014, Stereoscopic Retrieval of Smoke Plume Heights and Motion from Space-Based Multi-angle Imaging, using the MISR INteractive eXplorer (MINX), The Canadian Smoke Newsletter, 2014, 10-17.

Niyogi D, P Pyle, M Lei, SP Arya, CM Kishtawal, M Shepherd, F Chen, and B Wolfe. 2011. "Urban Modification of Thunderstorms: An Observational Storm Climatology and Model Case Study for the Indianapolis Urban Region." *Journal of Applied Meteorology and Climatology*. 50(5). 1129–1144.

Peng J. et al., 2016: Markedly enhanced absorption and direct radiative forcing of black carbon under polluted urban environments. *Proc. Natl. Acad. Sci.* USA, 113, 4266–4271.

Peterson, D., E. J. Hyer, J. R. Campbell, J. E. Solbrig, and M.D. Fromm (2016), A Conceptual Model for Development of Intense Pyrocumulonimbus in Western North America. *Monthly Weather Review*. 145, 2235-2255.

Phuleria, H. C., P. M. Fine, Y. Zhu, and C. Sioutas (2005), Air quality impacts of the October 2003 Southern California wildfires, *J. Geophys. Res*.,110, D07S20, doi:10.1029/2004JD004626.

Pikridas M., J. Sciare, F. Freutel, S. Crumeyrolle, S. L. von der Weiden-Reinmüller, A. Borbon, A. Schwarzenboeck, M. Merkel, et al., 2015: In situ formation and spatial variability of particle number concentration in a European megacity, *Atmos. Chem. Phys.* 15, 10219-10237.

Pöhlker, M. L., Pöhlker, C., Ditas, F., Klimach, T., Hrabe de Angelis, I., Araújo, A., Brito, J., Carbone, S., et al., 2016.: Long-term observations of cloud condensation nuclei in the Amazon rain forest – Part 1: Aerosol size distribution, hygroscopicity, and new model parametrizations for CCN prediction*, Atmos. Chem. Phys*., 16, 15709-15740.

Pöhlker, M. L., Ditas, F., Saturno, J., Klimach, T., Hrabě de Angelis, I., Araùjo, A. C., Brito, J., Carbone, S., et al. 2018: Long-term observations of cloud condensation nuclei over the Amazon rain forest – Part 2: Variability and characteristics of biomass burning, long-range transport, and pristine rain forest aerosols, *Atmos. Chem. Phys.*, 18, 10289-10331.

Pöschl U, Martin S.T, Sinha B, Chen Q, Gunthe S.S et al. 2010: Rainforest aerosols as biogenic nuclei of clouds and precipitation in the Amazon, *Science*, 329, 1513-1515.

Qian, Y., and F. Giorgi (2000), Regional climatic effects of anthropogenic aerosols? The case of Southwestern China, *Geophys. Res. Lett.*, 27(21), 3521–3524

Ramanathan V, Crutzen, PJ and Mitra, AP et al. 2002: The Indian Ocean Experiment and the Asian Brown Cloud. *Current Science*; 83(8): 947-955.

Randall D. A., 1980a: Conditional instability of the first kind upside-down. *J. Atmos. Sci*., 37, 125–130.

Randall D. A., 1980b: Entrainment into a stratocumulus layer with distributed radiative cooling. *J. Atmos. Sci.*, 37, 148–159.

Rosenfeld D., and I. M. Lensky, 1998: Satellite-based insights into precipitation formation processes in continental and maritime convective clouds. *Bull. Amer. Meteor. Soc.*, 79, 2457-2476.

Rosenfeld, D., and W. L. Woodley (2000), Deep convective clouds with sustained supercooled liquid water down to −37.5_C, *Nature,* 405, 440–442.

Rosenfeld, D., Fromm, M., Trentmann, J., Luderer, G., Andreae, M. O., and Servranckx, R. (2007), The Chisholm firestorm: observed microstructure, precipitation and lightning activity of a pyro-cumulonimbus, *Atmos. Chem. Phys*., 7, 645-659, https://doi.org/10.5194/acp-7-645-2007.

Rosenfeld D, Lohmann, U and Raga, GB et al. 2008: Flood or drought: How do aerosols affect precipitation? *Science*; 321: 1309-1313.

Rosenfeld D, and T. L. Bell, 2011: Why do tornados and hailstorms rest on weekends? *J. Geophys. Res.*, 116, D20211.

Rosenfeld D, and Coauthors, 2014: Global observations of aerosol-cloudprecipitation-climate interactions. *Rev. Geophys.*, 52, 750–808.

Rosenfeld D., Y. Zheng, and Coauthors, 2016: Satellite retrieval of cloud condensation nuclei concentrations by using clouds as CCN chambers. *Proceedings of the National Academy of Sciences*, 113 (21) 5828-5834.

Saide P.E., S.N. Spak, RB Pierce, JA Otkin, TK Schaack, AK Heidinger, AM da Silva, M Kacenelenbogen, J Redemann, and GR Carmichael. 2015. "Central American Biomass Burning Smoke Can Increase Tornado Severity in the U.S.: Smoke Can Increase Tornado Severity." *Geophysical Research Letters*. 42(3). 956–965. DOI:10.1002/2014GL062826.

Salamanca, F., and A. Martilli, 2010: A new building energy model coupled with an urban canopy parameterization for urban climate simulations—part II. Validation with one dimension off–line simulations. *Theor. Appl. Climatol.*, **99**, 345–356.

Saleeby S., and S. C. van den Heever, 2013. Developments in the CSU-RAMS aerosol model: Emissions, nucleation, regeneration, deposition, and radiation. *J. Appl. Meteor. Climatol.* 52, 2601–2622.

Shepherd JM, H Pierce, and AJ Negri. 2002. "Rainfall Modification by Major Urban Areas: Observations from Spaceborne Rain Radar on the TRMM Satellite." *Journal of Applied Meteorology*. 41(7). 689–701.

Shepherd JM. 2005. "A Review of Current Investigations of Urban-Induced Rainfall and Recommendations for the Future." *Earth Interactions*. 9(12). 1–27. DOI:10.1175/EI156.1.

Shrivastava M., D. Christopher, J. Fan, et al., 2017: Recent advances in understanding secondary organic aerosol: Implications for global climate forcing, *Rev. Geophys.* 55, 509–559.

Skamarock W. C. et al., 2008 “A description of the advanced research WRF version 3” (NCAR Technical Note, National Center for Atmospheric Research).

Sofiev, M.; Ermakova, T.; Vankevich, R. (2012), Evaluation of the smoke-injection height from wild-land fires using remote-sensing data. Atmos. Chem. Phys. 12, 1995–2006.

Storer, R. L., S. C. van den Heever, and G. L. Stephens, (2010), Modeling aerosol impacts on convective storms in different environments. *J. Atmos. Sci.*, 67, 3904–3915

Takahashi, T, and K. Miyawaki, (2002), Reexamination of riming electrification in a wind tunnel. *J. Atmos. Sci.,* 59, 1018–1025,

Tang S., Xie, S., Zhang, Y., Zhang, M., Schumacher, C., Upton, H., Jensen, M. P., Johnson, K. L., Wang, M., Ahlgrimm, M., Feng, Z., Minnis, P., and Thieman, M., 2016: Large-scale vertical velocity, diabatic heating and drying profiles associated with seasonal and diurnal variations of convective systems observed in the GoAmazon2014/5 experiment, *Atmos. Chem. Phys.*, 16, 14249-14264.

Tao W.-K., X. Li, A. Khain, T. Matsui, S. Lang, and J. Simpson, 2007: Role of atmospheric aerosol concentration on deep convective precipitation: Cloud-resolving model simulations. *J. Geophys. Res.*, 112, D24S18.

Thalman, R., de Sá, S. S., Palm, B. B., Barbosa, H. M. J., Pöhlker, M. L., Alexander, M. L., Brito, J., et al., 2017: CCN activity and organic hygroscopicity of aerosols downwind of an urban region in central Amazonia: seasonal and diel variations and impact of anthropogenic emissions, Atmos. Chem. Phys., 17, 11779-11801.

Thornton J. A., K. S. Virts, R. H. Holzworth, and T. P. Mitchell, 2017: Lightning enhancement over major oceanic shipping lanes, *Geophys. Res. Lett*. 44, 9102–9111.

Tory K.J., W. Thurston, and J. D. Kepert, (2018), Thermodynamics of Pyrocumulus: A Concenptual Study, *Mon. Weather Rev.*, 146, 2579-2597.

Trentmann, J., Luderer, G., Winterrath, T., Fromm, M. D., Servranckx, R., Textor, C., Herzog, M., Graf, H.-F., and Andreae, M. O. (2006), Modeling of biomass smoke injection into the lower stratosphere by a large forest fire (Part I): reference simulation, *Atmos. Chem. Phys.,* 6, 5247-5260, https://doi.org/10.5194/acp-6-5247-2006.

Twomey S. 1977: The influence of pollution on the shortwave albedo of clouds. *J Atmos Sci;* 34(7): 1149-1152.

van den Heever, S. C., G. G. Carrio, W. R. Cotton, P. J. DeMott, and A. J. Prenni, 2006: Impacts of nucleating aerosol on Florida convection. Part I: Mesoscale simulations, *J. Atmos. Sci.,* 63, 1752–1775.

van den Heever SC, and WR Cotton. 2007. "Urban Aerosol Impacts on Downwind Convective Storms." *Journal of Applied Meteorology and Climatology*. 46(6). 828–850. DOI:10.1175/JAM2492.1.

van den Heever, S. C., G. L. Stephens, andN. B. Wood, 2011: Aerosol indirect effects on tropical convection characteristics under conditions of radiative-convective equilibrium, *J. Atmos. Sci.,* 68, 699–718.

Wang J., R. Krejci , S. Giangrande, C. Kuang, H. M. J. Barbosa, J. Brito, S. Carbone, X. Chi, J. Comstock, F. Ditas, et al.,2016: Amazon boundary layer aerosol concentration sustained by vertical transport during rainfall, *Nature* 539, 416.

Wang, Q., Z. Li, J. Guo, C. Zhao, M. Cribb, (2018), The Climate Impact of Aerosols on the Lightning Flash Rate: Is it Detectable from Long-term Measurements? *Atmos. Chem. Phys*., 18, 12,797-12,816, doi:10.5194/acp-18-12797-2018.

Wang, X., and X. Zhang (2009), Calculation of electromagnetic induction inside a wind turbine tower struck by lightning, *Wind Energ.,* 13, 615-625, https://doi.org/10.1002/we.382.

Wang, Y., J. Fan, R. Zhang, L. R. Leung, andC. Franklin (2013), Improving bulk microphysics parameterizations in simulations of aerosol effects, *J. Geophys. Res. Atmos*., 118, 5361–5379,

Wiedinmyer, C., Akagi, S. K., Yokelson, R. J., Emmons, L. K., Al-Saadi, J. A.,Orlando, J. J., and Soja, A. J. (2011), The Fire INventory from NCAR (FINN): a high resolution global model to estimate the emissions from open burning, *Geosci. Model Dev.,* 4, 625-641, doi:10.5194/gmd-4-625-2011.

Williams. E, V. Mushtak, D. Rosenfeld, S. Goodman and D. Boccippio (2005), Thermodynamic conditions favorable to superlative thunderstorm updraft, mixed phase microphysics and lightning flash rate, *Atmospheric Research,* 76, 288-306.

Wood R., 2012. Review: Stratocumulus clouds. *Mon. Wea. Rev.*, 140, 2373–2423.

Yair, Y., B. H. Lynn, C. Price, V. Kotroni, K. Lagouvardos, E. Morin, A. Mugnai, and M. C. Llasat (2010), Predicting the potential for lightning activity in

Mediterranean storms based on the Weather Research and Forecasting (WRF) model dynamic and microphysical fields. *J. Geophys. Res.,* 115, D04205, doi:10.1029/2008JD010868.

Yang X., M. Ferrat, and Z. Li, 2013a: New evidence of orographic precipitation suppression by aerosols in central China. Meteor. *Atmos. Phys.*, 119, 17–29.

Yang X, Z. Yao, Z. Li, and T. Fan, 2013b: Heavy air pollution suppresses summer thunderstorms in central China. *J. Atmos. Sol.-Terr. Phys.*, 95–96, 28–40.

Yang Y., J. Fan, R. L. Leung, C. Zhao, Z. Li, and D. Rosenfeld, 2016: Mechanisms contributing to suppressed precipitation in Mt. Hua of central China. Part I: Mountain valley circulation. *J. Atmos. Sci.,* 73, 1351–1366.

Yin, Y., K. S. Carslaw, and G. Feingold, 2005: Vertical transport and processing of aerosols in a mixed-phase convective cloud and the feedback on cloud development, *Q. J. R. Meteorol. Soc*., 131, 221–245.

Zaveri, R. A., R. C. Easter, J. D. Fast, and L. K. Peters, (2008), Model for Simulating Aerosol Interactions and Chemistry (MOSAIC). United States: N. p., 2008. Web. doi:10.1029/2007JD008782.

Zhang Q., Streets, D. G., Carmichael, G. R., He, K. B., Huo, H., Kannari, A., Klimont, Z., Park, I. S., Reddy, S., Fu, J. S., Chen, D., Duan, L., Lei, Y., Wang, L. T., and Yao, Z. L. , 2009: Asian emissions in 2006 for the NASA INTEX-B mission, *Atmos. Chem. Phys*., 9, 5131-5153.

Zhang R., G. Li, J. Fan, D. L. Wu, and M. J. Molina, 2007: Intensification of Pacific storm track linked to Asian pollution. *Proc. Natl. Acad. Sci. U. S. A.* 104, 5295-5299.

Zaveri, R.A. and Peters, L.K. (1999). A new lumped structure photochemical mechanism for large-scale applications. J. Geophys. Res. Atmos. 104: 30387–30415.

Zhang R., A. Khalizov, Lin Wang, M. Hu, W. Xu, 2012: Nucleation and growth of nanoparticles in the atmosphere, *Chem. Rev.* 112, 1957-2011.

Zhang Y., 2008: Online-coupled meteorology and chemistry models: history, current status, and outlook, *Atmos. Chem. Phys*., 8, 2895-2932.

Zhang Y., J. Fan, T. Logan, Z. Li, and C. Homeyer (2019a), Wildfire impact on environmental thermodynamics and severe convective storm, *Geophysical Research Letters*. (Minor revision)

Zhang Y., J. Fan, and Z. Li (2019b), Impacts of Cloud Microphysics Parameterizations on Simulated Aerosol-Cloud interactions. (In preparation)

Zhang Y., J. Fan, and Z. Li (2019c), Impacts of Land Surface and Aerosol Changes from Houston Urbanization on Convective Storms. (In preparation)

Zhong S, Y Qian, C Zhao, R Leung, and X-Q Yang. 2015. "A Case Study of Urbanization Impact on Summer Precipitation in the Greater Beijing Metropolitan Area: Urban Heat Island versus Aerosol Effects: Urbanization Impact on Precipitation." *Journal of Geophysical Research: Atmospheres*.120(20). 10,903–10,914. DOI:10.1002/2015JD023753.

Zhou J. C., E. Swietlicki, H. C. Hansson, and P Artaxo, 2002: Submicrometer aerosol particle size distribution and hygroscopic growth measured in the Amazon rain forest during the wet season. *J. Geophys. Res*. 107, 8055.